ION BEAM MIXING AND THERMOELECTRIC CHARACTERISTICS OF Bi-Sb THIN FILM ALLOYS

By

AHMAD MAHMOUD IBRAHIM, B.Sc. (EE), M.Eng.

A Thesis

Submitted to the School of Graduate Studies

in Partial Fulfilment of the Requirements

for the Degree

Doctor of Philosophy

McMaster University

 August 1986

ION BEAM MIXING AND THERMOELECTRIC CHARACTERISTICS OF Bi-Sb THIN FILM ALLOYS

DOCTOR OF PHILOSOPHY (1986)
(Electrical Engineering)

McMASTER UNIVERSITY
Hamilton, Ontario

TITLE: Ion Beam Mixing and Thermoelectric Characteristics of Bi-Sb Thin Film Alloys

AUTHOR: Ahmad Mahmoud Ibrahim
B.Sc. (EE) (Ain Shams University, Cairo, Egypt)
M.Eng. (McMaster University, Hamilton, Ontario)

SUPERVISOR: Dr. D.A. Thompson

NUMBER OF PAGES: xi, 128

ABSTRACT

This thesis is concerned with investigating the production of thin film Bi-Sb alloys by ion beam mixing. Samples were composed of a thin Sb film sandwiched between two Bi layers; the thicknesses of the films were varied to produce composition range from 0 to ~45% Sb. The overall thickness was about 55 nm.

Analysis of the films by Rutherford Backscattering Spectrometry (RBS) and Auger Electron Spectroscopy (AES) indicated that ion beam mixing can produce uniform Bi-Sb alloys with doses of about 2.8×10^{15} cm^{-2} of 80 KeV Ar^+ at room temperature. The results of Electron Microscopy showed a grain growth due to ion bombardment.

The mixing was characterized by the increase in the full width at half maximum (FWHM) of the Sb signal in the RBS spectra. It was measured as a function of ion dose, dose rate, mass, and energy. The dependence of mixing on the temperature was also investigated. A square-root dependence of mixing on the dose confirmed a diffusion like mixing process. The rate of mixing per ion dose was found to increase with the elastic energy deposited at the Bi/Sb interface. The mixing is temperature independent in the range of ~40 to ~266 K, i.e., collision cascade mixing dominates. An effective diffusion coefficient, D*, of about 4.9×10^{-28} cm^4/ion was determined. At temperatures higher than ~266 K, the mixing increases with the temperature. This suggests that a radiation enhanced diffusion mechanism is the dominant mixing process. An effective diffusion coefficient of $\sim1.7\times10^{-27}$ cm^4/ion at room temperature was calculated; an activation energy of ~0.15 eV was found.

Thermoelectric characteristics of the alloys were investigated by measuring the thermal voltage, V_s, as a function of the temperature, T, in the range 300-500 K, for alloys with various composition. The thermal voltage was found to have a linear dependence on

temperature. The thermoelectric power, dV_y/dT, reaches a maximum of about 70 μV/deg, for $Bi_{.87}\ Sb_{.13}$. The dependence of the thermoelectric power on Sb concentration agrees with the model put forward to explain the transport properties of bulk Bi-Sb alloys. An empirical model has been proposed to relate the state of mixing with the measured thermoelectric power.

ACKNOWLEDGEMENTS

I am grateful to Dr. D.A. Thompson for his continuous encouragement, support, and guidance that made this work possible.

I am indebted to Dr. J.A. Davies for the precious pieces of advice and suggestions that I benefited greatly from throughout this work.

I am thankful to Dr. H.D. Barber for his continuous interest in my work and his valuable comments and suggestions.

I would like to thank Mr. D. Yaraskavitch for his skillful efforts in sample preparation.

I also thank Ms. D. Stevanovic and Mr. U. Akano for their valuable comments and discussions.

I also thank Mr. B. McClelland for ion-implanting the samples used for electron microscopy.

I acknowledge with gratitude the help of Dr. R. Underhill in the Auger analysis and the help of Dr. B. Robertson and Mr. F. Pearson in the electron microscopy.

I would like to thank Dr. V. Tikku for useful discussions during the very early stages of the work.

TABLE OF CONTENTS

TABLE OF CONTENTS (continued)

LIST OF FIGURES

LIST OF FIGURES (continued)

LIST OF FIGURES (continued)

LIST OF TABLES

CHAPTER I

INTRODUCTION

Thin fim thermoelectrics have a wide range of applications; they can be used as sensitive surface thermometers, radiation detectors, cooling devices, and electrical power generators [1,2]. Since the power produced by thin film thermoelectric generators is in the microwatt range, they became of increasing interest with the advent of low-power-consumption microelectronic devices. Thin film thermoelectric generators are of special value in aerospace and medical applications where light-weight, long-life power sources are required for the microelectronic devices [2,3].

The possibility of producing thin film alloys that have favourable thermoelectric characteristics using ion beam mixing technique was pioneered by Benenson et al. [4]. This technique uses ion bombardment of a solid target to produce changes in the spatial distribution of the elemental species composing the target. The basic idea of producing a thin film alloy by ion beam mixing is illustrated in Fig. (1.1).

In the present study, the formation of Bi-Sb alloys using ion beam mixing technique is investigated along with the thermoelectric characteristics of the alloys produced. Bi-Sb alloys were selected because they have a potential for efficient thermoelectric generation (for a recent review, see Ref. [5]). The alloys are also of interest from the physics point of view; Bi and Sb are semimetals, however, their bulk alloys were reported to exhibit semimetallic, semiconductor, or gapless behaviour depending on the alloy composition [5]. Recently, however, it was reported [6] that doping single crystal Bi with Sb by direct ion implantation, i.e., by bombarding Bi with energetic Sb ions and letting them come to rest within the Bi crystal, did not lead to changes in the semimetallic behaviour of Bi towards a

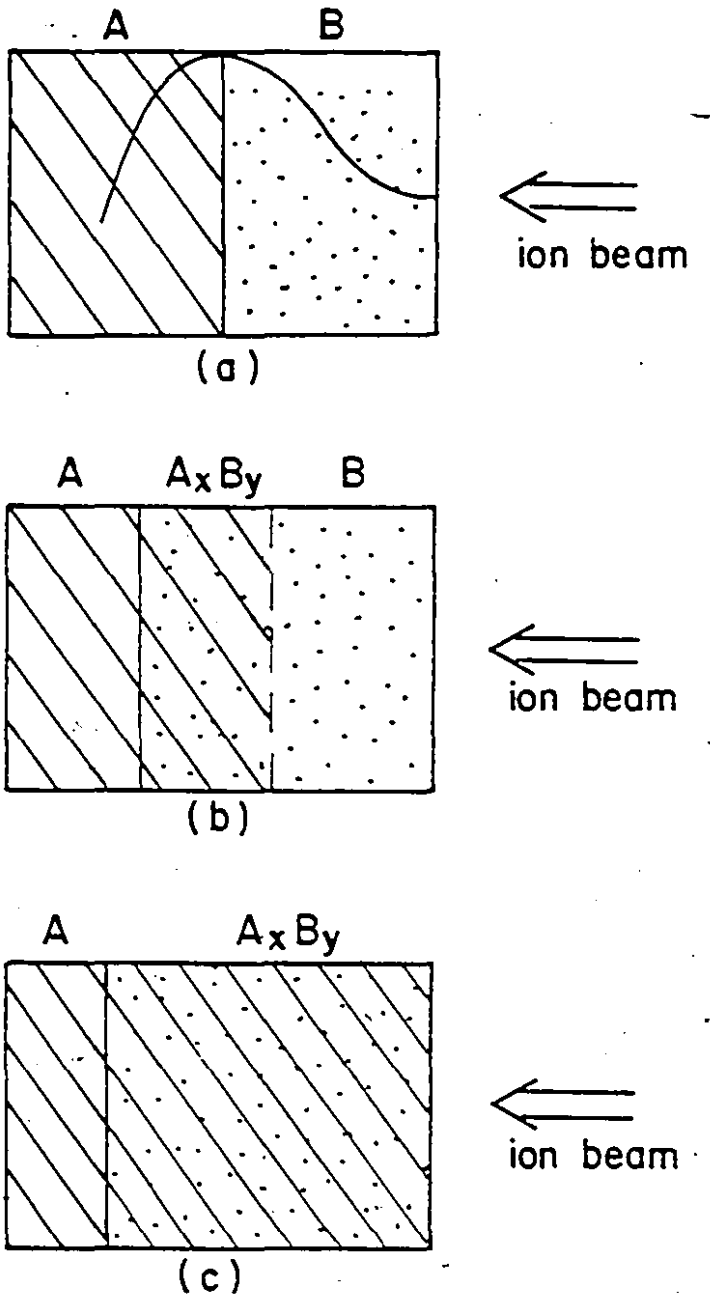

Fig. (1.1) The basic idea of ion beam mixing.

semiconductor behaviour as anticipated; thermoelectric properties were not investigated and only one dose (5×10^{15} Sb/cm^2) was reported. Ion implantation can only produce dilute alloys; the limit is set up by the sputtering yield, i.e., the number of ejected atoms from the solid per incident ion. This is demonstrated in Fig. (1.2). The maximum achievable concentration of ions A in a target B is given by [7]:

$$N_A/N_B = r/(y-1) \qquad (1.1)$$

where, y is the sputtering yield, and r is the preferential sputtering factor; $r>1$ if the probability of sputtering B atoms is greater than that of A atoms.

Fig. (1.3) shows calculated distribution of 150 KeV Sb^+ implanted into Bi for a dose of 5×10^{15} Sb^+/cm^2 (to simulate the conditions given in Ref. [6]); the sputtering yield is assumed to be 5.0 [8]. One can conclude that ion implantation is not only limited by the sputtering yield but will also lead to a depth-dependent alloy composition; ion implantation with multiple energies will be needed if a resulting uniform composition with depth is required.

Ion beam mixing overcomes these difficulties and make it possible, in many cases, to produce uniform alloys with any composition. Comparison with conventional alloying techniques can then be more informative, particularly for Bi-Sb alloys because Bi and Sb are completely soluble in each other [9].

Ion beam mixing of various systems has been investigated. They can be classified in general, as: metal/metal, metal/semimetal, and metal/semiconductor systems (for a review see Ref. [10]). Recently, ion beam mixing in metal/oxide and metal/glass systems was reported [11-13]. The present study is thus the first investigation of a semimetal/semimetal system. It is also the first detailed study of the thermoelectric properties of the alloys produced by ion beam mixing technique [14]. The study mainly addresses the following questions:

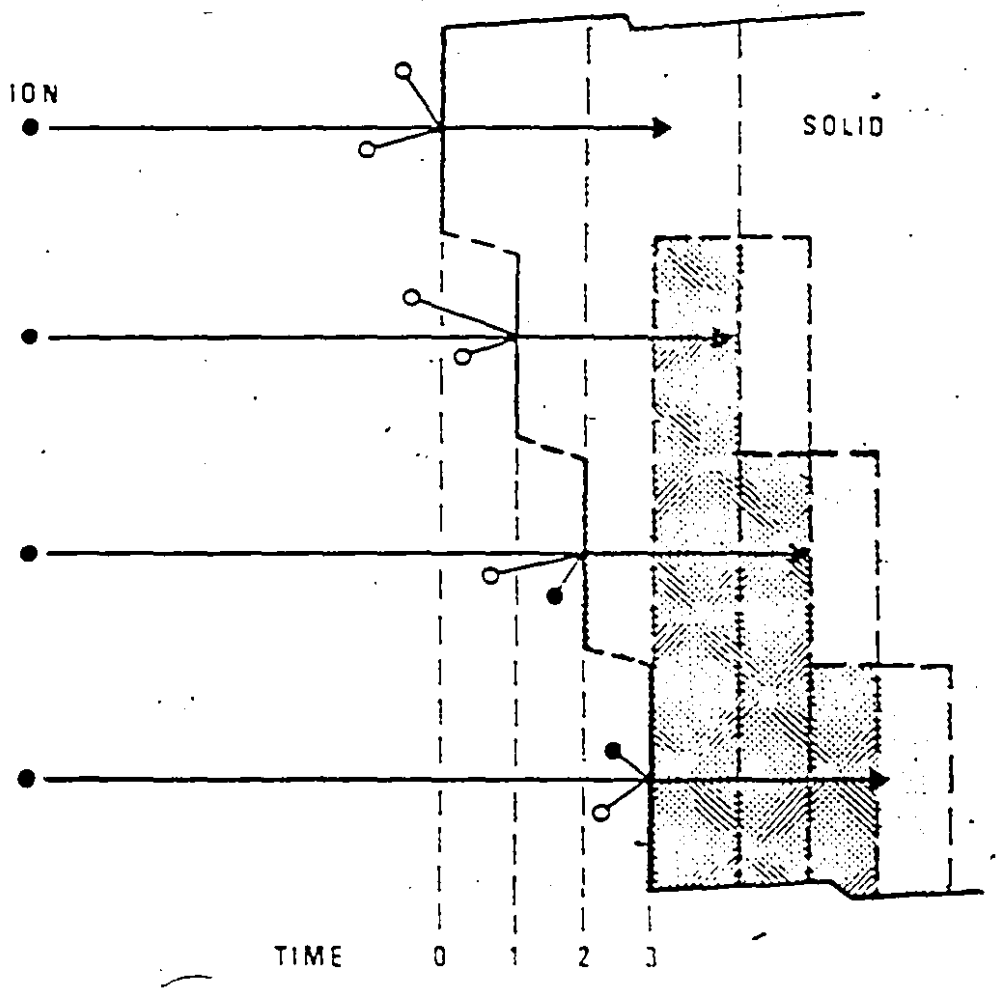

Fig. (1.2) The role of sputtering in determining the maximum number of retained ions (Ref. [9]).

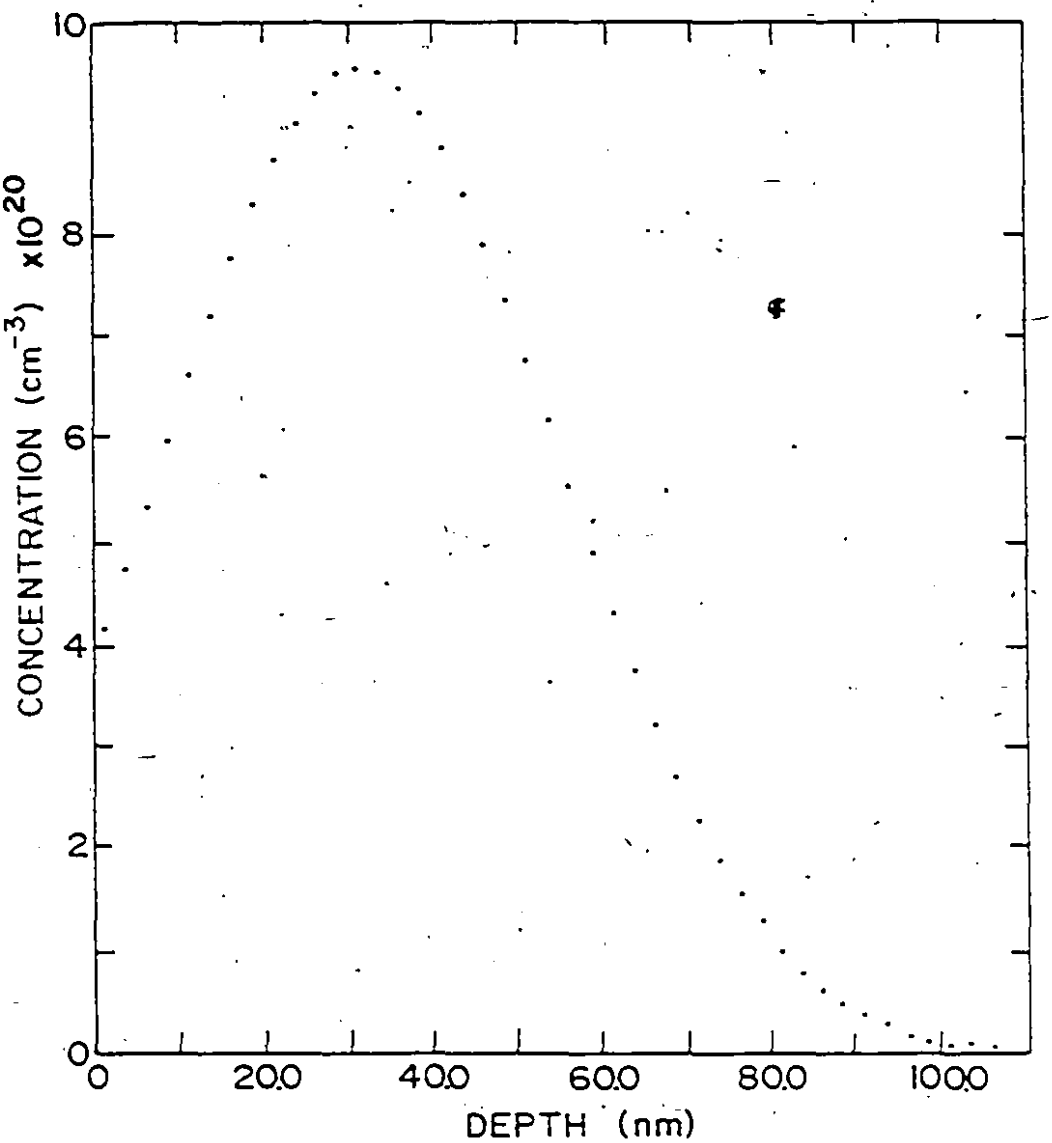

Fig. (1.3) Calculated distribution of 150 KeV Sb implanted into Bi. (5×10^{15}Sb/cm^2)

- Can Bi-Sb alloys be obtained conveniently by ion beam mixing and what alloy composition can be produced?
- What are the thermoelectric properties of the alloys produced?
- What mechanisms are responsible for mixing in this system?

The thesis is divided into six chapters. In Chapter II, the basic concepts of atomic collisions in solids are presented. Models of ion beam mixing along with major experimental findings are then reviewed. In Chapter III, the theory of thermoelectricity is presented. The criteria of determining the usefulness of an alloy for thermoelectric applications are discussed and thin film thermoelectrics investigated up to date are listed. Thin film thermoelectric generators are also discussed. In Chapter IV, the experimental techniques are discussed. The experimental findings of the present investigation are presented and discussed in Chapter V. Chapter VI gives a summary of the results and the main conclusions of the work.

CHAPTER II

ION BEAM MIXING

2.1 Introduction

Ion beam mixing is the result of ion bombardment of a solid composed of unlike atoms that have a depth-dependent distribution. The bombarding ions transfer their energy to the atoms of the solid through elastic and inelastic collision events. The theory of atomic collisions in solids is well documented in the literature. The basic ideas of the theory will be reviewed in Section (2.2). The literature of ion beam mixing is still growing with various authors adopting different approaches and notations. A unified theoretical framework will be presented in Section (2.3). The major experimental findings, reported by various workers, will be reviewed in Section (2.4).

2.2 Atomic collisions in solids

The collision theory treats the interaction between a moving ion and target atoms classically. The collision is assumed to be binary and the struck atom is assumed to be stationary before the collision. Also, it is assumed that the incident ion loses its energy through elastic and inelastic scattering events; the two mechanisms are assumed to be independent [15].

2.2.1 Elastic scattering

The main features of elastic scattering are shown in Fig. (2.1). The scattering angle, θ, in the centre of mass coordinates is given by [16]:

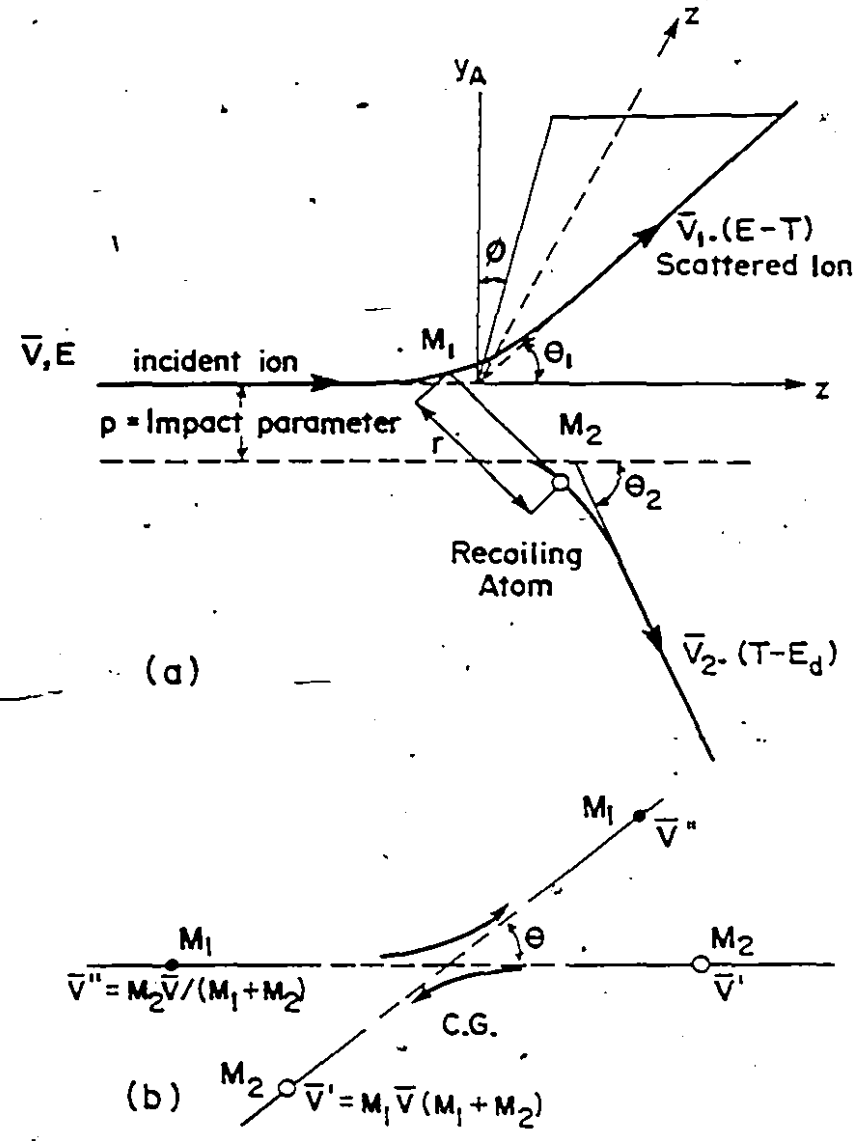

Fig. (2.1) a) Binary collision in Laboratory Coordinate System
b) Binary Collision in Centre of Mass Coordinate System.

$$\theta = \pi - 2p\int_0^{u_0} \frac{du}{[1 - V(u)/E' - p^2 u^2]^{1/2}} \qquad (2.1)$$

where,

p = the impact parameter,

E = the energy of the incident particle,

$E' = M_2 E/(M_1 + M_2)$,

M_1 and M_2 are the masses of the incident and struck particles respectively,

$u = 1/r$ and $u_o = 1/r_o$, and

V(u) = the interatomic potential.

A number of approximate interatomic potentials have been suggested [16-21] to treat a particular range of approach distance, r. They stem from a Coulomb interaction between the charged nuclei, taking into account the effect of screening of the nuclear charge by the atomic electrons. Firsov [22] suggested one convenient potential that has a sufficient range of validity to describe interactions appropriate to ion implantation; it has the form:

$$V(r) = \frac{Z_1 Z_2 e^2}{r}\,\phi\,(Z_1/Z_2, r/a) \qquad (2.2)$$

where, ϕ is the Thomas-Fermi function which has been calculated by Gombas [23], and a is the Thomas-Fermi screening length; given by: $a = 0.8853\, a_o/(Z_1^{2/3} + Z_2^{2/3})^{1/2}$; a_o being the first Bohr oribital radius for the hydrogen atom, and Z_1 and Z_2 are the atomic numbers of the incident and struck atoms, respectively.

Equation (2.1) has been solved by perturbation for small angle scattering and the results extrapolated to large scattering angles [24]. The scattering cross- section can then be expressed, for all combinations of ion and target atoms, by [24]:

$$d\sigma_n = \frac{1}{2}\,\pi a^2 t^{-3/2} f(t^{1/2})\, dt \qquad (2.3)$$

where,

$t = \varepsilon^2 T/T_m$,

ε = a/b (known as the reduced energy),

b = $2 Z_1 Z_2 e^2/E'$ (known as the collision diameter),

e is the electronic charge,

T is the recoiling atom energy,

and T_m is the maximum recoiling atom energy.

A useful approximation to $f(t^{1/2})$, known as the power cross-section approximation, is expressed as [24]:

$$f(t^{1/2}) = \lambda_m t^{1/2 - m} \quad ; \quad 0 \leq m \leq 1 \tag{2.4}$$

The values of m for best approximation are chosen according to the value of ε:

For $\varepsilon \geq 10.0$, $m = 1$, $\lambda_m = 0.5$; this corresponds to scattering.

For $0.1 < \varepsilon < 2.0$, $m = 0.5$, $\lambda_m = 0.328$; this corresponds to an inverse square potential.

For $\varepsilon < 0.2$, $m = 0.33$, $\lambda_m = 1.309$; this corresponds to an inverse cube potential.

For $\varepsilon << 0.01$, $m = 0.0$, $\lambda_m = 24.0$; this corresponds to Born-Bayer potential [25].

The stopping power due to nuclear scattering, $(dE/dx)_n$, can then be written as:

$$\left(\frac{dE}{dx}\right)_n = -N \int_o^{T_m} T \, d\sigma$$

$$= -N \int_o^{\varepsilon} T \frac{\pi a^2 dt}{2 t^{3/2}} f(t^{1/2})$$

$$= -\frac{N \pi a^2 T_m}{\varepsilon^2} \int_o^{\varepsilon} d(t^{1/2}) f(t^{1/2}). \tag{2.5}$$

where, N is the atomic density of the target.

A universal nuclear stopping cross-section, $S(\varepsilon)$ can be written in terms of a dimensionless range paramer, ρ, as [26]:

$$S_n(\varepsilon) = -\left(\frac{d\varepsilon}{d\rho}\right) = \frac{1}{\varepsilon} \int_o^{\varepsilon} f(t^{1/2}) \, d(t^{1/2}) \tag{2.6}$$

where,

$$\rho = 4R\pi a^2 N[M_1 M_2/(M_1 + M_2)^2], \tag{2.7}$$

R being the range of the incident ion in the target material.

For the power cross-section approximation, Eq. (2.6) becomes:

$$S_n(\varepsilon) = \lambda_m \varepsilon^{1-2m}/2(1-m). \tag{2.8}$$

For $m = 1.0$, $S_n(\varepsilon) = [\ell n(1.29\varepsilon)]/2\varepsilon$

for $m = 0.5$, $S_n(\varepsilon) = 0.327$,

for $m = 0.33$, $S_n(\varepsilon) = 0.981(\varepsilon)^{0.33}$, and

for $m = 24.0$, $S_n(\varepsilon) = 12.0\varepsilon$

2.2.2 Inelastic scattering

Inelastic scattering loss occurs due to excitation and ionization of the struck atom. This interaction depends on the projectile velocity, v_1 relative to $v_o Z_1$; v_o being the orbital velocity of the hydrogen atom electrons. At high velocities ($v_1 >> v_o Z_1$), the electronic (inelastic) stopping power is given by [27]:

$$\left(\frac{dE}{dx}\right)_e = N Z_2 [4\pi (Z_1 e^2)^2/m_e v_1^2] L \tag{2.9}$$

where, $L = \ell n(0.2 M_e v_1^2/Z_3)$,

At low velocities ($v_1 << v_o Z_1$), the electronic stopping power is given by [28]:

$$\left(\frac{d\varepsilon}{d\rho}\right)_e = S_e(\varepsilon) = \kappa \varepsilon^{1/2} \tag{2.10}$$

where,

$$\kappa = \xi_e \frac{0.0793 (Z_1 Z_2)^{1/2} (M_1 M_2)^{3/2}}{(Z_1^{2/3} + Z_2^{2/3})^{3/4} M_1^{3/2} M_2^{1/2}}.$$

Since $\kappa = \kappa(M_1, M_2, Z_1, Z_2)$, there is no universal curve for $S_e(\varepsilon)$. Fig. (2.2) shows $S_e(\varepsilon)$ for selected values of κ; it shows also the universal curve for $S_n(\varepsilon)$.

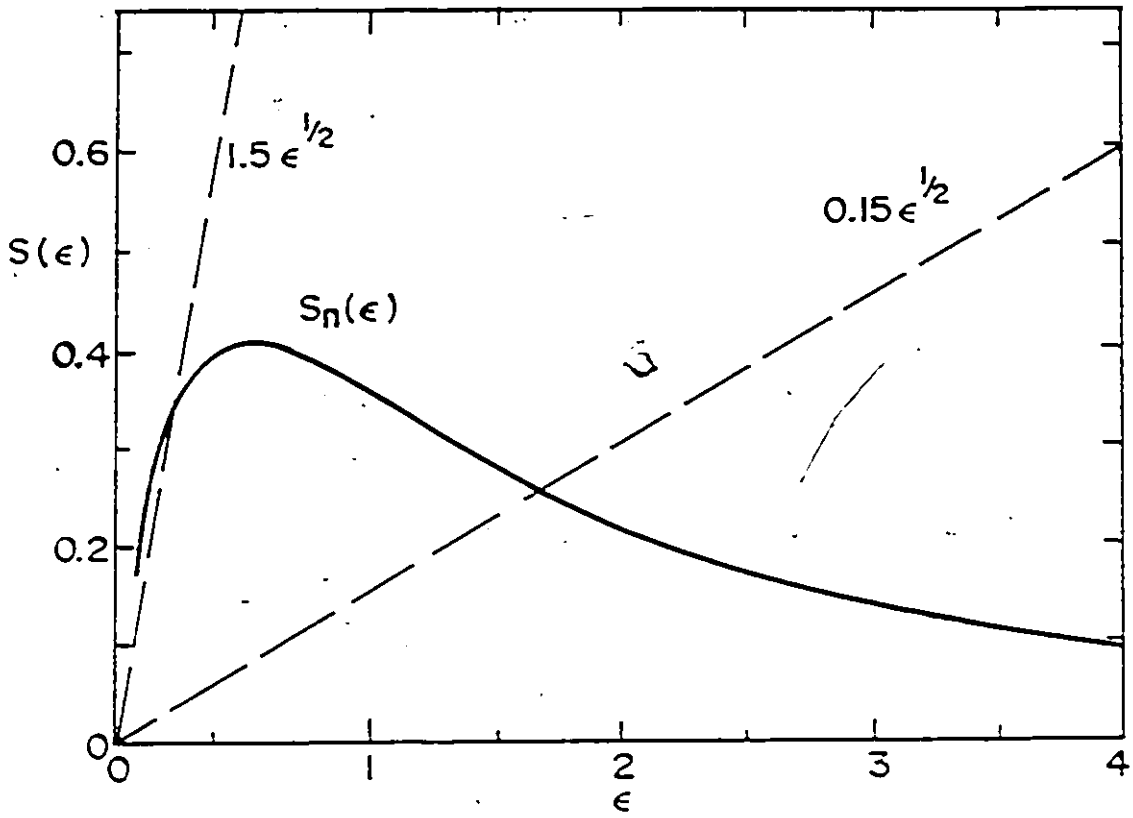

Fig. (2.2) Nuclear and electronic stopping powers in reduced units (Ref. [28]).

The above theory (Lindhard theory), predicts monotonic dependance of the energy loss rate on the atomic number of the incident particles. However, experimental results [29,30] show a periodic dependance [see Fig. (2.3)]. In Lindhard theory, the monotonic dependence of $(dE/dx)_e$ on Z, arises because the atomic charge distributions and potentials were smoothed as function of radius. More recent theories [31, 32] of inelastic energy loss have treated atoms in terms of their more precise radial electron density wave functions; these lead to qualitative agreement with experimental data. The position of maxima and minima of energy loss as a function of atomic number are reproduced [32], but the magnitudes are not in agreement with the experimental data. In spite of the oscillatory behaviour of the energy loss, Lindhard's theory is adequate as a first order approximation.

The total stopping power, (dE/dx), is given by:

$$\left(\frac{dE}{dx}\right) = \left(\frac{dE}{dx}\right)_n + \left(\frac{dE}{dx}\right)_e . \tag{2.11}$$

As shown in Fig. (2.1), nuclear stopping dominates at low energies and electronic stopping dominates at high energies.

For a uniform alloy composed of two types of atoms, we have [33]:

$$S(E)_{molecule} = p\,S_1(E) + q\,S_2(E) \tag{2.12}$$

where, p is the number of type (1) atoms and q is the number of type (2) atoms in a molecule. This leads to:

$$S(E)_{atom} = \frac{p\,S_1(E) + q\,S_2(E)}{p + q} . \tag{2.13}$$

2.2.3 The number of displaced atoms

Kinchin and Pease [34] proposed a simple method to find the number of atoms displaced by any energetic particle impacting a solid. It is based on the assumption of a unique threshold displacement energy, E_d, such that, if an atom receives energy greater than E_d, it will be permanently displaced. For an incident particle, with energy E, the model

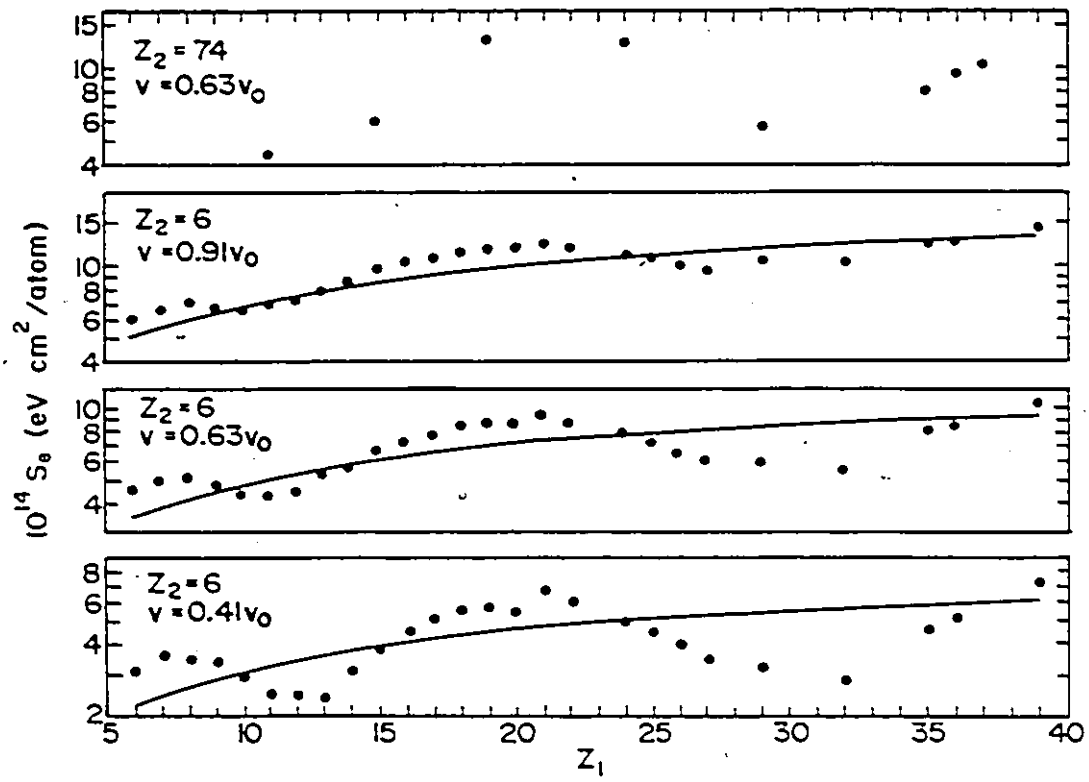

Fig. (2.3) Electronic stopping cross-section S_e vs. Z_i. The solid curves indicate calculated values according to Lindhard theory (Ref. [30]).

predicts that the number of displaced atoms, N_{KP}, is:

$$N_{KP} = E/2\,E_d \qquad ; \quad E > E_d . \tag{2.14}$$

The model was modified by Robinson [35]. He generalized the assumptions to allow for inelastic and elastic collisions with screened Coulomb potential. It was assumed that only elastic collisions produce displacement. This has led to the number of displaced atoms, N_D, being:

$$N_D = \xi(m)\, v \cdot E/2\,E_d \qquad ; \; E > E_d . \tag{2.15}$$

where, v is the fraction of energy deposited into elastic collisions, and

$$\xi(m) = 2(2^m - 1) / [\psi(1) - \psi(1-m)]$$

where,

$$\psi(x) = \frac{d}{dx} \ell n\, \Gamma(x) .$$

Sigmund [36] suggested that the approximation m = 0 should be used since it is the number of near-threshold collisions ($E \simeq 2\,E_d$) of the higher generation of recoil atoms that primarily determines N(E) and hence m. This leads to:

$$N_D(E) = \frac{6}{\pi^2}\, v\, \frac{E}{U}\, \ell n\left(1 + \frac{U}{E_d}\right). \tag{2.16}$$

For $U = E_d$, Eq. (2.16) becomes:

$$N_D(E) = 0.42\, v . E/E_d . \tag{2.17}$$

Eq. (2.17) is usually referred to as the modified Kinchin-Pease equation.

2.2.4 Cascade dimensions

The cascade dimensions depend on the spatial distribution of the elastic energy deposition. To find the equation governing the energy disposition [37], let an ion with velocity v strike the target surface at $r = 0$. The energy deposited in a volume d^3r at r is given by $F(r,v)\, d^3r$.

The probability for a collision to occur when a particle moves a distance δR is $N\delta R d\sigma$, where $d\sigma$ is the scattering cross-section and N is the atomic density. The corresponding deposited energy is:

$$N\,\delta\,R\,d\sigma\,[F(r, v') + F(r, v'']\,d^3r$$

where v' and v'' are the velocity of ion and recoil, respectively. The probability for a collision not to occur is $(1-N\delta R d\sigma)$. The corresponding deposited energy at (r, v) d^3r would be:

$$(1 - N\,\delta\,R\,d\sigma)\,F(r - \delta R, v)\,d^3r.$$

Hence, the total energy deposited F(r,v) is:

$$F(r, v) = [N\,\delta\,R \int d\sigma\,[F(r, v') + F(r, v'') + (1 - N\,\delta\,R \int d\sigma)\,F(r - \delta\,R, v)]. \tag{2.18}$$

This leads to:

$$\frac{v}{v}\,\frac{\partial}{\partial r}\,F(r, v) = N \int d\sigma[F(r, v'') + F(r, v') - F(r, v)]. \tag{2.19}$$

Eq. (2.19) is the basic integro-differential equation for the spatial distribution of energy deposition. Multiplicaton by r^n and integration by parts leads to a recursive expansion for the spatial moments [26,37]. The problem then becomes one of constructing the distribution from a finite number of generated moments. The Edgeworth expansion [38,39] is used for that purpose. It has the advantage of having a simple form and being a weighted-Gaussian function. For incidence normal to the surface of the target, the longitudinal distribution may be expressed in terms of the Edgeworth expansion, for the first four moments, as:

$$F(Z, E) = \frac{g}{\sqrt{2\pi}\,\sqrt{\mu_2}} \exp\left(-\frac{\xi^2}{2}\right) f(\xi) \tag{2.20}$$

where,

$$f(\xi) = 1 - \left(\frac{\mu_3}{6\,\mu_2^{3/2}}\right)\cdot\ (3\xi - \xi^3) + \frac{1}{24}\left(\frac{\mu_4}{\mu_2^2} - 3\right)\cdot\ (3 - 6\,\xi^2 - \xi^4)$$

$$-\left(\frac{\mu_3^2}{72\,\mu_2^3}\right)(15 - 45\,\xi^2 + 15\,\xi^4 - \xi^6),$$

$$\xi = \frac{Z - \langle Z\rangle}{\mu_2^{1/2}},$$

$$\mu_n = \langle (Z - \langle Z\rangle)^n \rangle$$

$$g = \begin{cases} 1 & \text{for range distribution} \\ \nu\cdot E & \text{for damage distribution} \\ \eta\cdot E & \text{for ionization distribution} \end{cases}$$

2.2.5 Spike effects

The collision theory assumes that the collisions are binary between one moving and one stationary atom. However, as the collision density becomes higher (heavy atoms or low energy) the atoms interact collectively rather than discretely. This situation can not be treated by the collision theory; new concepts known as "spikes" are introduced to model the interaction.

A) Displacement spike

Brinkman [40,41] proposed that when the mean free path between displacement collisions approaches the interatomic spacing of the target, a violently disturbed region will be created where diplaced atoms move outward from the center. The atoms come to rest at small distances from the center because of their low energy. A vacancy-rich core will thus be created surrounded by a region with excess interstitial atoms. Heavy ions ($M_1 \geq 100$) with energies in the range 10

to 60 KeV will typically result in a displacement spike extending over essentially the total cascade dimensions [42]. Many of the defects produced in the spike region will migrate to take up a more energetically favourable configuration. Nevertheless, a certain degree of disorder will persist.

B) **Thermal spike**

When the energy of the primary (and each displaced atom) degrades to less than E_d, it will be unable to produce further displacements. In order to achieve thermal equilibrium, it dissipates this excess kinetic energy as heat or lattice vibrations. This type of dissipation is termed thermal spike [43]. The time required for an ion with energy in the range 10 to 100 KeV to come to rest is about 10^{-13} sec. If the number of atoms involved in the cascade volume is large enough, typically about 10^4 - 10^5 atoms [42], their energy distribution can be described by Maxwell-Boltzman statistics after $\sim 10^{-12}$ sec. The concept of local temperature and heating becomes practical. Brinkman [40] has pointed out that the thermal spike could occur after the propagation of the displacement spike.

The common assumption in all theoretical spike models [43,45] is the applicability of heat transport equation:

$$\frac{\partial T}{\partial t} = K \frac{\partial^2 T}{\partial x^2} \qquad (2.21)$$

where, K is the thermal diffusivity.

The usual thermal conductivity consists of two components due to lattice and electronic contribution. The coupling between the lattice and the electrons is not sufficiently strong to permit appreciable exchange of energy in times of the order of 10^{-12} sec. [41]. Since the times involved in energy spikes are of this magnitude or less, it is argued that the energy given to

an atom will be dissipated in the lattice only, i.e., the effective thermal conductivity is the lattice conductivity. Another approach for calculating K was adopted by Sigmund [36]; he calculated K from kinetic gas theory assuming that the spike region can be treated as a high pressure gas. Once a value is assigned to K, the temperature- time evolution of the spike can be determined with the possibility of evaluating the resulting effects such as defect migration, annealing etc.

2.3 Theoretical framework of ion-beam mixing

The configurations of the systems investigated under ion-beam mixing conditions are:

i) Thin layer of element A on a semi-infinite substrate of element B (bilayer),

ii) Very thin layer of element A buried in an otherwise uniform material B (marker),

or iii) Alternate thin layers of A and B (multilayer).

This is shown schematically in Fig (2.4). The interfaces between A and B regions are assumed to be sharp and well defined. Bombardment with the mixing ions leads to progressive migration across the interface.

A set of equations describing the mixing process will contain terms of three types, corresponding to three types of processes involved [46]; ballistic, diffusive, and directional. Ballistic mixing can be subdivided according to the number of collisions and damage cascade density. Mixing resulting from non-overlapping cascades can be denoted isotropic cascade mixing.

Diffusive mixing describes relocation processes that consist of a large number of small jumps; the jumps being isotropic on the atomic scale. All these processes can be

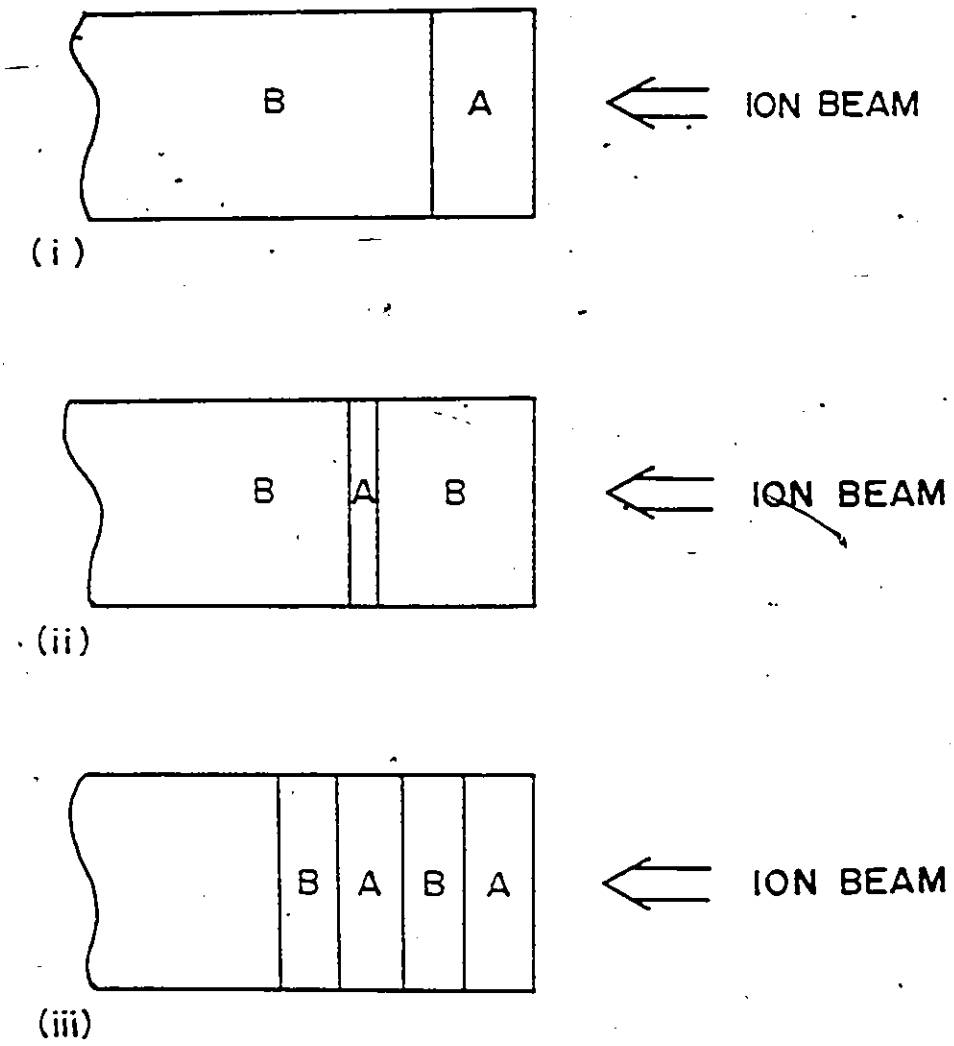

Fig. (2.4) Schematic of sample geometries used in ion beam mixing investigations.

described in terms of "effective diffusivities". The overall effect can be described in terms of a resultant diffusivity which is the linear sum of the individual diffusivities. Directional mixing denotes relocation processes that are not isotropic in atomic scale. They are best described in terms of chemical potential. However, models were proposed in terms of effective diffusivities.

Some of the above processes will be less important than the others depending on the particular regime considered.

2.3.1 Cascade mixing

Since most of the collisional displacements occur at the low energy part of the cascade, which can be considered isotropic, the cascade mixing can be treated as a random-walk process. This leads to the definition of a "diffusion coefficient", D_{cas}. The diffusion coefficient is given by [47]:

$$D_{cas} = \frac{1}{6} \lambda^2 N_D' \qquad (2.22)$$

where, λ is the rms separation for vacancy-interstitial pair, and N_D' is the rate of atomic displacement.

An alternative derivation of D_{cas} has been proposed for dense cascades, it leads to [47]:

$$D_{cas} = \frac{1}{6} \frac{rd}{E_d N} \left(\frac{dE}{dx} \right) \phi' \qquad (2.23)$$

where, r is the mean free path between atomic collisions

N is the atomic density of the solid

d is the diameter of the cascade,

and ϕ' is the irradiation dose rate.

Since λ, r and d are in the nanometer range, both Eq. (2.22) and Eq. (2.23) will give diffusion coefficients of the same order of magnitude.

The implication of the above equations is that the rate of mixing decreases if the nuclear stopping power, the ion flux, or the mean free path decreases. It is important to note that the model does not describe diffusion of atoms within the microstructure of a developing secondary cascade, but only their diffusion averaged over times which are very long compared to the cascade life time. Thus, D_{cas} can be made arbitrarily small by reducing the beam current [48].

2.3.2 Radiation enhanced diffusion

Ion bombardment causes an increase in vacancy concentration resulting in a proportional increase in diffusion by a vacancy mechanism. Also, substitutional atoms are ejected into interstitial sites, from which they diffuse rapidly. These two mechanisms lead to an enhancement in thermally activated diffusion. The basic equations describing enhanced diffusion in a crystalline solid are [49,50]:

$$\frac{\partial C_v}{\partial t} = D_v \frac{\partial^2 C_v}{\partial x^2} + \alpha P - \frac{D_v}{\ell^2}(C_v - C_v^{th}) - 4\pi R_{iv} N D_{in} C_v C_{in}, \qquad (2.24)$$

$$\frac{\partial C_{in}}{\partial t} = D_{in} \frac{\partial^2 C_{in}}{\partial x^2} + \alpha P - \frac{D_{in}}{\ell^2} C_{in} - 4\pi R_{iv} N D_{in} C_v C_{in}, \qquad (2.25)$$

$$D_{enh} = C_v D_v + C_{in} D_{in} \qquad (2.26)$$

where,

C_v is the total atomic fraction of vacancies,

C_v^{th} is the vacancy concentration without irradiation,

C_{in} is the atomic fraction of interstitials,

P is the production rate of vacancy-interstitial pairs per target atom,

α is the fraction of point defects that escape the cascade to migrate freely,

ℓ is a characteristic diffusion length to fixed annihilation sites,

N is the atomic density,

R_{iv} is the vacancy-interstitial separation at which spontaneous recombination occurs,

and D_{enh} is the enhanced atomic diffusion coefficient.

The terms on the right-hand side of Eq. (2.24) and Eq. (2.25) represent: defect diffusion, defect production and defect annihilation. The equations can be solved numerically [51] for a specific case. However, an approximate analytical expression for D_{enh} can be obtained. Assuming a steady state, where creation and annihilation are balanced, and assuming that C_v and C_{in} are constant over a distance ℓ, we get [49]:

$$D_{enh} = \frac{-D_v}{4\pi N R_{iv} \ell^2} + \left[\left(\frac{D_v}{4\pi N R_{iv} \ell^2} + C_v^{th} D_v \right)^2 + \frac{\alpha P}{\pi N R_{iv}} \right]^{1/2} \quad (2.27)$$

Eq. (2.26) can be simplified by considering three regimes:

i) At high temperature, the normal diffusion dominates, then

$$D_{enh} = D_v C^{th} = D , \quad (2.28)$$

where D is the unenhanced diffusion coefficient.

ii) At lower temperatures, where diffusion is enhanced and point defects annihilate mostly at fixed sinks:

$$D_{enh} = 2\alpha P \ell^2 . \quad (2.29)$$

The diffusion coefficient is independent of temperature.

iii) At still lower temperatures, where annihilation occurs mainly by recombination:

$$D_{enh} = \sqrt{\frac{\alpha P D_v}{\pi N R_{iv}}}. \qquad (2.30)$$

This leads to an activation energy, E_A of one-half of the vacancy migration energy.

In a bulk-polycrystalline material, diffusion along grain boundaries (GB) occurs. GB diffusion can be seldom decoupled from the lattice diffusion [52]. The diffusing species may "leak" into the adjoining lattice. This has led to the proposal of three types of diffusion kinetics (A, B and C) according to the extent of that leakage [53] as shown in Fig. (2.5). In A-kinetics, diffusion fields from adjoining grains are assumed to be overlapping. In B-kinetics, grain boundaries are assumed to be isolated. In C-kinetics, grain boundary diffusion is assumed dominant (i.e. lattice diffusion is assumed insignificant). The grain structure can influence both the extent of coupling between lattice and grain boundary diffusion and the intrinsic nature of grain boundary diffusion. This aspect has not been investigated extensively [52]. As far as ion-beam-mixing models are concerned, the GB and lattice diffusion can be considered the components of an effective non-enhanced diffusion. If the grain structure undergoes fundamental structural changes as a result of ion bombardment, GB diffusion will be radiation dependent; the need may then arise to decouple the lattice and GB diffusion for improved modelling of ion beam mixing.

2.3.3 Spike effects

A model considering the effect of spikes on mixing was proposed recently [54]. The model considers marker atoms migrating over spherical region of the spike with a diffusivity $D_{sp}(t)$ which is spatially uniform but has a time dependence of the form:

$$D_{sp}(t) = D_{osp}\, C(t)\, \exp\left(-E_m/K_B\, T(t)\right). \qquad (2.31)$$

where,

D_{osp} is a spike independent constant,

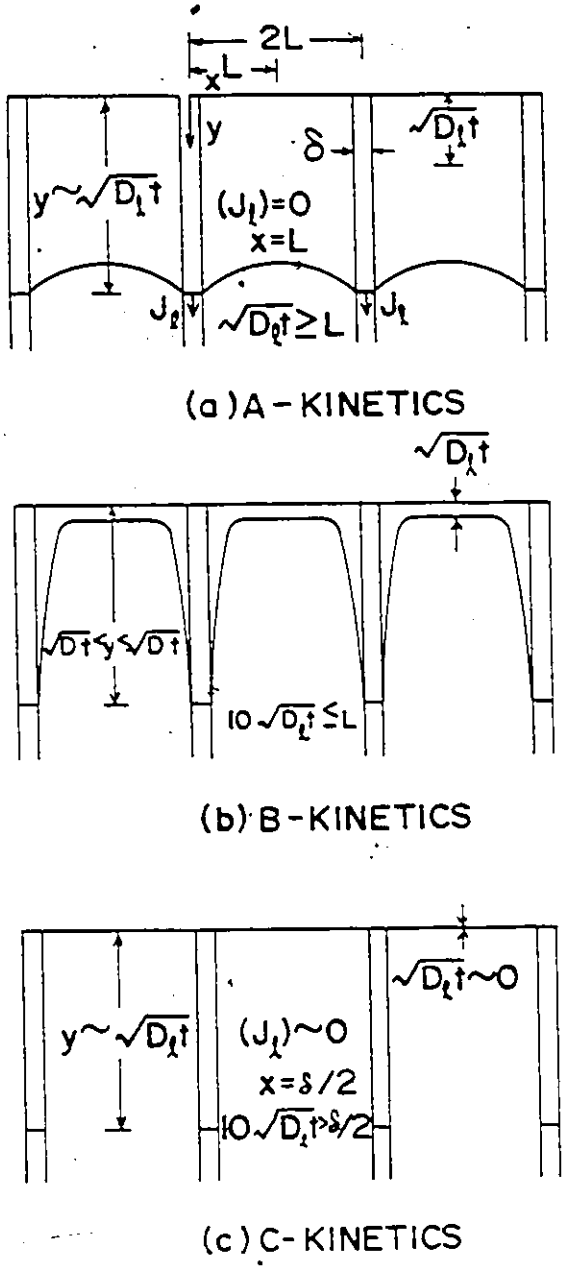

Fig. (2.5) Schematic representations of A-, B-, and C-kinetics of grain boundary diffusion. Vertical lines indicate grain boundaries and curved lines are isoconcentration contours. The diffusion source coincides with the top horizontal lines (Ref.[79]).

C(t) is the time-dependent defect concentration,

T(t) is the time-dependent spike temperature (spatially uniform),

K_B is Boltzman constant,

and E_m is the marker-atom migration energy.

Displacements of marker atoms through successive spikes add up to a random walk with isotropic jumps.

The contribution to mixing was measured in terms of the parameter Y, given by:

$$Y = <\Delta x^2>_{sp}/2\phi F_D D_{osp} \qquad (2.32)$$

where,

$<\Delta x^2>_{sp}$ is the variance of the marker spreading due to spike effects only,

and

F_D is the damage energy deposited per ion per unit length.

Dividing by ϕF_D gives a measure of the effectiveness of the ion in promoting the mixing; dividing by D_{osp} helps to determine the effectiveness of spike characteristics. It was explained [54] that the model predicts little variation in the mixing parameter, Y, from ion to ion for a given target, or from target to target for metal hosts. The model predicts that mixing is sensitive to the value of defect migration energy. The authors [54] pointed out that direct comparison with experiment is very difficult because of the difficulty in finding an accurate value for D_{osp}.

An alternative model was proposed earlier [55] where normal thermal reaction processes were assumed for the duration of the spike. The temperature is assumed constant for time t_o, followed by an instantaneous drop to ambient temperature. The reaction rate in each spike volume is thus proportional to $\exp(-E_m/K_B(T_o+T))$ where T is the sample temperature.

Applying the conventional furnace annealing formula, modified to account for the repetitive nature of ion irradiation, the thickness of the formed compound, x, will be:

$$X^2 = A_o \phi\, t_o\, a_s \exp{-(E_m/K_B(T_o+T))} \tag{2.33}$$

or

$$X = B_o \phi\, t_o\, a_s \exp{-(E_m/K_B\,(T_o+T)} \tag{2.34}$$

where, t_o is the spike duration, ϕ is the ion flux and a_s is the effective area of the spike. A and B are pre-exponential factors for parabolic and linear growth rates, respectively.

This model predicts that the apparent activation energy of mixing is a function of the temperature of the material, T_o.

The most important model paramters, for Cr/Si system, were calculated to be

$E_m = 0.2\,eV$

$T_o = 1250\,K$

$t_o = .5 \times 10^{-11}$ sec.

2.3.4 Chemical effects

Chemical effects can influence the mixing process. This was put forward to account for differences in mixing in collisionally similar, but chemically different systems [56]. Johnson et al. [57] considered the enhancement/inhibition of mixing of binary metal alloy due to chemical effects by introducing a diffusion coefficient D_{ch}. The main idea is that the mixing of an A/B system can be described by a diffusion equation of the form:

$$\frac{\partial C_A}{\partial t} = D_{ch} \nabla^2 C_A \tag{2.35}$$

where, $C_A = 1 - C_B$ is the fractional concentration of A. The diffusivity D_{ch} is given by:

$$D_{ch} = D^o_{ch} \left(1 + \frac{4\delta}{K_B T} C_A C_B\right) \tag{2.36}$$

where, $D^o_{ch} = D^o_A C_B + D^o_B C_A$,

D^o_A and D^o_B are self-diffusivities.

and $$\delta = Z\,(V_{AB} - \frac{1}{2}\,(V_{AA} + V_{BB}))\,.$$

The V's are pair enthalpies and Z is the coordination number (assumed constant). Thus, δ represents the chemical preference of A-atoms to be surrounded by B-atoms and vice versa.

Although mixing rates calculated by Eq. (2.36) give reasonable correlation with heats of mixing [57], nevertheless, the form of Eq. (2.36), for spatially dependent D, does not conserve particles [56] because it does not have the form:

$$\frac{\partial c}{\partial t} = \text{div}\,(D\ \text{grad}c) \tag{2.37}$$

Also, the equilibrium distribution in one dimension as ($t \rightarrow \infty$ and $\partial c/\partial t \rightarrow 0$) is independent of δ; i.e., the equilibrium state is independent of the chemical preference. This represents a self-inconsistency in the model.

2.4 Ion beam mixing experiments

Several experimental techniques have been used in the study of ion-beam mixing. The main techniques are:

- Rutherford Backscattering Spectrometry (RBS) for measuring the amount of mixing and average composition.
- Auger Electron Spectroscopy (AES) for determining the composition
- X-rays for detecting compound formation and crystal-structure changes.
- Transmission Electron Microscopy (TEM) for microstructure investigatons.

RBS is the dominant technique in all ion-beam-mixing investigations.

Various parameters are used to characterize the mixing process: primary parameters measurable by an experimental technique, and calculated parameters using one or more of the models discussed in Section (2.3) or similar models. The primary parameters include:

- The number of atoms crossing an interface; this parameter is mainly used for bilayer systems.
- The mean-square value of the spreading of a marker.
- The ratio of the square-value of the thickness of the mixed layer, $(\Delta x)^2$, to the corresponding ion dose, ϕ. This gives a measure for mixing efficiency. The parameter can be more informative when normalized to the efficiency of a selected ion A, i.e., when expressed for an ion i as:

$$[(\Delta x)^2/\phi]_i/[(\Delta x)^2/\phi]_A$$

The parameters calculated to fit a model are mainly an effective diffusion coefficient, D, or an effective diffusion length, $(Dt)^{1/2}$. An efficiency parameter ($Dt/\phi F_D$) is also used (where F_D is the elastic energy deposited per unit length).

In the following paragraphs, major experimental findings will be discussed. The aspects that will be addressed are: the effect of the temperature of the target during irradiation, the influence of beam parameters, the changes occuring in the spatial distribution of elements (profiles) and the microstructure.

2.4.1 Temperature

Most of the reported systems show a temperature dependence of the type shown in Fig. (2.6) for Nb/Si system [58]. The temperature dependence can be divided, approximately, into two regions: low temperature (below certain critical temperature, T_c) and high temperature (above T_c). Below T_c, mixing is independent of temperature for both markers and bilayers [59] with the exception of Fe/Pt system which shows a step in the temperature-dependence curve at about 25 K [60]. For Si/Ge system, some results show temperature variation [61], while others [62,63] show no temperature dependence. At high temperatures,

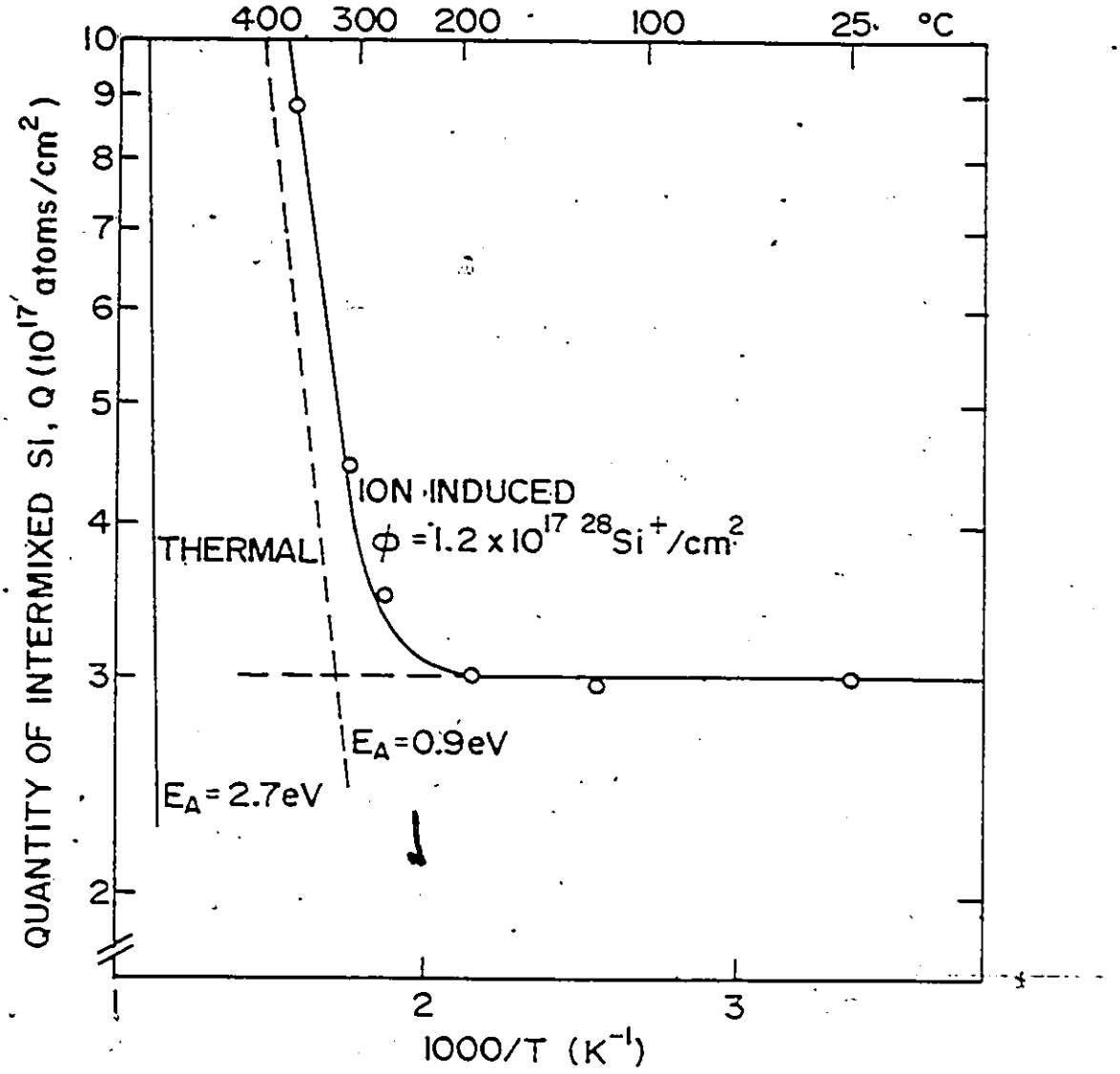

Fig. (2.6) Temperature dependence of mixing Nb and Si layers under Si^+ irradiation (from Ref. [58]).

mixing increases with increasing temperature. The critical temperature, T_c, occurs, generally, in the range from about 160 K [64] to about 470 K[58].

These findings can be understood in terms of the models discussed in Section (2.2): at high temperature, radiation enhanced diffusion occurs and at low temperature cascade mixing dominates.

2.4.2 Beam Parameters

A) Mass and Energy

The mass and energy of the mixing ions determine their range in a given target and accordingly the energy density distribution. The general trend is that the mixing proceeds faster as the energy deposited at the interface increases. Fig. (2.7) shows, for example, the case of Al/Au system irradiated with 140 KeV and 200 KeV Kr^+ [65]. The compound formation occurs faster for irradiation with 200 KeV than for 140 KeV Kr^+. For 140 Kr^+ bombarding Al and Au, the calculated values of the reduced energy, ε (see Eq. (2.3)) are 0.47 and 0.2 respectively. These values will be 0.6 and 0.3 for 200 KeV Kr^+. For Al-Au alloys, the values of ε depend on the composition, but it will not exceed the values for Au. Then, it can be seen, from Fig. (2.2), that S_n is larger for 200 KeV Kr^+ than for 140 KeV Kr^+. The variation of the mixing efficiency, ξ with ion mass irradiating Pt/Si system [66] is shown in Fig. (2.8); ξ_i increases as the atomic mass of the irradiating ions increases.

The calculated parameter Dt varies linearly with F_D at low temperatures (below T_c) for W markers in Al, and Au markers in Al_2O_3 and SiO_2 for irradiation with Ne^+, Ar^+, and Kr^+ [67]. These findings agree with the collisional cascade models (see Section (2.2)). However, recent results of mixing Au markers in Si show

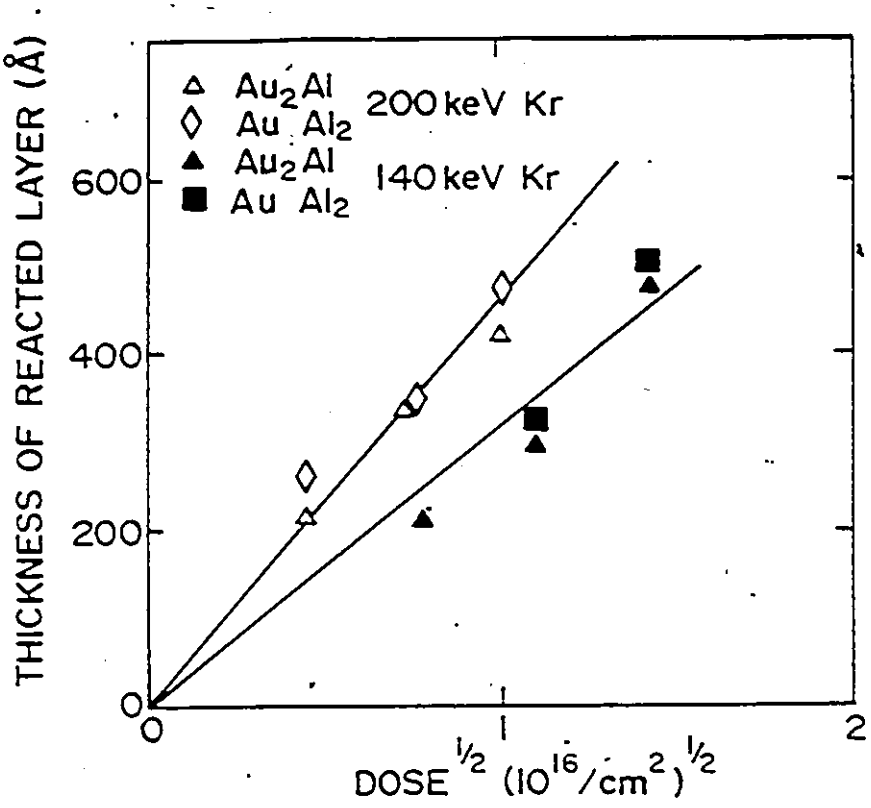

Fig. (2.7) Dependence of mixing on dose and energy of the bombardment ions (Ref. [65]).

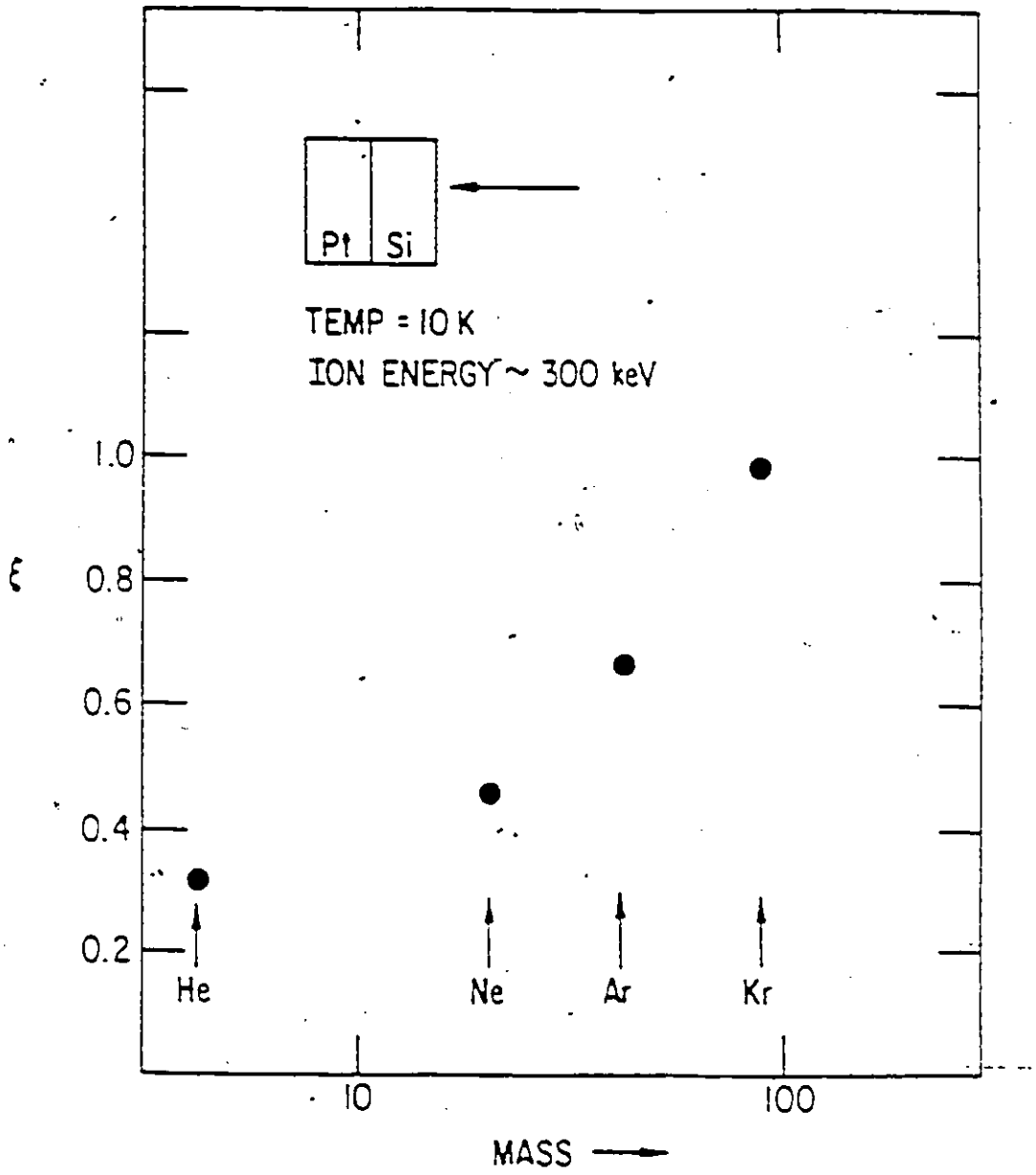

Fig. (2.8) The dependence of mixing efficiency on the mass of the irradiating ions (from Ref. [66]).

a non-linear relation between F_D and Dt. This deviation from collisional models may be due to diffusion by interstitial mechanism [67,68].

The results of mixing Au markers in Ni using N^+, Ne^+, Ar^+, Sb^+ and Xe^+ [69] suggest that the deviation from collisional models is substantial for light ions implying a major role of interstitial-diffusion mechanism. For heavier ions, the dense collision cascades seem to suppress the influence of mechanisms other than collisional ones.

B) Dose and dose rate

For furnace annealing, the spread, Δx, of a marker is given in [70]:

$$(\Delta x)^2 = 2Dt \qquad (2.36)$$

where, D is the diffusion coefficient and t is the time.

Eq. (2.36) can be used for the case of a marker spreading due to ion irradiation. The irradiation time t is (ϕ/ϕ'), where ϕ is the dose and ϕ' is the dose rate. This leads to:

$$(\Delta x)^2 = 2\,Dt = \beta\phi \qquad (2.37)$$

where, β is a constant.

Eq. (2.37) was found to be applicable in most of the investigated systems [71]. Fig. (2.8) shows an example of such findings. However, a linear dependence of Δx on ϕ was reported for Au/Si and Au/Ge bilayer systems [72]. The simple explanation of this "deviation" is that the model applies only for dilute alloys in homogenous matrix. It is important to note that for Au markers in Si, it was found previously [73] that Eq. (2.37) is applicable. Linear variations of Δx with ϕ was reported also for Ti/Si bilayer system [74], and $\Delta x \propto \phi^{0.7}$ was reported for Ti/Ni bilayer system [2,75]. Again, the model is not applicable in these cases.

Dose rate, ϕ', was found to have no effect on Dt at low temperatures ($T < T_c$) for Ni/Si bilayer system [76], Pt markers in Fe [77], and Au markers in Ni [78]. Similar results were found for Ni/Si bilayer system at high temperatures ($T > T_c$) [78]. A decrease of about 20% in Dt with increasing ϕ was reported for Au marker in Ni. This effect disappeared above $T_c + 100$ K [78].

2.4.3 Profiles and microstructure

The profiles of marker systems are nearly always Gaussian after ion irradiation [71]. The exceptions are Pd(Si) systems [79,80] and Si(Pt) at 500 K [80]. The profiles of bilayer systems are of the form of error functions, after irradiation at low temperatures [71]. The Ni/Si [76] and Nb/Si [58] systems appear to have small steps superimposed on them after low temperature irradiation. These correspond to layers of fixed composition. Compound formation has been reported only for Al/Au [65]. It is important to note that the analysis of this system was done at room temperature. At T_c and above, many bilayer systems develop well-defined layers of fixed composition which have been identified by x-ray diffraction to contain single crystalline phase [71].

Amorphization due to ion-beam mixing was observed in some systems (e.g. Au/V [81], Au/Co [81], and Ni/Mo [82]); retained crystallinity was observed in some other systems (e.g. Au/Ni [81], and Ag/Cu [83]). Liu et al. [82] proposed that it is the crystal-structure difference of the two constituent metals that plays the key role in ion-induced amorphization; atomic size and electronegativity effects are minor. Brimhall et al. [84] suggested that a limited compositional range of solubility is a better criterion for amorphous phase formation. Jaouen et al. [85] proposed that the ratio of irradiation temperature to solidification temperature can be an important factor, since at a given temperature the stable phase results

from the balance between thermal ordering and radiation induced disordering; amorphization will occur when the disordering is high.

Another structural feature that was observed to occur due to ion-beam mixing is grain growth. For example, in Au/Ni multilayer system [86], irradiation with 300 KeV Xe^+ leads to an increase in grain size from about 200 Å to about 1500 Å. This growth was attributed to the increase in film thickness from about 100 Å for as-deposited Au and Ni layers to about 800 Å Au/Ni alloy film [86]. It was observed [87], however, that grain growth occurs due to irradiation while the film thickness is not increasing but rather decreasing due to sputtering. This implies that there may be more than one mechanism contributing to grain growth in ion- mixed systems.

CHAPTER III

THIN FILM THERMOELECTRICS

3.1 The thermoelectric phenomenon

The reversible thermoelectric phenomenon reveals itself in either of three related effects [88]:

i) Seebeck effect

The Seebeck effect is the creation of an electric potential difference, V_s, between the terminals of a conductor as a result of the application of a temperature gradient across it. In order to observe the effect, we have to have a circuit composed of two different materials or perhaps the same material in two different states, e.g., different doping (See Fig. (3.1a)). It should be emphasized, however, that the thermoelectric properties are intrinsic characteristics of a material as much as electrical and thermal conductivities are. The necessity of two materials for the measurements arises because of technical reasons.

Seebeck coefficient, or the thermoelectric power of a material, S, is defined as:

$$S = \frac{dV_s}{dT} \tag{3.1}$$

where T is the temperature.

ii) Peltier effect

The Peltier effect is the reversible generation or absorption of heat at the junction between two different conductors due to an electric current passing through the junction. The direction of the heat exchange depends on the direction of the electric

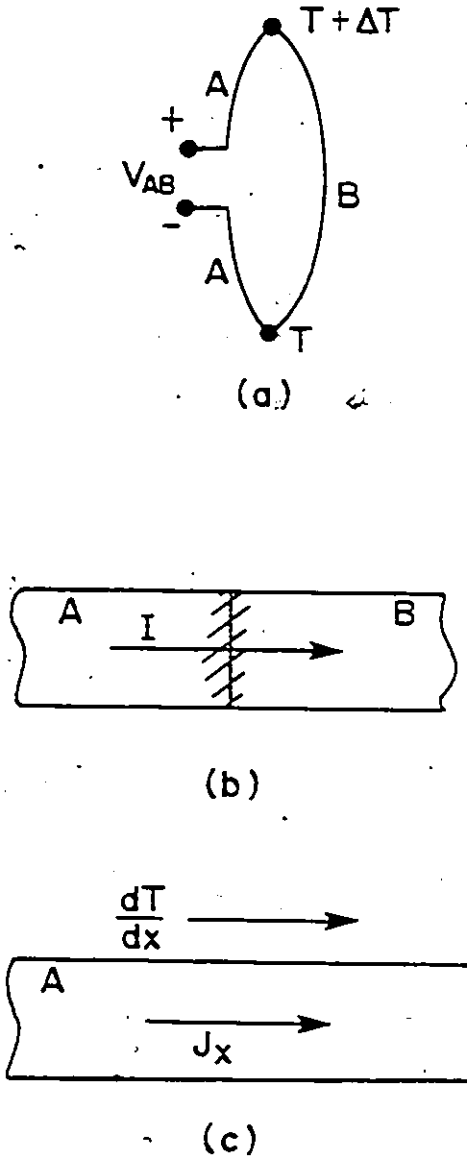

Fig. (3.1) The thermoelectric phenomenon (See text for details)
a) Seebeck effect
b) Peltier effect
c) Thomson effect

current; the magnitude depends on the junction temperature. Peltier heat at the junction, π_{AB}, is defined as the reversible heat developed per unit time per unit electric current in the direction A to B (See Fig. (3.1b)).

iii) **Thomson effect**

The Thomson effect is the reversible generation or absorption of heat due to an electric current passing through a conductor across which a temperature gradient, dT/dx, exists (See Fig. (3.1c)). The total heat produced in a conductor per unit volume per second, Q', due to an electric current of density J_x passing through the conductor is given by:

$$Q' = \frac{J_x^2}{\sigma} - \sigma_T J_x \frac{dT}{dx} \tag{3.2}$$

where, σ is the electrical conductivity and σ_T is defined as the Thomson heat of the conductor. The first term of Eq. (3.2) is the irreversible Joule heat. The second term is the reversible heat due to the Thomson effect; it depends on temperature and increases linearly with the electric current, the direction of which determines the direction of the heat exchange.

Thomson derived the relations between the thermoelectric power, S, the Peltier heat, π, and the Thomson heat, σ_T; they are given by [88]:

$$\sigma_T = \frac{TdS}{dT} \tag{3.3}$$

$$\pi = T S \tag{3.4}$$

Since Seebeck effect is the manifestation underlying the conversion of heat into electrical power, it will be considered in more detail in the following section.

3.2 The thermoelectric power

An electric potential difference, V_s, develops between the terminals of a conductor across which a temperature gradient exists. This is because electrons at the hot end acquire higher energy than those at the cold end and diffuse toward the cold end. Hence, an accumulation of negative charge occurs at the cold end, resulting in the creation of an electric potential difference. The temperature gradient leads also to the creation of a phonon flux flowing from the hot to the cold end. A phonon can interact with other phonons and with electrons and an appropriate mean free path, ℓ, can be ascribed to each of these interactions. At low temperatures, the phonon-electron interaction exceeds the phonon-phonon interaction; $\ell_{p,p} > \ell_{p,e}$. The electrons can receive energy from phonons. The phonon flux in effect "drags" electrons with it towards the cold end leading to an extra contribution to the thermoelectric power, known as the phonon drag component. At high temperatures ($T > \theta_D$, where θ_D is Debye temperature = 119 K for Bi), the phonon-phonon interaction exceeds greatly the phonon-electron interaction; $\ell_{p,p} < \ell_{p,e}$. Phonons will not then create an extra component of the thermoelectric power. However, the lattice still influences the thermoelectric power by scattering electrons moving under the influence of the temperature gradient. The total thermoelectric power can be expressed, in general, as [89]:

$$S = S_D + S_g \tag{3.5}$$

where, S_D and S_g are the contributions from electronic diffusion and phonon drag, respectively. At ordinary temperatures (300-400 K), $S = S_D$, the term S_g will not be referred to any further.

In order to obtain a general expression for S, we can start by writing the transport equations using the definitions of Section (3.1). Then, we derive the transport equations from Boltzman approach. A comparison between the two sets of equations obtained by the two approaches leads to a general expression for S [89].

The transport equations, assuming a temperature gradient in the x-direction, can be written as

$$J_x = \varepsilon_x \sigma - S\sigma \frac{dT}{dx} \tag{3.6}$$

$$(J_u)_x = -K \frac{dT}{dx} + ST J_x \tag{3.7}$$

where, J_x is the electrical current density,

ε_x is the developed electric field,

σ is the electrical conductivity,

J_u is the heat current density,

and K is the thermal conductivity.

Now, if a steady state exists under the action of temperature and potential gradients, and if f is the electron distribution function, then Boltzman equation can be written as:

$$\left[\frac{\partial f}{\partial t}\right]_{field} - \left[\frac{\partial f}{\partial t}\right]_{collisional} = 0 \tag{3.8}$$

The second term of Eq. (3.8) can be expressed as:

$$\left[\frac{\partial f}{\partial t}\right]_{collisional} = -\frac{f - f_o}{\tau} \tag{3.9}$$

where f_o is the equilibrium distribution function under no external forces,

and τ is the characteristic relaxation time related to some mean time between collisions of the particles involved; it is a function of energy and momentum in the crystal.

The field term can be determined by considering that under the influence of an electric field, ε_x, electrons with mass m, and charge e will have an acceleration given by:

$$\frac{du_x}{dt} = \frac{e\varepsilon_x}{m} \tag{3.10}$$

where u_x is the velocity of the electron.

It follows that:

$$\left[\frac{\partial f}{\partial t}\right]_{field} = \frac{f(u_x + \frac{e\,\varepsilon_x}{m}dt,\, x + u_x dt,\, t+dt) - f(u_x,\, x,\, t)}{dt} \tag{3.11}$$

or

$$\left[\frac{\partial f}{\partial t}\right]_{field} = \frac{\partial f}{\partial t} + \frac{e\,\varepsilon_x}{m}\frac{\partial f}{\partial u_x} + u_x\frac{\partial f}{\partial x} \tag{3.12}$$

Eq. (3.12) can be rewritten in terms of wave number k, where mu = hk/2π, leading to:

$$\left[\frac{\partial f}{\partial t}\right]_{field} = \frac{2\pi e\,\varepsilon_x}{h}\frac{\partial f}{\partial k_x} + u_x\frac{\partial f}{\partial x} \tag{3.13}$$

Eqs. (3.8), (3.9), and (3.13) lead to:

$$\frac{2\pi e}{h}\varepsilon_x\frac{\partial f}{\partial k_x} + u_x\frac{\partial f}{\partial x} = -\frac{f-f_o}{\tau} \tag{3.14}$$

or

$$f = f_o - \tau(k)\left[\frac{2\pi e}{h}\varepsilon_x\frac{\partial f_o}{\partial k_x} + u_x\frac{\partial f_o}{\partial x}\right] \tag{3.15}$$

The electric current density, J, and the heat current density, J_u, can be expressed in terms of f as:

$$J = \frac{e}{4\pi^3}\iiint u\,f\,dk \tag{3.16}$$

$$J_u = \frac{1}{4\pi^3}\iiint u\,E f\,dk \tag{3.17}$$

Eqs. (3.15), (3.16) and (3.17), with some mathematical manipulations, can lead to [89]:

$$J_x = [e^2 M_o]\varepsilon_x + |e|\left[-\frac{E_F}{T}M_o + \frac{1}{T}M_1\right]\frac{dT}{dx} \tag{3.18}$$

and

$$(J_u)_x = -[|e|M_1]\varepsilon_x - \left[-\frac{E_F}{T}M_1 + \frac{1}{T}M_2\right]\frac{dT}{dx} \tag{3.19}$$

where, E_F is the Fermi energy,

$$M_n = \phi_n(E_F) + \frac{\pi^2}{6}(K_B T)^2\frac{d^2}{dE_F^2}\phi_n(E_F) + \ldots,$$

and

$$\Phi_n = \frac{E^n}{\pi h^2} \int\int \left(\frac{\partial E}{\partial k_x}\right)^2 \frac{\tau(k)\, dA}{\nabla_k E}$$

with A being the Fermi surface area.

Comparison with Eq. (3.6) leads to:

$$\sigma = e^2 M_0 \tag{3.20}$$

and

$$S = \frac{1}{|e|T}\left[\frac{M_1}{M_0} - E_F\right] \tag{3.21}$$

To the first order of T we have:

$$\sigma = \frac{e^2}{\pi h^2} \int\int \left(\frac{\partial E}{\partial k_x}\right)^2 \frac{\tau(k) dA}{\nabla_k E} \tag{3.22}$$

Then, it can be shown, for $E_f >> K_B T$, that:

$$S = \frac{\pi^2 K_B^2 T}{3|e|}\left[\frac{\partial}{\partial E} \ln \sigma(E)\right]_{E=E_F} \tag{3.23}$$

In the case of a spherical Fermi surface with isotropic τ, we have:

$$\left(\frac{\partial E}{\partial x}\right)^2 = \left(\frac{h u_x}{2\pi}\right)^2 = \frac{1}{3}\left(\frac{h u}{2\pi}\right)^2 \tag{3.24}$$

and

$$\nabla_k E = hu \tag{3.25}$$

This will lead to:

$$\sigma(E) = \frac{e^2 u \tau}{6\pi^2 h} \int\int dA$$

$$= \frac{e^2}{6\pi^2 h} \ell A \tag{3.26}$$

where, $\ell = \tau u$ is the mean free path of all the electrons.

The thermoelectric power will then be given by:

$$S = \frac{\pi^2 K_B^2 T}{3e}\left[\frac{1}{A}\frac{\partial A}{\partial E} + \frac{1}{\ell}\frac{\partial \ell}{\partial E}\right]_{E=E_F} \tag{3.27}$$

or

$$S = \frac{\pi^2 K_B^2 T}{3e E_F} (U + V) \tag{3.28}$$

where,

$$U = \left(\frac{\partial \ln \ell}{\partial \ln E} \right)_{E=E_F}$$

and

$$V = \left(\frac{\partial \ln A}{\partial \ln E} \right)_{E=E_F}$$

If $\tau(\mathbf{k})$ and U are anisotropic, the Fermi surface may be divided into regions characterized by isotropic velocities and relaxation times. The conductivity may then be written as [89]:

$$\sigma = \frac{e^2}{6 \pi^2 h} \sum_i \ell_i A_i \tag{3.29}$$

and the thermoelectric power:

$$S = \frac{\pi^2 K_B^2 T}{3e} \frac{\partial}{\partial E} \left(\sum_i \ell_i A_i \right) / \ell_i A_i \tag{3.30}$$

It should be noted that if we write S_i as the thermoelectric power of the ith region defined by:

$$S_i = \frac{\pi^2 K_B^2 T}{3e} \frac{\partial}{\partial E} (\ell_i A_i) / \ell_i A_i \tag{3.31}$$

Then, it follows that:

$$S = \left(\sum_i \sigma_i S_i \right) / \sum_i \sigma_i \tag{3.32}$$

This result may be applied directly to the case of a single conductor which has a number of independent groups of charge carriers 1,2,... with conductivities σ_1, σ_2, ..., and such that each group, if acting alone, contributes thermoelectric powers S_1, S_2, ..., respectively [90].

This result will be used later for the case of a partially mixed alloy to find a value for S as a function of the mixing dose.

The analysis of the thermoelectric power given above is quite general. The results apply even for non-spherical surfaces in the k-space. To obtain more tangible results (but approximate), we can use in the Boltzman equation the Fermi-Dirac distribution given by

$$f(E) = \left[1 + \exp\left(\frac{E - E_F}{K_B T}\right)\right]^{-1} \tag{3.33}$$

where E_F is the Fermi energy,

and K_B is the Boltzman constant.

Then we assume that:

$$\tau \propto E^b \tag{3.34}$$

where,

$$b = \begin{cases} -\frac{1}{2} & \text{for lattice scattering.} \\ +\frac{3}{2} & \text{for ionized-impurity scattering.} \end{cases}$$

This leads to an expression for the thermoelectric power given by [91]:

$$S = -\frac{K_B}{e}\left[-\eta + \frac{(b+5/2)\,F_{b+3/2}(\eta)}{(b+3/2)\,F_{b+1/2}(\eta)}\right] \tag{3.35}$$

where

$$F_r(\eta) = \int_0^\infty \xi^r \cdot \frac{1}{1 + \exp(\xi - \eta + 1)}\, d\xi ,$$

$$\eta = \frac{E_F}{K_B T} ,$$

and

$$\xi = \frac{E}{K_B T} .$$

Numerical values of $F_r(\eta)$ are tabulated in Ref. [92] for various values of r and η.

For intrinsic and moderately doped semiconductors, where $|\eta| > 4$, Eq. (3.35) can be simplified to [91]:

$$S = -\frac{K_B}{e}\left[b + \frac{5}{2} - \eta\right] \tag{3.36}$$

Eq. (3.36) shows that the larger the value of the reduced Fermi energy, η, the larger the value of S (η is negative). The thermoelectric power increases as the Fermi energy moves further into the energy gap from the bottom edge of the conduction band.

In a thin film, where thickness is comparable with the electron mean free path, a geometrical limitation is imposed on the motion of electrons by the film boundaries. The physical effects arising from this limitation are known as "size effects". A specularity parameter, p_o, was used [93] as a measure of the deviation from bulk behaviour due to size effect. This parameter becomes unity for perfect specular scattering and zero for diffuse scattering. An expression for the thermoelectric power in a thin film, S_F, relative to that in the bulk, S_B, was obtained assuming scattering of charge carriers at the surface and in the bulk are additive processes. It is given by [93]:

$$S_F = S_B\left[1 - \frac{3}{8}\,\frac{1-p_o}{\gamma}\cdot\frac{U}{1+U}\right] \quad , \quad \gamma >> 1 \tag{3.37}$$

and

$$S_F = S_B\left[1 + \frac{\ln\gamma - 1.42}{\ln\gamma - 0.42}\,\frac{U}{1+U}\right] \quad , \quad \gamma << p_o \simeq 0 \tag{3.38}$$

where γ is the ratio of the mean free path to the film thickness.

The validity of Eqs. (3.37) and (3.38) has been verified experimentally [94]. However, it should be noted that for very thin films quantum size effects [95] may appear and produce appreciable effect on the physical characteristics of the film.

A summary of the reported values of the thermoelectric power of various materials prepared in the thin film form is given in Tables (3.1) and (3.2). The thermoelectric power of a material in a thin film form is usually less than that of the same material in the bulk form

with the exception of Pb-Se (see Table (3.1)). It is interesting to note that the values of S for chromium, given in Table (3.1), show the first reported change of the sign of the thermoelectric power with thickness in metals. A comparison between the values of S given in Tables (3.1) and (3.2) leads to the conclusion that semiconductors, semimetals, and their alloys have, in general, higher values of S than metals and metallic alloys.

3.3 Materials assessment

For energy conversion applications, the efficiency, η_c, is a parameter that one desires to maximize. The efficiency of a thermoelectric generator, working between temperatures T_0 and T_1, can be expressed as:

$$\eta_c = \frac{T_1 - T_o}{T_1} f(Z) \tag{3.39}$$

where, f(Z) is a function of the material parameters and becomes a maximum when Z, the figure of merit, is maximum. The figure of merit is given by [88]:

$$Z = \frac{S^2 \sigma}{K} \tag{3.40}$$

where K is the thermal conductivity $= K_c + K_\ell$, and K_ℓ and K_c are the lattice and carrier thermal conductivities, respectively.

From Eq. (3.40) one can conclude that to maximize Z, the ratio (σ/K) has to be maximized. This occurs in materials that have relatively low phonon conductivity, few carriers and high mobilities.

Table (3.1) Seebeck coefficients for thin film metals and metallic alloys.

Material	Thickness (nm)	Seebeck Coefficients (μV/K)	Temperature (K)	References	Comments
Copper	16.0-500.0	3.2-5.5	100-350	[96]	
Copper alloys					
$Cu_{.95}Al_{.05}$	50.0–400.0	2.5-.5 (u) 1.2-.3 (a)	300	[97,98]	u = annealed a = annealed
$Cu_{.99}Al_{.01}$	300.0	3.0 (u) 0.6			
$Cu_{.99}Sn_{.01}$	300.0	2.2 (u)			
$Cu_{.99}Ge_{.01}$	300.0	2.2 (u) 1.0 (a)		[99]	
Silver	71.2	1.165	300	[100]	Calculated from data given in Ref. [100]
Tin	40.0-150.0	1.8-4	298	[101,102]	
Chromium	100.0 10.0	+8.0 −8.0	298	[103]	
Nickel chromium (10% Cr)		33-40	50.35	[104]	
Palladium	60.0 10.0	−9.3 2.0	280 20	[103]	
Pd-Au	10.0	0.3	20	[106]	
Ytterbium	60.0 120.0	9.0 19.0	298 298	[107]	
Samarium	60.0 120.0	−15.0 0.0	298 298	[107]	
Tantalum	100.0	−9 to +1.5	298	[108]	Film prepared by rf sputtering S depends on the conditions of sputtering

Table (3.2) Seebeck coefficient for thin film semiconductor and semimetals.

Material	Thickness (nm)	Maximim S (μV/deg)	Temperature (K)	References	Comments
p-Ge	92.5	62	600	[109]	
n-Be-Sb	46.0	172	600	[109]	
a-Ge-Te	200.0	88	175-375	[109]	a = amorphous
a-Ge-Cu	>2.0	−26	340	[110]	Thickness was not clearly specified
a-Ge-Al	>2.0	470	300	[110]	at 10/% Al
a-Ge-Fe	>2.0	75	150-450	[110]	at 5% Fe; S is constant in the range 150-450 K.
a-Si:H	1.0	±200	150-400	[111]	:H = hydrogenated + and − for p- and n- types, respectively
Te	50.0-170.0	100-400	170	[112]	
Bi-Te	40.0	49.9	300	[4]	
Pb-Se	200.0-500.0	$S_F/S_B = 2.3$	7.7-350	[113]	F = film, B = bulk (2.3) is the highest ratio
Bi-Sb	1000.0	80	373	[114]	
Te-Se-Sn	265.0	500	250	[115]	
Boron-Phosphide	16 μm	−300	500	[116]	n-type
	13 μm	+500	500	[116]	p = type
	30 μm	−300	300-1000	[117]	n-type
Gallium nitride	5-30 μm	70	300	[118]	
a-Cd_3As_3	0.5-10.0 μm	−500 to 30	100-350	[119]	

Fig. (3.2) shows schematically the dependence of S, σ and K on the concentration of free carriers [88]. One may conclude that semiconductors are probably the best candidates for thermoelectric energy conversion. Nevertheless, no material is known which exhibits both high Z and high temperature capabilities.

Bi-Sb alloys can be useful in thermoelectric energy conversion because Bi is a semimetal that has a relatively low lattice thermal conductivity; alloying with antimony can create an energy gap leading to reasonable values of Z. Table (3.3) gives a comparison between the maximum reported values of Z of Bi-Sb and other semiconductors at room temperature; it shows that Bi-Sb alloys have the potential for efficient thermoelectric energy conversion.

3.4 Thin film thermoelectric generators

Thermoelectric generators are usually composed of several modules connected in parallel; each module is made up with segments of thermoelectric materials connected in series. The series connection establishes the output voltage; the parallel connection raises the output current level. An example of a thin film module is shown schematically in Fig. (3.3). The series connection is achieved using a zig-zag pattern with alternating p-type and n-type legs of the selected alloy. Thin film thermoelectric generators are capable of delivering power in the microwatt range. Fig. (3.4) shows the open circuit output voltage and the power is delivered to a matching resistive load for a generator composed of three parallel modules like the one shown in Fig. (3.3). The alloy composition for this example is:

75 wt% Bi_2Te_3 + 25 wt% Bi_2Se_2 for the n-type leg

and 25 wt% Bi_2Te_3 + 75 wt% Sb_2Te_3 for the p-type leg

The alloys were formed by coevaporation of constituent components followed by heat treatment at 250°C [123].

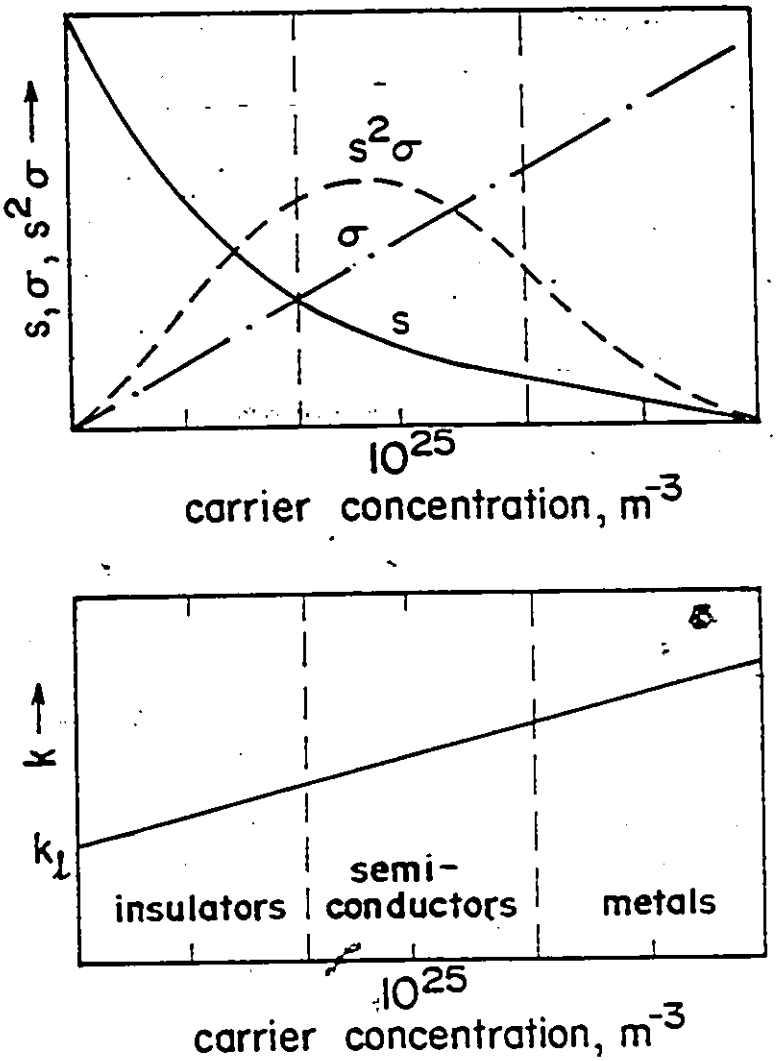

Fig. (3.2) Dependence of the thermoelectric power, S, the electrical conductivity, σ, and the thermal conductivity, K, on the concentration of free carriers (Ref. [88]).

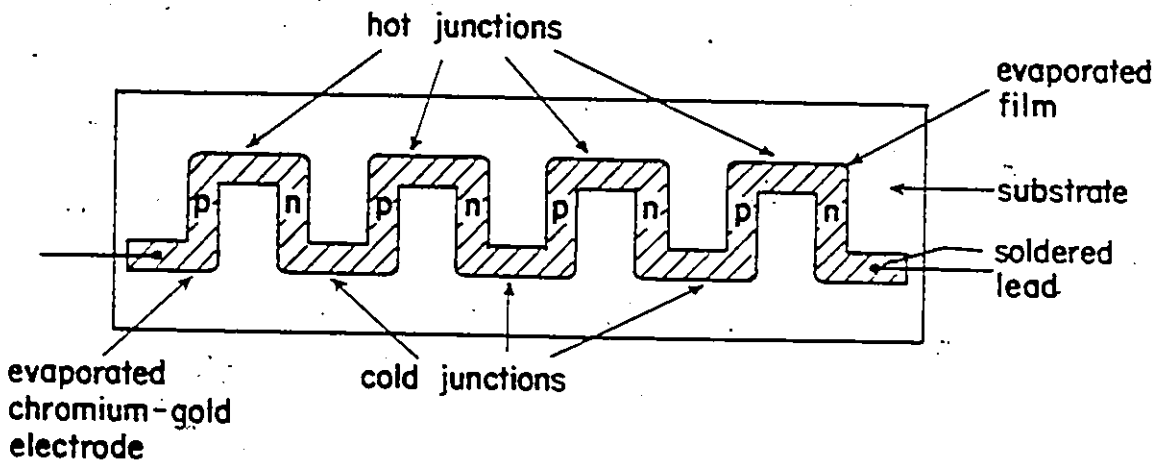

Fig. (3.3) The lateral configuration of a module of a thin film thermoelectric generator (Ref. [123]).

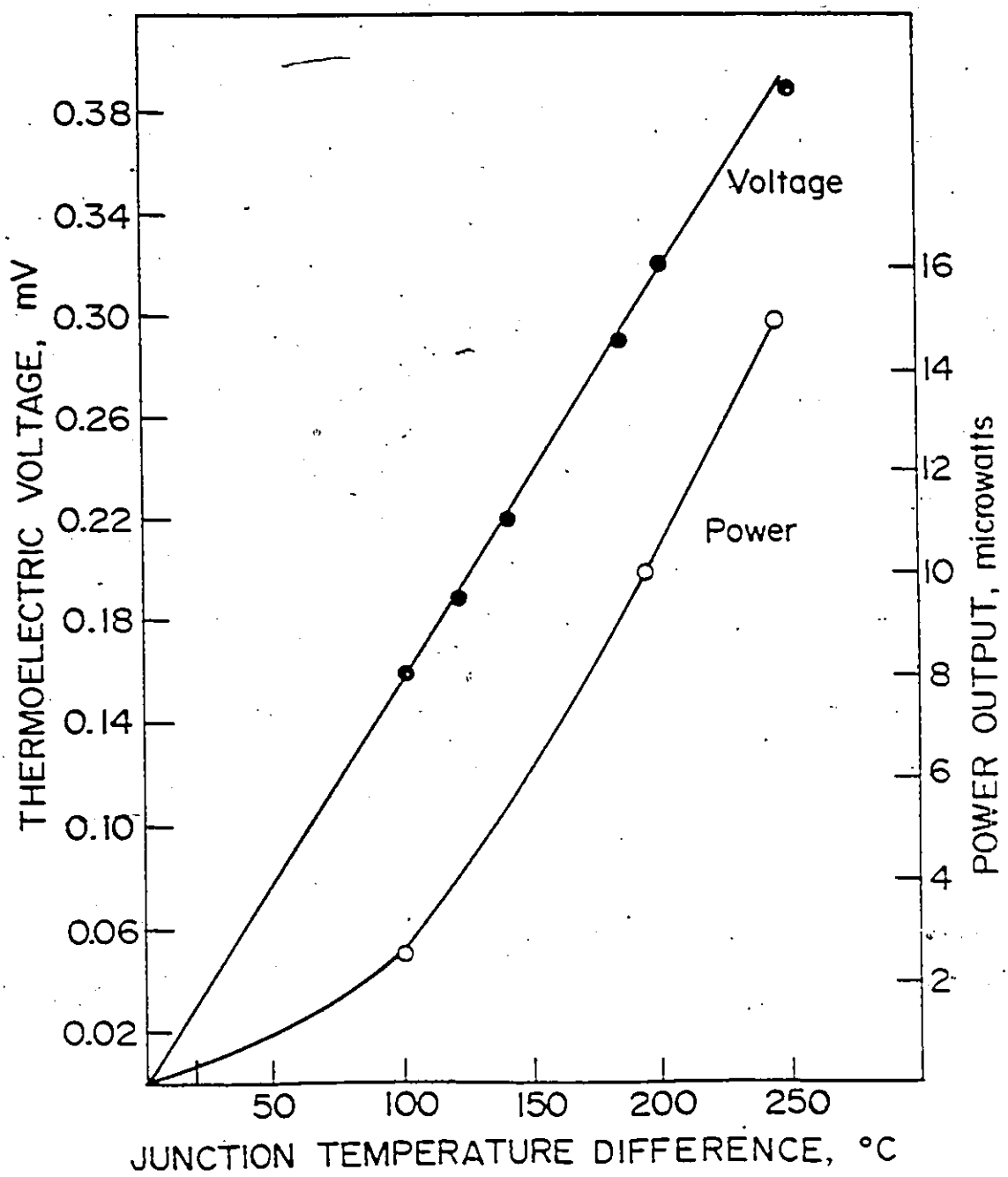

Fig. (3.4) The output voltage and the thermoelectric power delivered into a matched resistive load as a function of temperature difference. (See text for details).

Table (3.3) Maximum values of the figure of merit, Z for bulk Bi-Sb and some other semiconductors

Semiconductor	$Z_{max}(10^{-3}deg^{-1})$	References
Bi-Sb	1.8	[120]
$BiTe_3$	2.0	[120]
$AgSbTe_2$	1.2	[121]
Pb-Te	1.2	[122]
InSb	0.47	[122]
Ge-Si	0.9	[122]

Fig. (3.4) shows that the Seebeck voltage increases linearly with temperature in the range 100 to 260°C, giving a Seebeck coefficient of about 137 μV/deg. The power delivered to the matching load ranges from 2.5 to 16 μW.

The series connection of the p-type and n-type legs does not have to be lateral, as shown in Fig. (3.3), it can be vertical as shown in Fig. (3.5). The vertical configuration has the advantage of reducing the area the thermoelectric module occupies. The basic experimental problem with this configuration is current leakage through the insulators [124].

The heat sources for thermoelectric generators are mainly fossil fuel, or radioactive isotopes. When periodic refuelling is possible and oxygen is available, fossil fuel can be used. Since the energy per unit weight produced by fossil fuel, if the conversion efficiency >2%, is about fifty times that of a chemical battery, the thermoelectric system will be still lighter and less bulky than a system using chemical batteries [125]. If periodic refuelling is not possible, or oxygen is not available, radioactive isotopes can serve as the heat source enabling the generators to operate unattended for extended periods, longer than 15 years in some cases [125].

Table (3.4) gives the required output power for some cybernetic devices, an area where radioisotope thermoelectric generators find an immediate application [2].

It is informative to compare thin film thermoelectrical generators with thin film solar cells. For a Si thin film p-n junction solar cells, it has been reported that [126,127]: $V_{OC} = 0.58$ V and $\eta_c = 9\text{-}12\%$ where V_{OC} is the open circuit voltage, and η_c is the power efficiency. The highest performance parameters are those of p-GaAlAs/p-GaAS/n-GaAs; the reported values are [128]: $V_{OC} = 0.99$ V and $\eta_c = 12.8\%$.

Keeping in mind the data of Fig. (3.4) and Tables (3.1) and (3.2), it can be seen that thin film thermoelectrical generators can compete only marginally with thin film solar cells. They cannot compete with the more sophisticated thin film solar cells. Nevertheless,

thermoelectric generators have unique advantages: illumination, and hence exposure to an external atmosphere, are not required; no electric energy storage equipment is required to ensure a continuous electric energy supply.

Thus, it is concluded that, as far as power generation is concerned, thin film thermoelectrics cannot replace solar cells in the near future. Nevertheless, they have their important role in specialized applications such as in deep space missions, satellites, cardiac pacemakers, etc.

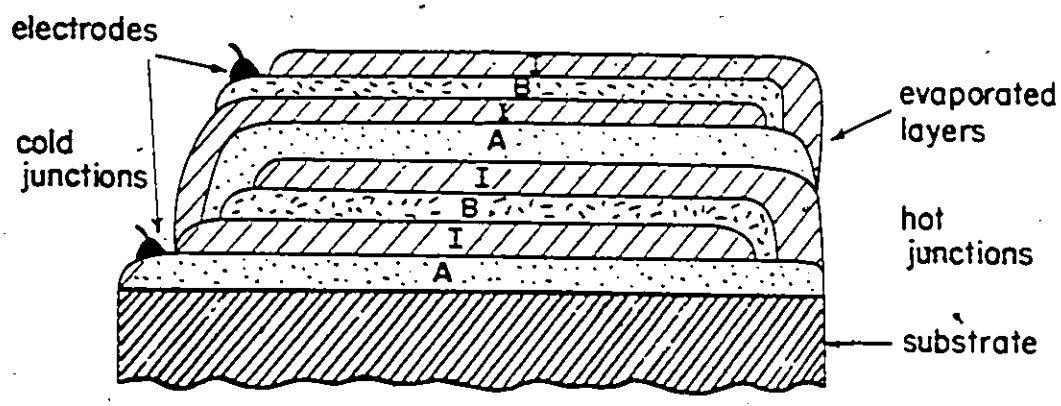

Fig. (3.5) The vertical configuration of a module of a thin film thermoelectric generator; I is an insulator layer, A and B are the junction material (Ref. [126]).

Table (3.4) Output power for some cybernetic devices (from Ref. [2]).

Device	Power
Cardiac pacemaker	3 μW
Carotid sinus nerve (and pump)	300 μW
Sphincter muscle	1.0 mW

CHAPTER IV

EXPERIMENTAL TECHNIQUES AND INSTRUMENTATION

4.1 Introduction

Several experimental techniques and numerous instruments have been used during the course of the experimental investigations reported in this thesis. The techniques can be classified, as far as the present investigation is concerned, into two groups: major and auxiliary techniques; in addition to sample preparation techniques.

(i) Major techniques:

These are ion implantation, Rutherford backscattering spectrometry (RBS), and thermoelectric characterization.

(ii) Auxiliary techniques:

These are transmission electron microscopy (TEM), Auger electron spectroscopy (AES), and various electrical measurements such as Hall effect and resistivity measurements.

In the following sections a short discussion of the physical concepts of the major techniques will be given, followed by the instrumentation. Sample preparation and auxiliary techniques will then be described briefly.

4.2 RBS and ion implantation

When a beam of energetic ions hits a thick solid target, the majority of the ions will come to rest within the target, they are said to be implanted; a small fraction will be backscattered. For RBS analysis [129-131], the sample is bombarded with a beam of light monoenergetic particles, e.g., He^+, and one measures the number of backscattered particles

as a function of their energy. Such a spectrum carries information about the masses of the elements constituting the target and their spatial distribution. The light, MeV ions penetrate the target much deeper than heavy elements implanted at lower energies; they also displace much fewer of the target atoms. This leads to the conclusion that MeV-He ions will not have a significant contribution to the mixing process. Thus, RBS is suitable as an analytical tool for ion-beam-mixing investigations. In the following paragraphs, the basic ideas of RBS analysis will be reviewed.

If the energy of the incident ions is E_0, and that of the backscattered ions is E_1, then from conservation of energy and momentum it follows that [130]:

$$E_1 = k_{M2}\, E_0 \tag{4.1}$$

where,

$$k_{M2} = \left[\frac{M_1 \cos\theta + \sqrt{M_2^2 - M_1^2 \sin^2\theta}}{M_1 + M_2} \right]^2 ,$$

θ is the laboratory scattering angle,

and M_1 and M_2 are the masses of the incident ion and the struck atom respectively.

As the particles penetrate the material, they lose energy along their path. The energy of the backscattered ions from a depth Δx will be less than the energy of the particles scattered from the surface by ΔE, where;

$$\Delta E = \Delta x\, [S_0] = N\, \Delta x [\varepsilon] \tag{4.2}$$

where,

$[S] = dE/dx$ = stopping power,

and $[\varepsilon] = 1/N(dE/dx)$ is the stopping cross section of the target with atomic density N.

Considering that the backscattered ions lose energy both on the way in and out of the target, we can write:

$$[S_0] = \left[\frac{k}{\cos\theta_1} \frac{dE}{dx}\bigg|_{in} + \frac{1}{\cos\theta_2} \frac{dE}{dx}\bigg|_{out} \right] \tag{4.3}$$

where, θ_1 and θ_2 are the angles between the normal to the target and the directions of the incident and backscattered ions, respectively. The total number of detected backscattered particles, A_d, can be written as:

$$A_d = \left(\frac{d\sigma}{d\Omega} \cdot \Delta\Omega\right) \cdot (N \Delta x) \cdot Q \tag{4.4}$$

where,

$d\sigma/d\Omega$ is the differential scattering cross-section,

$\Delta\Omega$ is the solid angle of the detector,

and Q is the number of incident ions.

The differential scattering cross-section for $M_1 << M_2$ is given by:

$$\frac{d\sigma}{d\Omega} = \left(\frac{Z_1 Z_2 e^2}{4E_o}\right)^2 \left[\sin^{-4}\frac{\theta}{2} - 2\left(\frac{M_1}{M_2}\right)^2 + \ldots\right]. \tag{4.5}$$

The number of particles backscattered from the surface (or an interface) is given by:

$$H = \left(\frac{d\sigma}{d\Omega} \cdot \Delta\Omega\right) \cdot Q \cdot \tau N \tag{4.6}$$

where τ is a slab at the interface determined by the resolution of the detecting system.

A major advantage of the RBS technique using light ions is that the cross- sections are accurately predictable and thus no calibration procedures are necessary once the scattering geometry is known. The technique also provides depth information (≤ 1 μm) non-destructively [130].

Fig. (4.1) shows a schematic of an RBS spectrum of a sample composed of three elements with the spatial distribution indicated. The main features of the spectrum are:

i) A signal with a peak at an energy $k_{M2}E_0$. This signal corresponds to backscattering from the atoms of mass M_2 at the surface of the solid.

ii) A signal with an edge at energy $k_{M3}E_0$ corresponding to backscattering from the atoms of mass M_3 at the surface; the width of the signal, ΔE, corresponds to backscattering from the atoms of mass M_3 up to depth Δx.

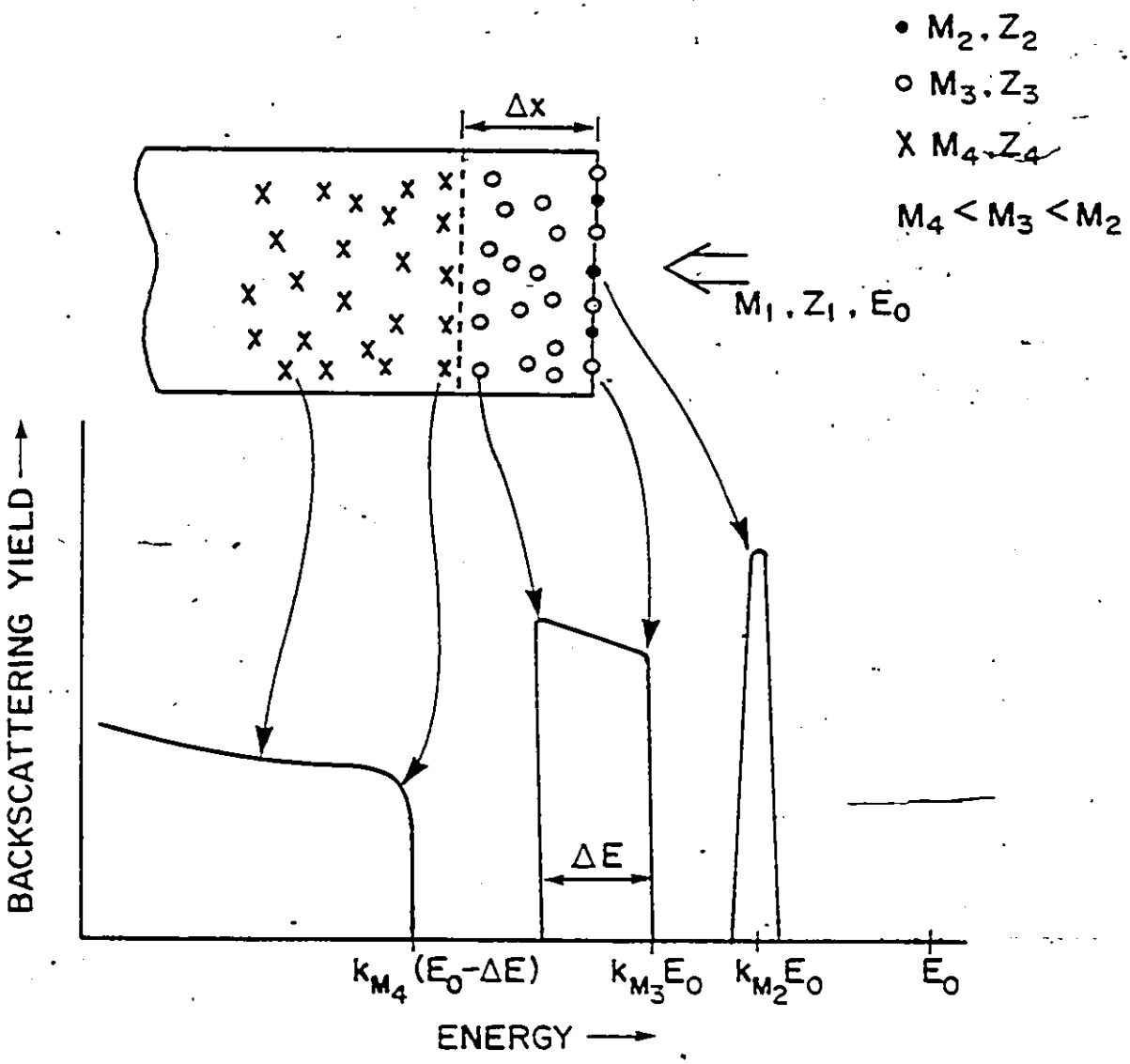

Fig. (4.1) A schematic of an RBS spectrum.

iii) A signal with an edge at energy $k_{M4}(E_0-\Delta E)$ corresponding to backscattering from the atoms of mass M_4 at depth Δx.

The three signals are not overlapping, and hence producing a clear spectrum, because $M_4 < M_3 < M_2$ and because the thickness Δx is small enough so that:

$$(k_{M3} E_0 - \Delta E) - k_{M4}(E_0 - \Delta E) > 0.$$

A block diagram of the system used for RBS analysis and for ion implantation is shown in Fig. (4.2). A 3.5 MV Van de Graaff accelerator (A) is used to obtain a He^+ beam for RBS analysis. The beam is transported to an analysing magnet (E). The transport system (B) provides magnetic steering and magnetic focusing. A 150 KV ion accelerator (C), using a Danfysik 911A universal ion source, is used to obtain the implantation beam, e.g., Ar^+ beam. The beam is transported to the analysing magnet (E). The transport system (D) provides magnetic steering. The focusing is provided by an Einzel lens placed at the exit of the ion source.

The analysing magnet (E) is used to select a monoenergetic beam of the required ion species from either accelerator. The selected beam is then transported to the target (sample) chamber (G). The transport system (F) provides a feedback circuitry to stabilize the energy of the beam. A system of apertures is used for defining the beams. The He^+ beam is defined to 0.7 mm diameter. For implantation, a 2 mm aperture (closest to the magnet) and a 4 mm aperture (closest to the target chamber) are moved up, off the beam axis, such that the 4 mm aperture is higher than the 2 mm aperture. The beam is then steered electrostatically to the target chamber. This arrangement ensures that the ions neutralized between the magnet and the 4 mm aperture will not bombard the target because there is no direct path to the target. The implantation beam is swept horizontally and vertically to ensure the uniformity of the implantation.

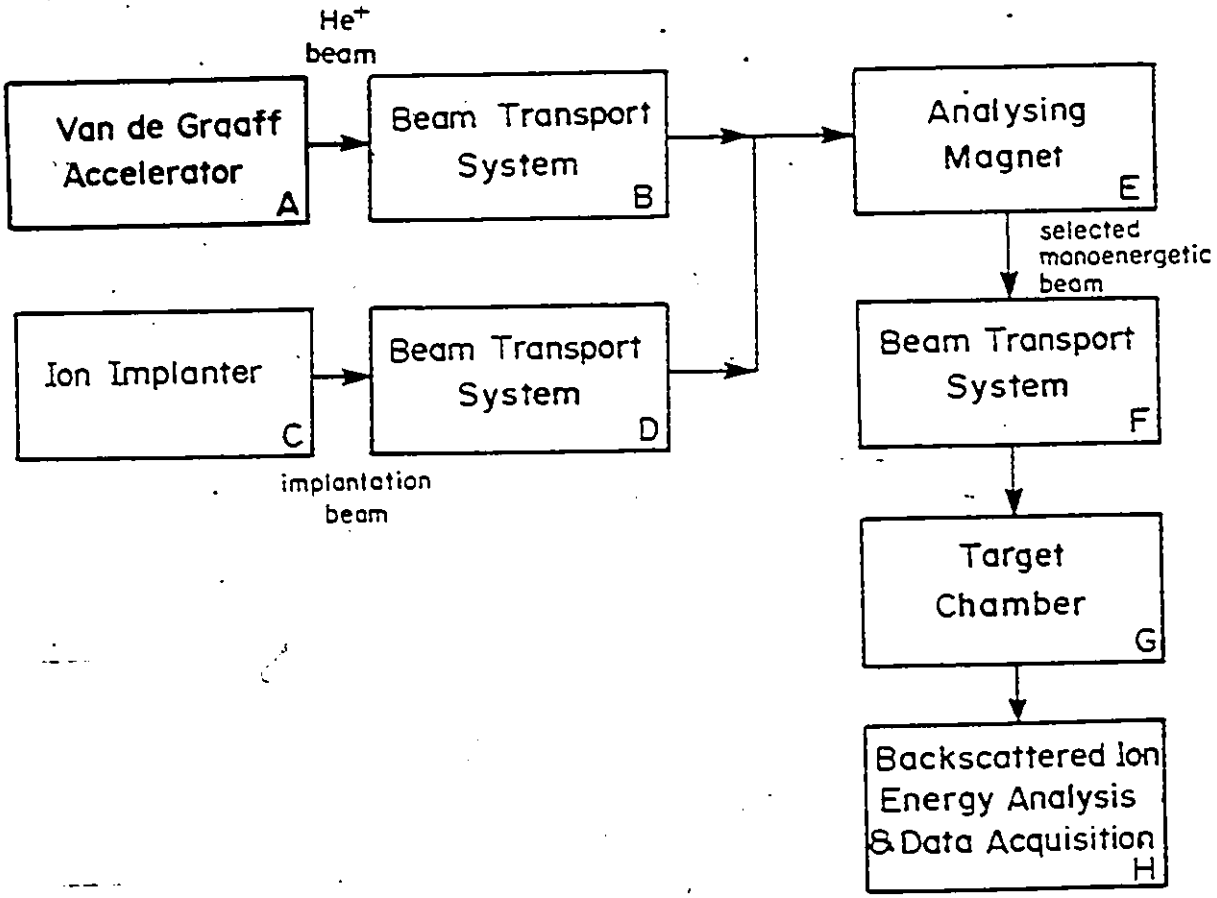

Fig. (4.2) A block diagram of RBS/implantation system.

A schematic of the target chamber is shown in Fig. (4.3). The sample is mounted on a goniometer that has two degress of rotation with respect to the incident beam. The sample can be heated with a heater connected to the copper sample mount. The sample can also be cooled via a cryocooler that can be connected thermally to the sample mount using a flexible copper braid. A radiation shield surrounds the cryocooler in the chamber to minimize the radiative heat loss. The target mount is surrounded by a copper shield that is also attached to the cryocooler. This target-shield arrangement acts as a Faraday cup for beam current measurements. A radiation shield, cooled to liquid nitrogen temperature, surrounds the copper shield. The target mount is thermally isolated using a thin- wall stainless steel tube. A gold (doped with 0.07 Fe)-chromel thermocouple is fixed to the target mount to measure the temperature. A removable Faraday cup is placed at the entrance of the chamber. It is used during the adjustment of beam parameters before letting the beam impinge on the sample.

The ion dose is determined by measuring the integrated charge at the target over the period of ion bombardment. To ensure accurate measurement of current, the target mount and the copper shield are electrically isolated from the cryocooler with a ten-micron Mylar film and from the goniometer with a Teflon washer. Secondary electrons are suppressed by applying –220 V to two copper rings placed at both ends of the shield; they are electrically isolated from it. The base pressure in the system is about 10^{-7} Torr.

The dose-measurement system starts with a current integrator (Ortec model 439); it measures the beam current on either the target or Faraday cup. A timer/scaler (Ortec model 771) controls the data acquisition. Fig. (4.4) is a block diagram showing the data flow system. Energy analysis of the backscattered ions starts with a silicon surface-barrier detector (FWHM ~15 KeV) mounted in the chamber at a scattering angle of 160°. The detector solid angle is 0.0361 str.

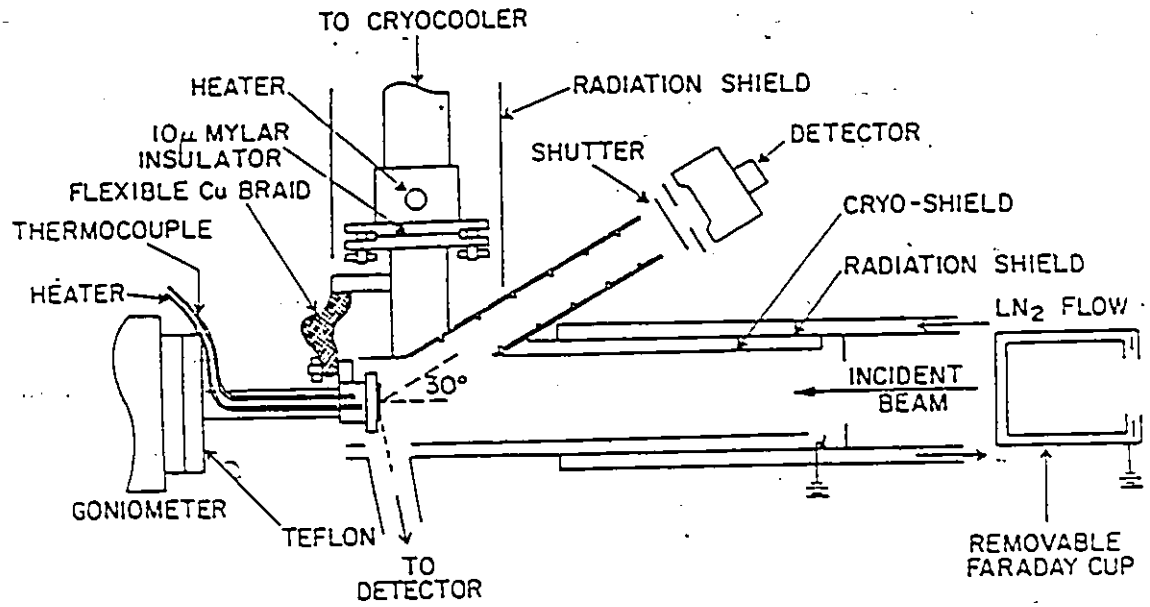

Fig. (4.3) A schematic of the target chamber.

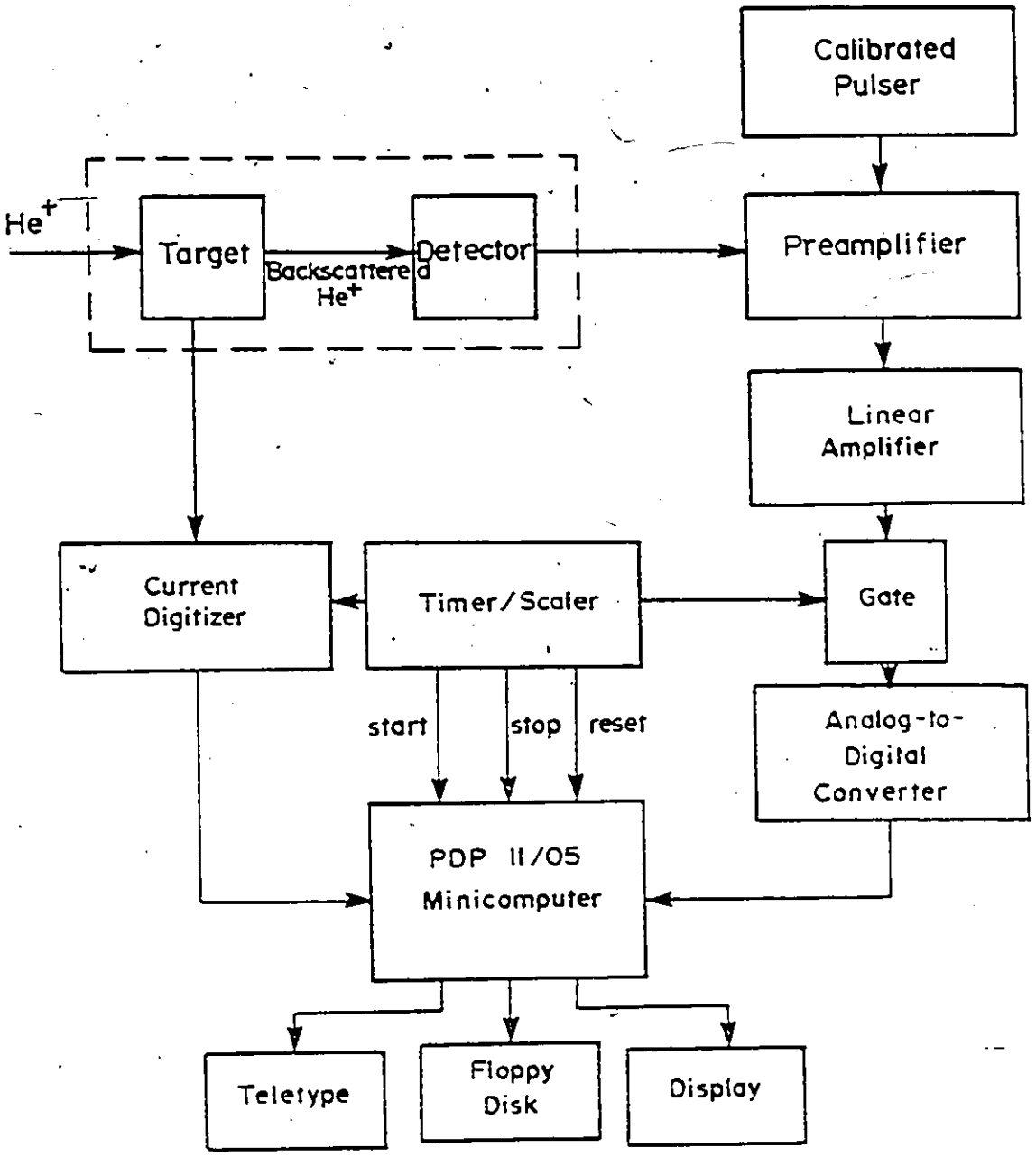

Fig. (4.4) A block diagram of the data acquisition system.

To avoid radiation damage of the detector, it is covered with an externally-controlled shutter during implantation. The backscattered He^+ ion reaching the detector produces a signal (pulse) proportional to its energy. The signal goes directly to a pre-amplifier (Canberra model 1408) then to a linear amplifier (Ortec model 572). The signal is digitized using an analog-to-digital converter (Northern Scientific ADC model 8192). The ADC is connected to a PDP 11/05 minicomputer for pulse height analysis and data acquisition.

4.3 Thermoelectric characterization

4.3.1 Thermoelectric power measurement

The relation between the thermoelectric power, S, the temperature gradient, and the developed voltage, V_s, can be written in either of two equivalent forms:

$$S = \left.\frac{dV_s}{dT}\right|_{T_1} \tag{4.7}$$

or

$$V_s = \int_{T_0}^{T_1} S\,dT . \tag{4.8}$$

This leads to two theoretically equivalent methods for S measurement: the integral and the differential methods [132].

In the integral method, the temperature at one end of the sample is maintained at T_0. The developed voltage, V_s, is then measured as a function of the temperature at the other end of the sample, T_1. The value of S can be obtained by differentiating $V_s(T)$ with respect to T. This can be accomplished graphically by plotting V_s vs. T. An average value of S can be defined if V_s vs. T is linear over the temperature range of interest; otherwise, S will be a function of temperature. The integral method is not practical if a very small sample and very large temperature gradient are to be used.

In the differential method, a "small" temperature gradient, $\Delta T = T_1 - T_0$, is maintained fixed across the sample and the average temperature is varied. The temperature gradient has to be small enough so that S can be assumed constant and large enough so that appreciable voltage can develop.

In both methods, the electrical contact will have an effect on the measured value of the thermoelectric power of the sample. The effect will be significant if the absolute value of the thermoelectric power of the material of the contacts is comparable to that of the sample. In general, if the absolute value (as opposed to relative; the sign is considered) of the thermoelectric power of the sample is S_A and that of the contact is S_B, then the measured value, S_{AB} (A relative to B) is given by [133]:

$$S_{AB} = S_A - S_B \tag{4.9}$$

Since it is the temperature range ~300 to 500 K that is considered in the present investigation, the integral method was used. It was preferred because of its simplicity. The system used for thermoelectric power measurement is shown schematically in Fig. (4.5). Two copper electrodes, pressure contacting the sample, were used to measure V_s. One electrode was maintained at room temperature while the other electrode was heated. The temperature was controlled by controlling the current flowing through the heater using a variable resistor connected in series with the heater. Two thermocouples were fixed to the electrodes to measure the temperature.

4.3.2 Measurement of the figure of merit

To evaluate the figure of merit using Eq. (3.33), one has to measure S, σ, and K. Measurement of K is difficult particularly for a thin film. An alternative method was first suggested by Harman [134] and revived by Trefny [135]. The essential physics of Harman's

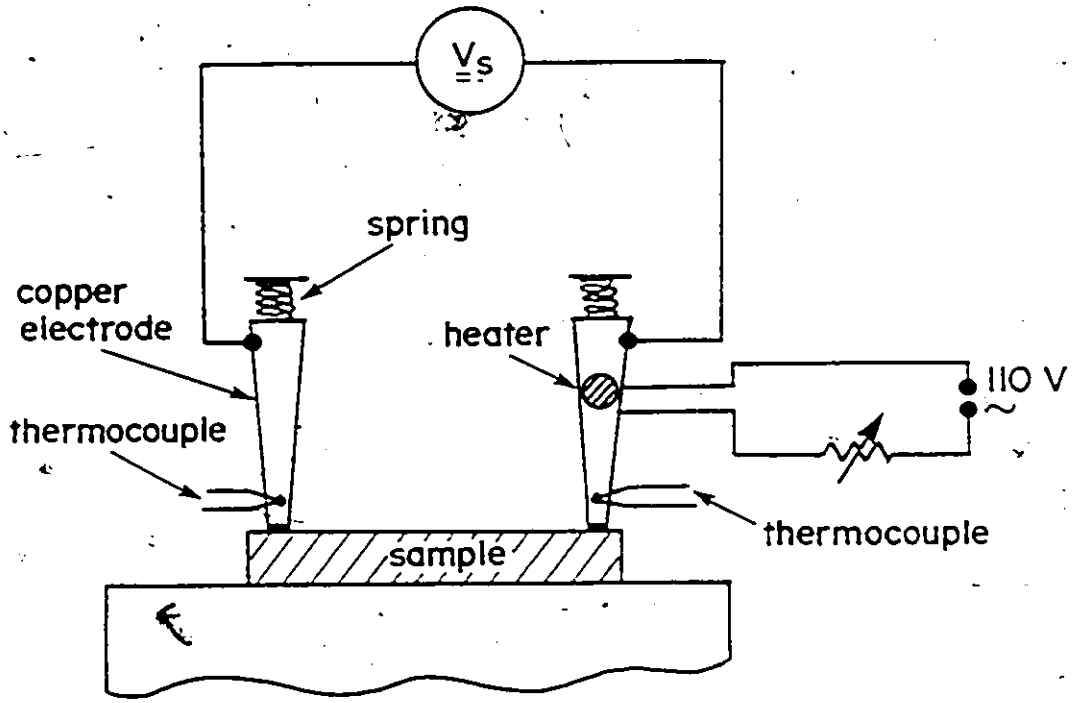

Fig. (4.5) Schematic diagram of the system used for measuring the thermoelectric voltage.

technique is contained in the two basic transport equations: Eq. (3.6) and Eq. (3.7), which will be rewritten here as:

$$\varepsilon = J/\sigma + S\nabla T . \tag{4.10}$$

and

$$J_u = -K\nabla T + STJ . \tag{4.11}$$

Eq. (4.10) expresses that the steady state electric field, ε, may arise in a conducting medium due to a current density, J, and a temperature gradient ∇T. Eq. (4.11) expresses that the heat current density J_u, is due to a temperature gradient and an electric current density.

Under isothermal conditions, Eq. (4.10) can be written as:

$$(\varepsilon / J)_{T=0} = \frac{1}{\sigma} = \rho_{iso} \tag{4.12}$$

Under adiabatic conditions, Eq. (4.11) can be written as:

$$(\varepsilon / J)_{J_u=0} = \rho_{iso}\left[1 + \frac{S^2\sigma T}{K}\right] = \rho_{ad} \tag{4.13}$$

This leads to:

$$\frac{S^2\sigma T}{K} = \left(\rho_{ad}/\rho_{iso} - 1\right) \tag{4.14}$$

or

$$Z.T = \left(\rho_{ad}/\rho_{iso} - 1\right)$$

Practically, an ac resistance measurement yields the isothermal resistance, ρ_{iso}, and a dc resistance measurement yields the adiabatic resistance, ρ_{ad}. Hence

$$Z.T = (\rho_{dc}/\rho_{ac} - 1) \tag{4.15}$$

The major sources of error in this technique relate to the Seebeck coefficient of the leads, the thermal conduction by the support leads and by the substrate, and the radiative heat exchange with the surrounding environment. Nevertheless, if all these factors are kept constant, the technique can be used to compare directly the values of Z for different alloys.

4.4 Sample preparation

Samples were prepared by vacuum deposition of Bi and Sb layers on various substrates at room temperature without breaking the vacuum. The base pressure was typically $\sim 10^{-6}$ Torr. This vacuum is more than adequate because Bi does not readily oxidize, even at temperatures close to its melting point in air [136]. Various substrates were used; samples that were to be electrically or thermoelectrically characterized were deposited onto glass substrates, those which were to be characterized by AES were deposited onto Si substrates, and those to be examined by TEM were deposited on NaCl substrates.

4.5 Auxiliary techniques

A PHI 600 Auger Electron Spectrometer was used for checking the uniformity of the samples in depth and laterally. A TEM (Philips model 300 G) was used to examine the microstructure of some of the samples at various states of mixing. Hall effect measurements were also performed to verify the type of conductivity of some samples before and after mixing.

4.6 Experimental Procedures

Every experimental measurement done in the course of this work was carried out on three or more similar samples to ensure reproducibility. Results of only one set of measurements are reported here unless there was a variation in the mesasured quantity of more than 5% (or when it was important to comment on the variations observed). RBS analysis was done on every sample before and after ion bombardment except for samples prepared for analysis by TEM. RBS, TEM, and AES were done on various spots on the samples to check the lateral uniformity. Repeated thermoelectric and RBS measurements

were carried out on some samples to check the effect of repeated heating on V_s and He^+ bombardment on mixing.

CHAPTER V

RESULTS AND DISCUSSION

5.1 Introduction

In this chapter the experimental results of this work are presented, analysed, and discussed. The following sections are organized such that direct answers to the questions raised in Chapter I can be concluded.

In Section (5.2), the results indicating the ability of forming $Bi_{1-x}Sb_x$ alloys by ion beam mixing are presented. The microstructure of the alloys is also shown. In Section (5.3), the dependence of mixing on the parameters of the mixing beam and on the temperature is revealed leading to the discussion of the possible mixing mechanisms in Bi-Sb system. In Section (5.4), the results of the thermoelectric characterization of the alloys are given. They are discussed in terms of a well-established model put forward to explain the transport properties of bulk $Bi_{1-x}Sb_x$ alloys. A model, based on the concepts discussed in Section (3.2), is proposed to give an insight into the relation between the measured thermoelectric power and the mixing doses.

5.2 Ion beam mixing

The feasibility of producing Bi-Sb alloys by ion beam mixing was investigated by monitoring the effect of ion bombardment on the elemental spatial distribution. The samples were composed of a thin Sb layer sandwiched between two Bi layers. Typical RBS spectra obtained using a 2 MeV $^4He^+$ beam, impinging normally on the sample, are shown in Fig. (5.1). The signals from Sb and Bi are well-separated. The total number of counts in the Sb signal is 3462 $\pm$ 59 for a dose of analysing He^+ of $(1.87 \pm .1) \times 10^{13}$ ions/cm^2. Since the

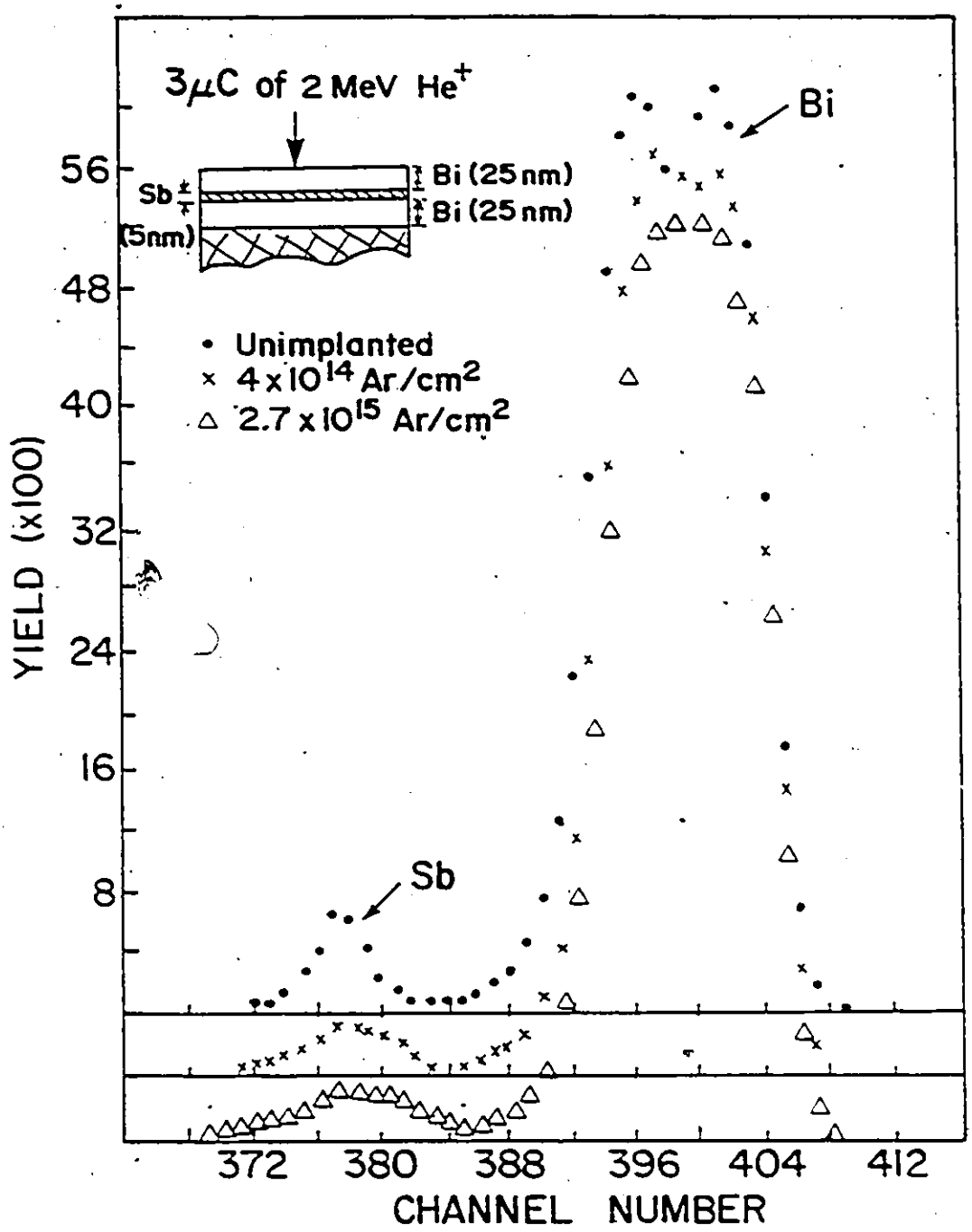

Fig. (5.1) RBS spectra before and after bombardment with 80 KeV Ar^+ (room temperature).

differential scattering cross-section, $d\sigma/d\Omega$, is 3.4×10^{-24} cm^2/str. and the detector solid angle, $d\Omega$, is 3.61×10^{-3} str., then, from Eq. (4.4), the thickness of the Sb layer is 6.3 ± 0.4 nm, assuming a bulk density for the Sb layer of 3.31×10^{22} cm^{-3}. Successive doses of Ar^+ lead to broadening in the Sb signal; the full width at half maximum (FWHM) increased from 4 channels (= 18 KeV) to about 10 channels (= 45 KeV). This represents an increase of about 52.7 nm in the Sb width, i.e. the Sb became distributed over the width of the sample.

For bilayer samples, mixing also occurs but a higher dose of mixing ions is needed for complete mixing. Fig. (5.2) shows RBS spectra obtained using a 2 MeV $^4He^+$ beam impinging normally on a bilayer Bi/Sb sample. The arrow indicates the position where Sb signal should appear if Sb were on the surface of the sample. This was determined by doing an RBS analysis, under the same experimental conditions, of a sample composed of two very thin Bi and Sb films ($\simeq$1.0 nm each). The position of the arrows are the position of the peaks of the Bi and Sb signals thus obtained. Hence, Fig. (5.2) indicates that under Ar^+ bombardment, Sb has reached the surface of the sample. Bilayer samples were not used for any further investigations.

Similar results to those shown in Figs. (5.1) and (5.2) were obtained by doing the RBS analysis on different regions of the sample that are 2 mm above and below the initial region analysed.

The final alloy composition is determined by the relative thicknesses of the deposited Bi and Sb layers. The composition was verified from RBS spectra using Eq. (4.4).

The uniformity of the alloys was examined by AES laterally and in depth. Fig. (5.3) shows an example of depth profiles obtained before and after bombardment with 2.8×10^{15} cm^{-2} of 80 KeV Ar^+ for a sample of the marker type deposited on a Si substrate. Under the influence of ion bombardment, Bi and Sb became approximately uniformly

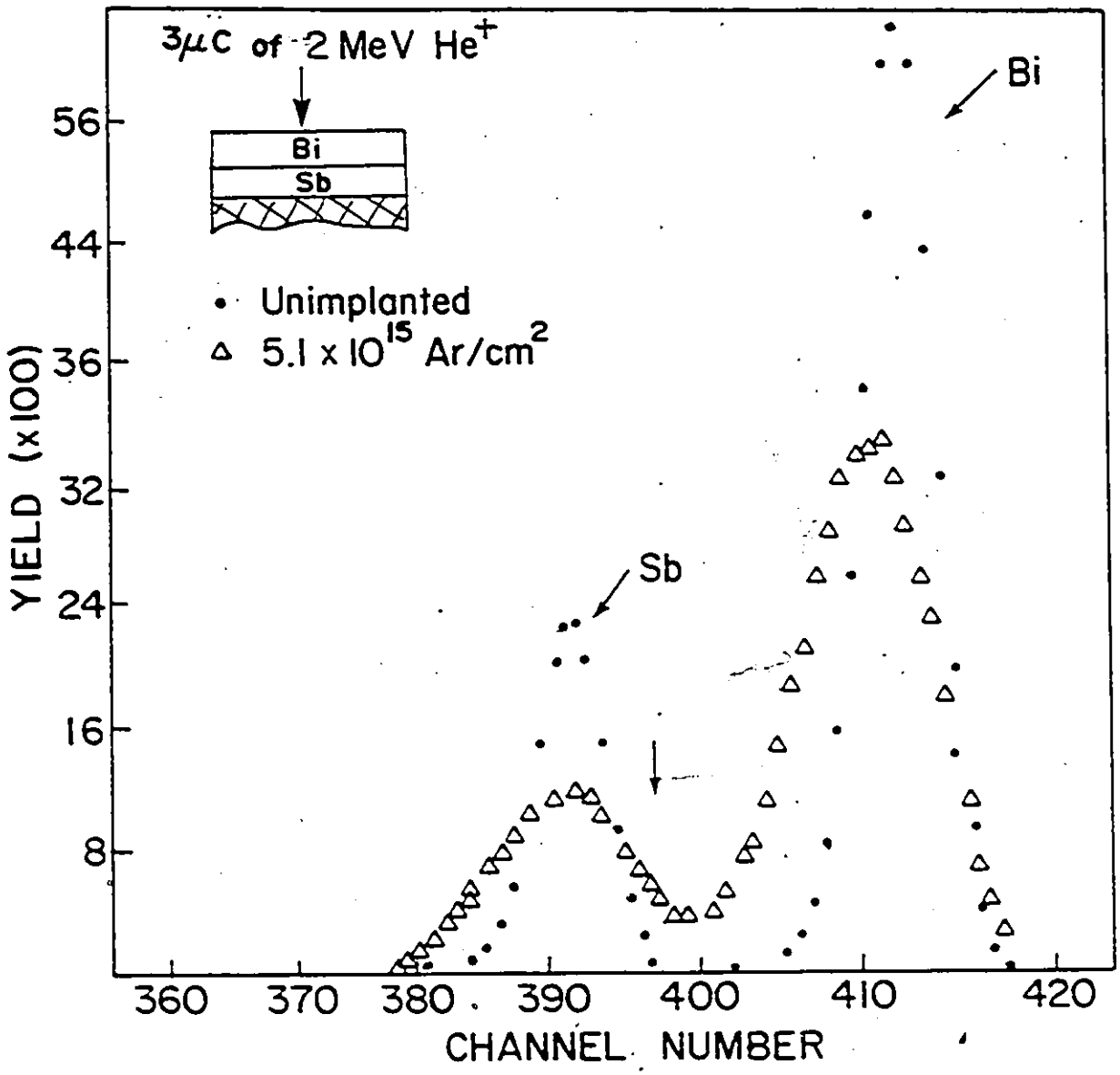

Fig. (5.2) RBS spectra before and after mixing with 80 KeV Ar^+ of Bi/Sb bilayer system (room temperature).

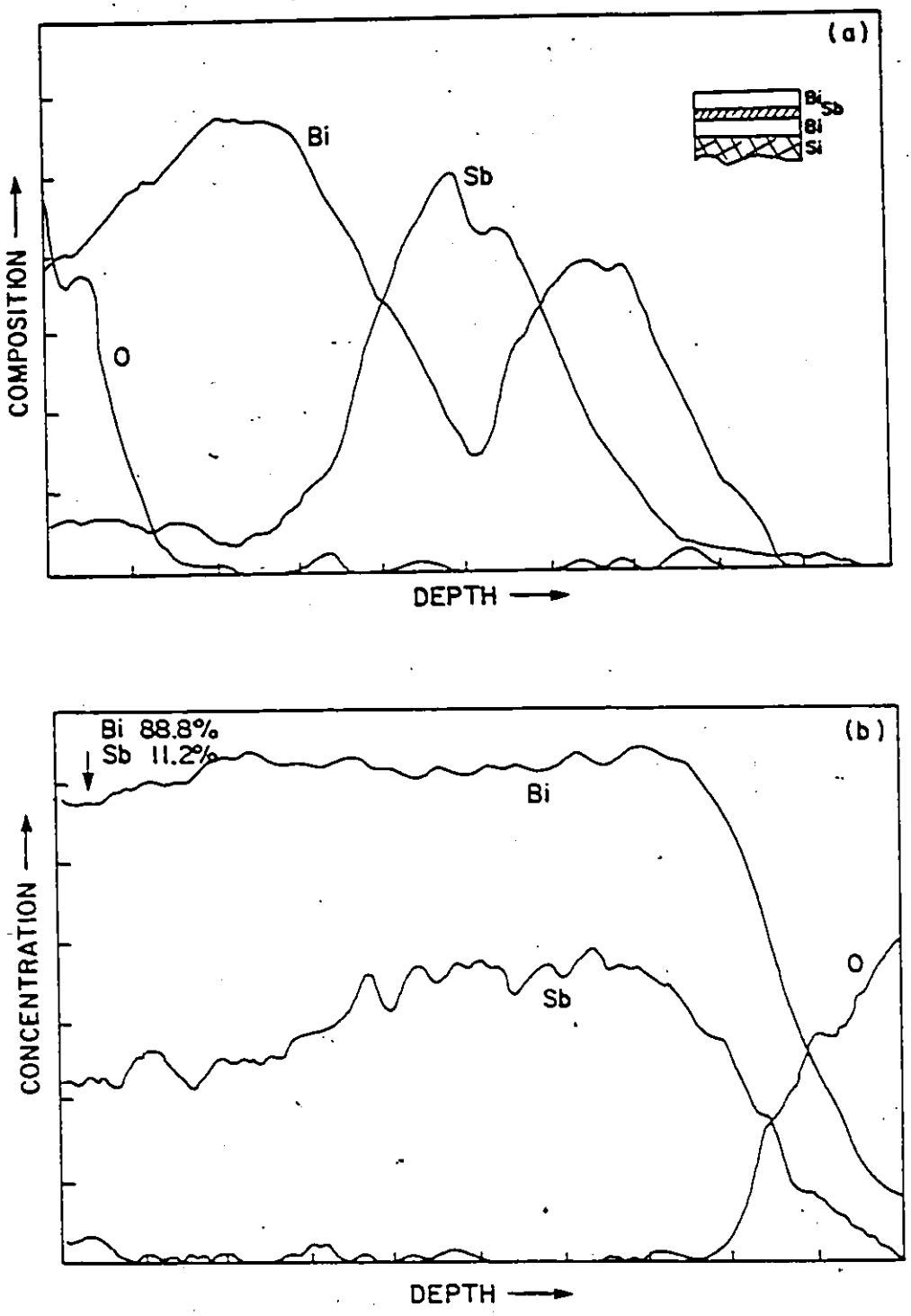

Fig. (5.3) AES depth analysis
a) before mixing
b) after mixing

distributed. Also, the oxygen on the sample surface was removed. The oxygen appearing in Fig. (5.3b) comes from the substrate surface (SiO_2). The apparent variation in Sb concentration near the surface may be due to the preferential sputtering of Sb over that of Bi. The lateral uniformity was examined by performing AES analysis at various points at the surface of the mixed sample; the spots analysed were randomly distributed over the implanted area of the sample. The results are shown in Fig. (5.4). They indicate the existence of lateral uniformity.

Fig. (5.5) shows typical TEM micrographs of Bi/Sb films before and after bombardment with 80 KeV Ar^+. The average grain size increased from ~100 nm to ~140 nm and ~150 nm after bombardment with 1×10^{15} Ar^+/cm^2 and 3×10^{15} Ar^+/cm^2, respectively. This increase may be attributed to the increase in the effective film thickness [86] and to the deposition of elastic energy by the bombarding beam [87].

Compositional analysis by x-ray florescence (using STEM) was carried out on several grains of a sample bombarded with 80 KeV Ar^+ to a dose of $\sim 3 \times 10^{15}\,cm^{-2}$. This was done by comparing the ratio of the counts in the Sb $L_{\alpha 1}$ and Bi $L_{\alpha 2}$ signals after 20 sec. The results indicated that the atomic ratio of Sb to Bi is essentially constant from grain to grain.

The RBS, AES and STEM results have lead to the conclusion that essentially uniform Bi-Sb alloys can be produced conveniently by ion beam mixing.

5.3 Mixing mechanisms

In Section (2.3), the models proposed for ion beam mixing mechanisms were reviewed. The classical models fall into two major categories:

i) Ballistic models which describe the transport resulting from radiation damage.

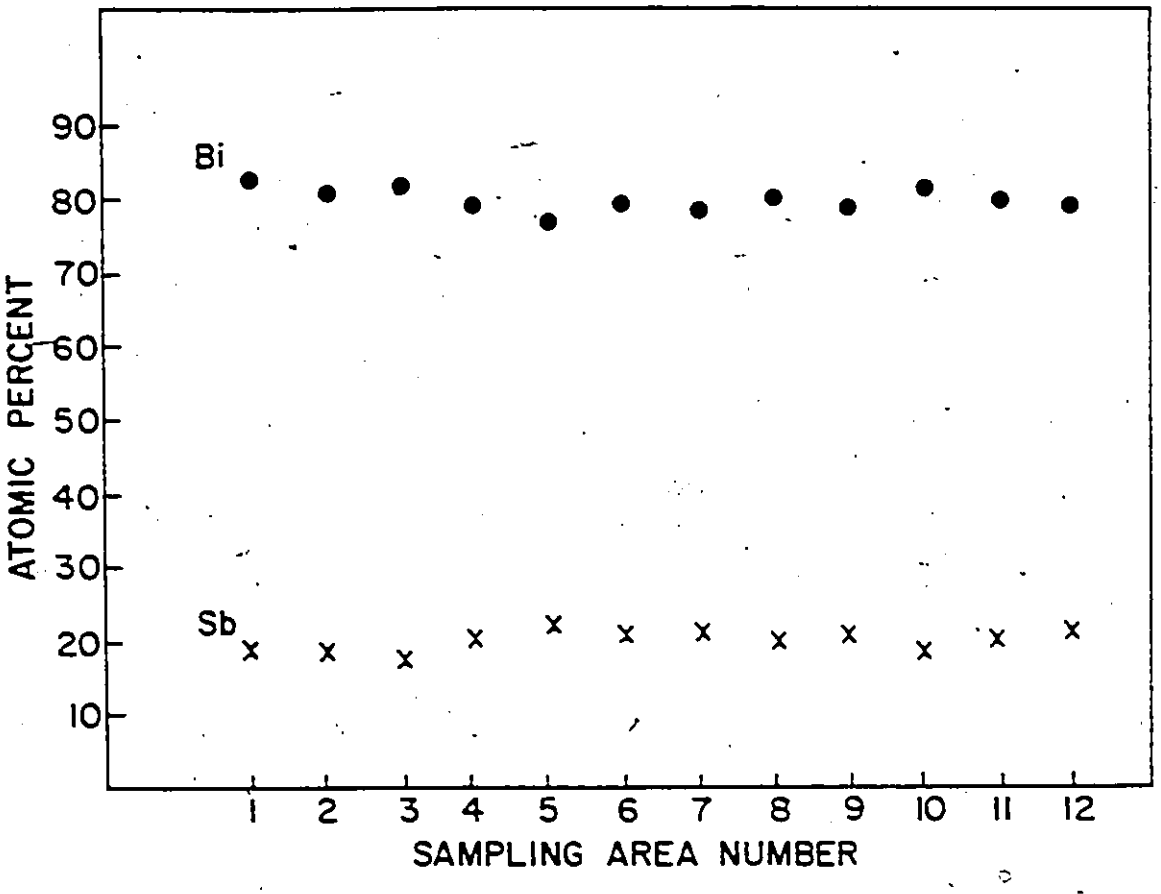

Fig. (5.4) Surface compositional analysis by AES.

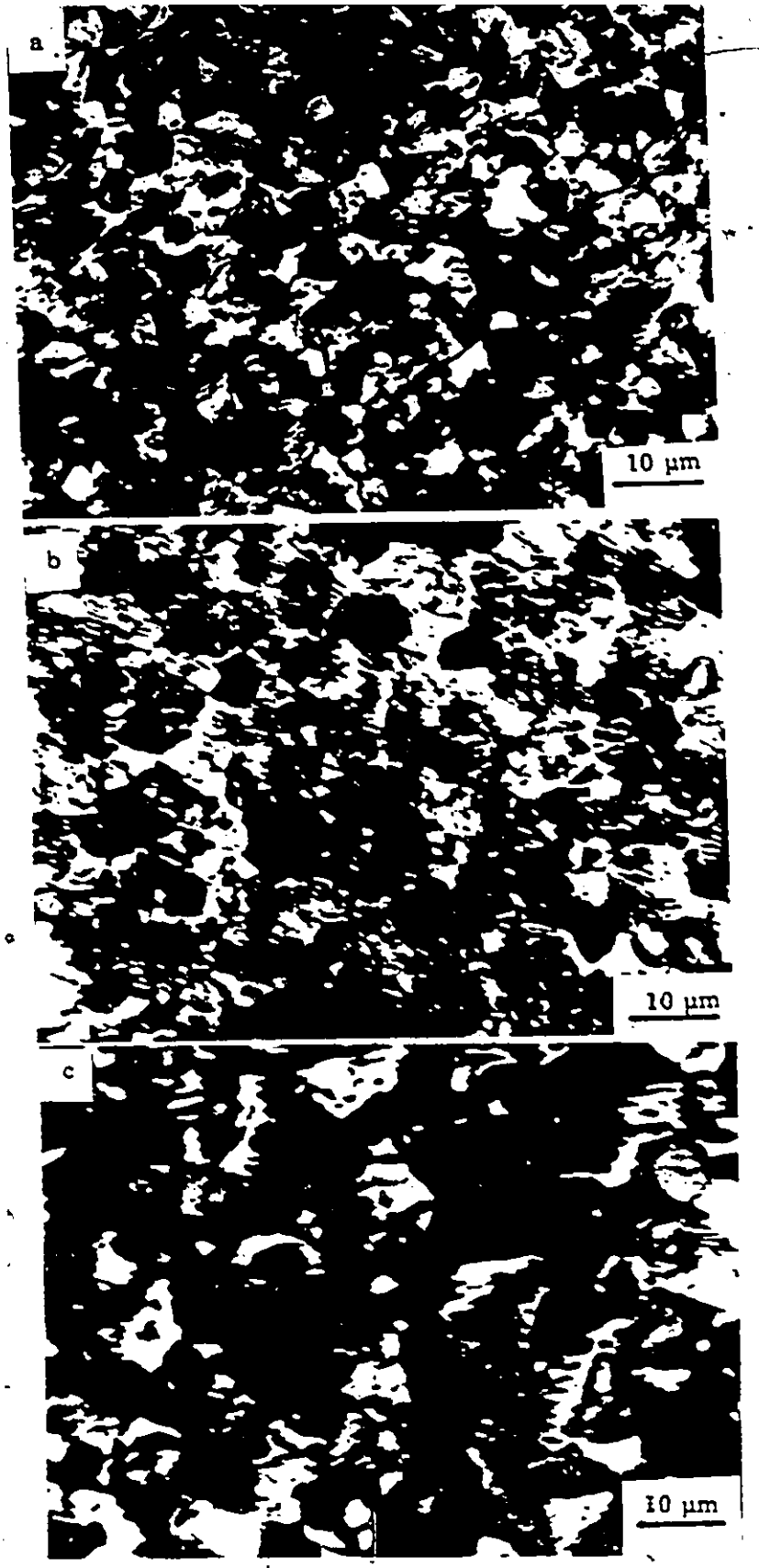

Fig. (5.5) TEM micrographs of Bi/Sb marker system
a) before bombardment
b) after $\sim 1 \times 10^{15}$ cm^{-2} (80 KeV Ar^{+})
c) after $\sim 3 \times 10^{15}$ cm^{-2} (80 KeV Ar^{+})

ii) Models which describe transport resulting from thermal migration of atoms in high concentration of defects.

The models put forward to explain cases where deviation from the classical models occur (e.g. due to chemical effects) were also discussed. The objective of the following sections is to reveal the dominant mixing mechanisms in Bi/Sb system in the light of the models presented in Section (2.3). To achieve this, a measure for mixing is first discussed, then the results of measuring the "mixing" as function of the mixing beam parameters and temperature are discussed.

5.3.1 A measure for mixing

In Section (2.4), it was stated that the increase in the width of a marker is one of the possible measures of mixing. The use of this method for Bi/Sb system in conjunction with RBS analysis will be elaborated on here.

The Sb signal in the RBS spectrum is well distinguished from that of Bi, as shown in Fig. (5.1). There is no ambiguity in determining the FWHM of the Sb signal. This quantity can serve as a measure of mixing as explained in the following.

Assuming a random walk, diffusion-like mixing process, then the solution of the "diffusion" equation obtained for a thin solute layer buried between two semi-infinite solvent layers is valid in the present case, thus we can write [70]:

$$C(x) = \frac{C_{Sb}}{2(\pi Dt)^{1/2}} \exp\left[-\frac{(x-x_o)^2}{4Dt}\right] \qquad (5.1)$$

where, $C(x)$ is the Sb concentration at location x.

C_{Sb} is the initial Sb concentration,

D is the effective diffusion coefficient,

x_o is the position of the initial Sb film,

and t is time.

Neglecting the contribution of the thin Sb layer to the stopping cross-section (~3%), the channel number, n, in an RBS spectrum and the position in the target, x, can be determined using Eq. (4.3). For small amount of mixing, we can write:

$$(x-x_o) = \frac{(n-n_o)\delta E}{[\varepsilon_o]_{Bi} N_{Bi}} \tag{5.2}$$

where, δE is the energy width of the channel

$[\varepsilon_o]_{Bi}$ is the stopping cross-section of Bi $= 2.44\times10^{-13}$ eVcm^2,

and N_{Bi} is the atomic density of Bi $= 2.82\times10^{22}$ cm^{-3}.

Eq. (5.1) can then be written as [70].

$$C(x) = \frac{C_{Sb}}{2\sqrt{\pi Dt}} \exp\left\{-\left[\frac{1}{4Dt}\left(\frac{(n-n_o)\delta E}{[\varepsilon_o]_{Bi} N_{Bi}}\right)^2\right]\right\}. \tag{5.3}$$

This is a Gaussian distribution with standard deviation σ_D given by:

$$\sigma_D^2 = 2Dt\left[\frac{[\varepsilon_o]_{Bi} N_{Bi}}{\delta E}\right]^2. \tag{5.4}$$

The measured standard deviation, σ, from an RBS spectrum can be expressed, in general, as:

$$\sigma^2 = \sigma_D^2 + \sigma_R^2 + \sigma_S^2 + \sigma_T^2 \tag{5.5}$$

where, σ_R is due to the finite resolution of the detection system,

σ_s is due to the straggling produced by the Bi overlayer,

and σ_T is due to the thermal migration.

If we assume that the temperature is low enough that no mixing occurs without ion bombardment, then, $\sigma_T = 0$. If we also assume that both σ_R and σ_s are constant throughout an experiment, then:

$$\sigma_R^2 + \sigma_S^2 = \sigma_o^2 \tag{5.6}$$

where, σ_o is a constant.

Accordingly, the overall standard deviation, σ, measured from an RBS spectra will be:

$$\sigma^2 = 2Dt\left[\frac{[\varepsilon_o]_{Bi}\cdot N_{Bi}}{\delta E}\right] + \sigma_o^2 \qquad (5.7)$$

Rearranging Eq. (5.7), we obtain:

$$D = \frac{\sigma^2 - \sigma_o^2}{2t}\left[\frac{\delta E}{[\varepsilon_o]_{Bi}\cdot N_{Bi}}\right]^2 \qquad (5.8)$$

Equation (5.8) implies that

$$D \propto \Delta^2 \qquad (5.9)$$

and we have:

$$\Delta^2 = (FWHM)^2 - (FWHM)_o^2 \qquad (5.10)$$

$$(FWHM) = 2.34\,\sigma,$$

and $$(FWHM)_o = 2.34\,\sigma_o.$$

From the above analysis, it can be seen that Δ^2 gives information about the effective diffusion coefficient and Δ gives information about the width of the alloy. In the following section, this quantity (Δ or Δ^2) will be used as a measure for mixing.

5.3.2 Dependence of mixing on ion dose and dose rate

The increase in the FWHM of the Sb signal was measured as a function of the irradiation doses of 60 KeV Ar^+ and 110 KeV Kr^+ at room temperature. The doses used were much lower than required for complete mixing to ensure the validity of Eq. (5.7). The results are shown in Fig. (5.6). The error in Δ was taken to be half a channel in the corresponding RBS spectra. A square-root dependence of mixing on the dose of incident ions was observed. This confirms the similarity with thermal annealing processes (see Section (2.4)).

The effect of dose rate, ϕ', on mixing at room temperature was investigated by varying the current density of the mixing beam as follows:

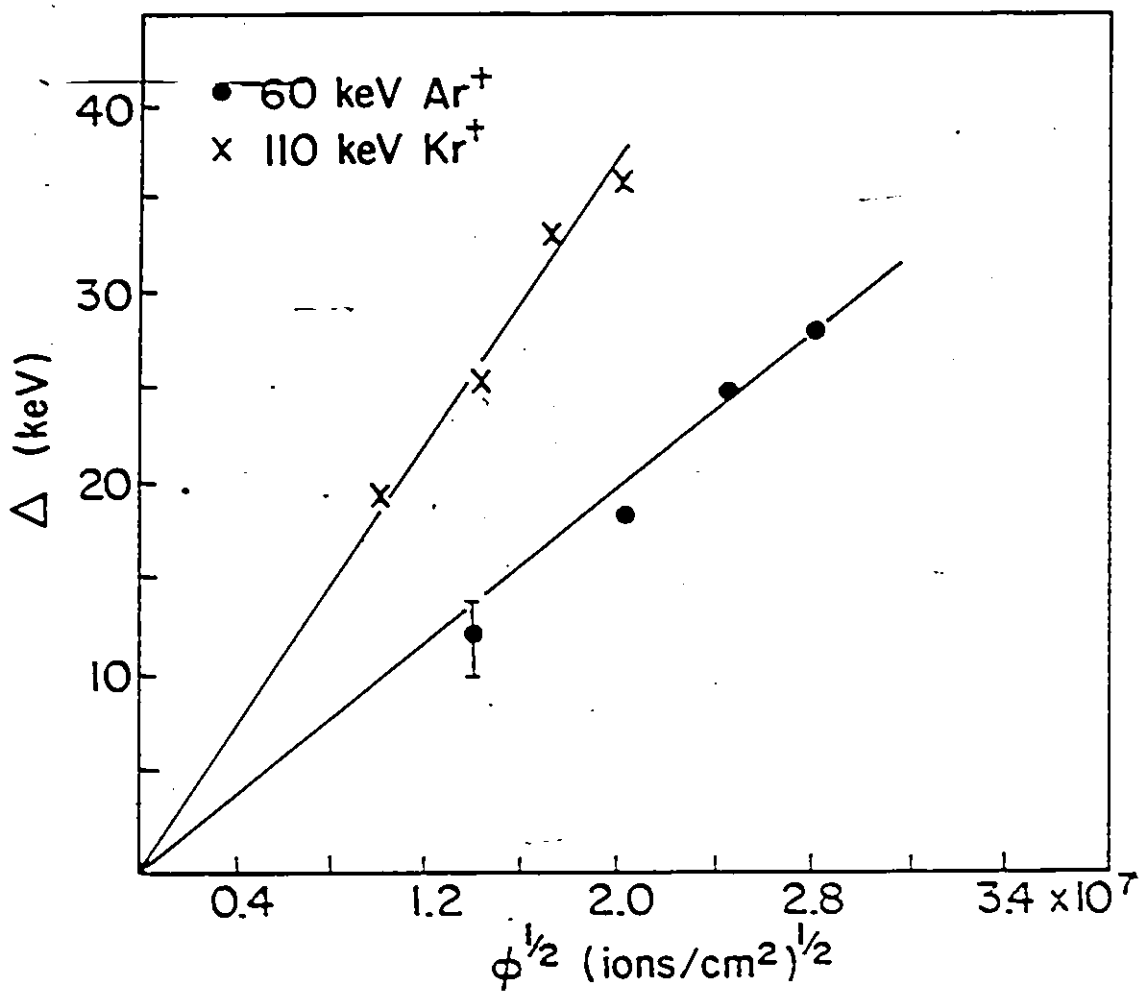

Fig. (5.6) The dependence of the amount of mixing, Δ, on Ar^+ and Kr^+ $(doses)^{\frac{1}{2}}$ for bombardment at room temperature.

i) For 60 KeV Ar^+: 333, 266 and 100 nA/cm^2 beam current densities were used

ii) For 110 KeV Kr^+: 166 and 50 nA/cm^2 beam current densitites were used.

There was no observable effect for varying ϕ' on the rate of mixing.

5.3.3 Dependence of mixing on ion energy and mass

The role of the energy of the incident ions in the mixing process was investigated by measuring the mixing as a function of ion doses for Ar^+ beams with energies: 40, 60, 80, 100 and 120 KeV. The results of mixing with 40, 60 and 80 KeV Ar^+ beams are shown in Fig. (5.7). The results of mixing as a function of beam energy for a dose of 6×10^{14} Ar^+/cm^2 are shown in Fig. (5.8) along with the calculated values of the elastic deposited energy at the interface.

The results indicate that the mixing proceeds faster as the energy increases up to around 60-80 KeV, then it decreases slowly. This behaviour corresponds with the variation of the elastic deposited energy at the interface, as shown in Fig. (5.8). Thus one may conclude that the higher the elastic deposited energy at the interface, the more efficient the mixing will be, i.e., the same ion dose produces more mixing.

The role of the mass of the incident ions in the mixing process was investigated by measuring the mixing at 40 K, as a function of ion doses using 110 KeV Kr^+, 60 KeV Ar^+, and 40 KeV Ne^+ beams. The energies were selected such that the maximum elastic energy will be deposited close to the Bi/Sb interfaces. The calculated values of the elastic energy, mean range, and damage range for Kr^+, Ar^+, and Ne^+ are given in Table (5.1).

The results are shown in Fig. (5.9) and Fig. (5.10). They indicate a square-root dependence of Δ on ϕ, implying a diffusion-like process as before. The square of the slope of

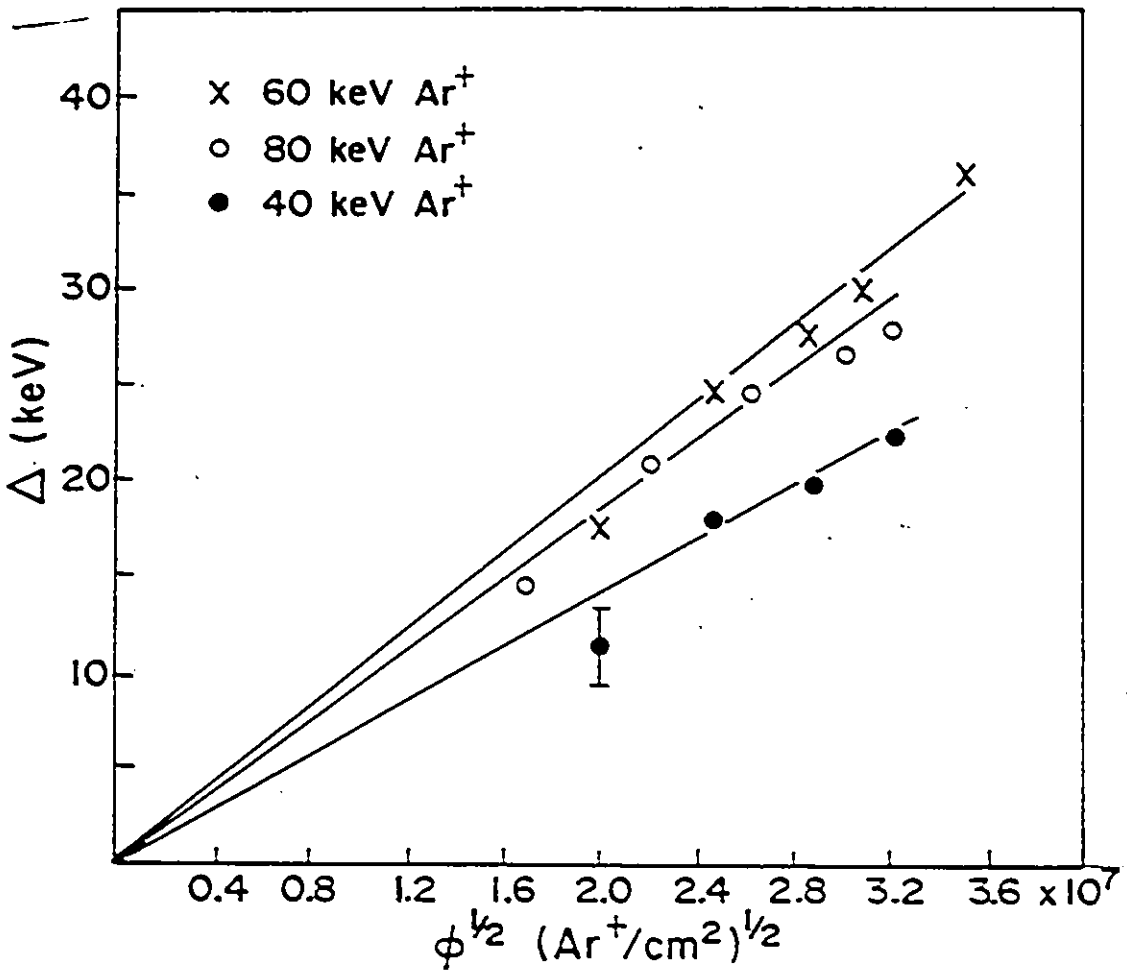

Fig. (5.7) The amount of mixing, Δ, as a function of (dose)$^{\frac{1}{2}}$ for various energies of Ar^+ bombardment at room temperature.

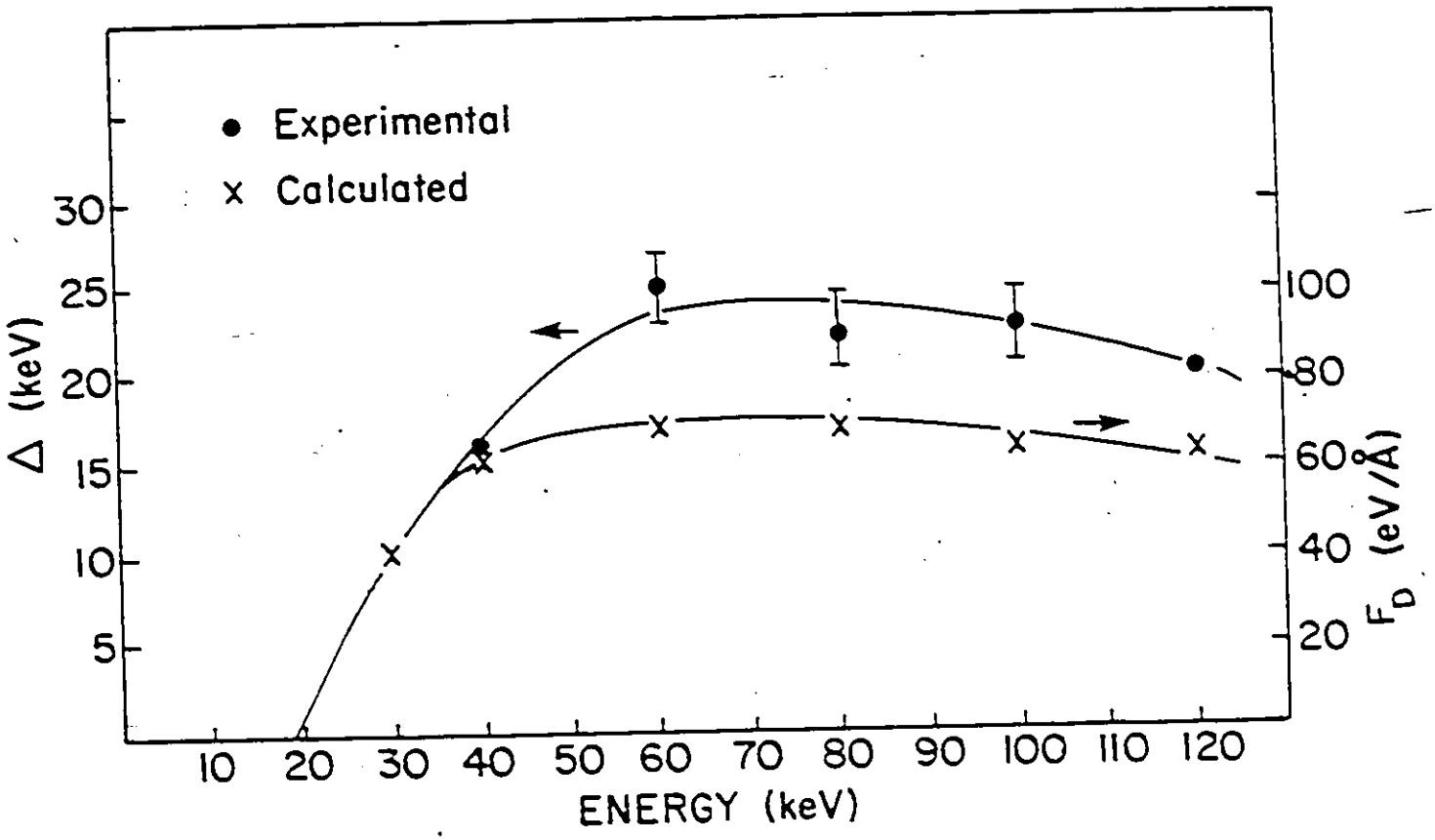

Fig. (5.8) Comparison of the calculated deposited energy (F_D) at the interface and the amount of mixing (Δ) for a dose of 6×10^{14} Ar^+/cm^2 as a function of Ar^+ energy.

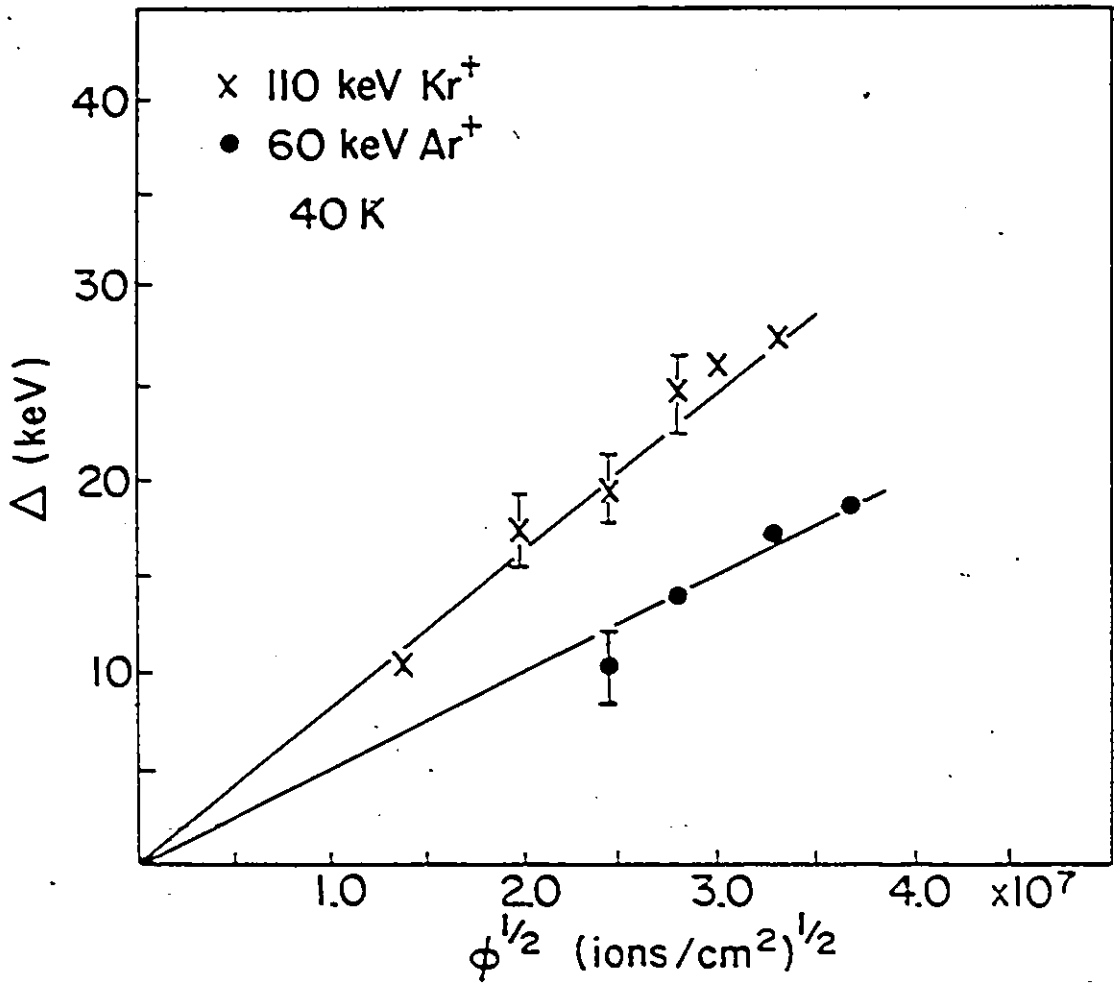

Fig. (5.9) Amount of mixing, Δ, as a function of $\phi^{\frac{1}{2}}$ for Ar^+ and Kr^+ bombardment at 40K.

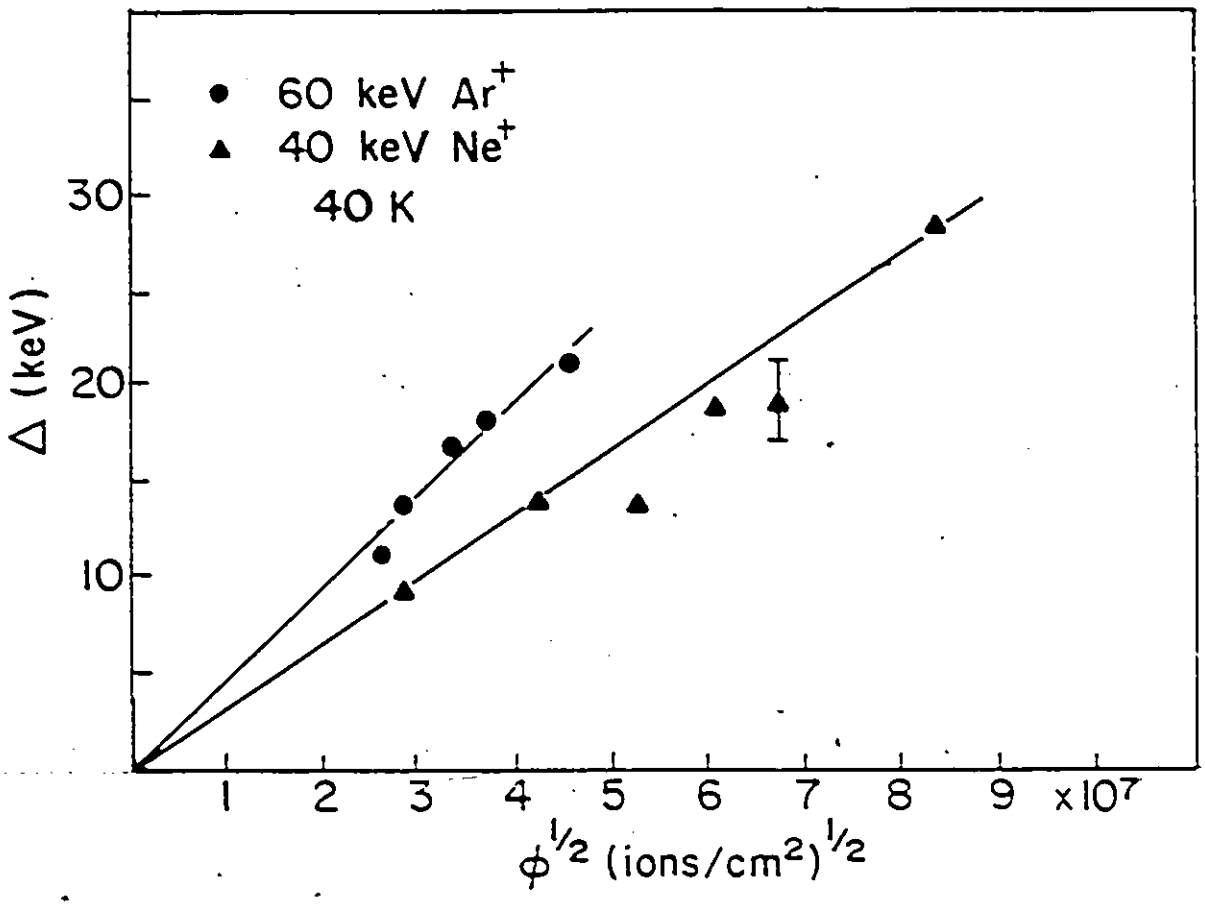

Fig. (5.10) Amount of mixing, Δ, as a function of $\phi^{\frac{1}{2}}$ for Ar^+ and Ne^+ bombardment at 40K.

Table (5.1) Calculated ranges and elastic deposited energies for Kr^+, Ar^+, and Ne^+ in Bi.

Ion	Energy,E (KeV)	Elastic deposited energy, E.v(E) (KeV)	Projected range, R_p(nm)	Damage range, R_D (nm)
Kr	110.0	73.7	34.9	28.8
Ar	40.0	24.0	25.0	21.3
	60.0	35.0	35.4	28.9
	70.0	40.88	40.4	33.9
	80.0	45.92	45.1	37.8
	100.0	55.60	55.1	45.7
Ne	40.0	19.20	39.7	34.1

each line is proportional to the effective diffusion coefficient. Since at low temperature cascade mixing prevails (see Section (5.34)), then, according to Eq. (2.23), the ratio of the square of the slopes should be close to the ratio of the elastic deposited energy. By considering the ratio of the square of the slopes, rather than calculating diffusion coefficients from Eq. (2.23), the uncertainty in the values of some of the cascade model parameters is avoided.

From Table (5.1), the ratio of the elastic deposited energy, E.v(E), for 110 KeV Kr^+, 60 KeV Ar^+, and 40 KeV Ne^+ are: 3.8:1.8:1.0, while from Fig. (5.9) and Fig. (5.10), the ratio of the square of the corresponding slopes are: 5.2:2.0:1.0. The values of $(dE/dx)_n$ at the Bi/Sb interface for 110 KeV Kr^+, 60 KeV Ar^+, and 40 KeV Ne^+ were calculated to be 159 eV/A°, 68 eV/A°, and 29 eV/A°, respectively, giving a ratio of 5.5:2.3:1. These comparisons indicate that the mixing increases with the mass of the mixing ions mainly because of the increase in the elastic deposited energy at the interface.

5.3.4 Dependence of mixing on temperature

The results of measuring Δ, the increase in the FWHM of Sb signal, as a function of temperature for a dose of 4×10^{14} Ar^+/cm^2 are shown in Fig. (5.11). Samples similar to those used for the present measurements were heated up to 100°C (for ~ 300 sec.) and the FWHM of the Sb signal was measured before and after the heating; no increase was observed. Hence, σ_T, in Eq. (5.5), was equated to zero.

The results shown in Fig. (5.11) indicate that mixing is independent of temperature up to about 266 K, then a strong enhancement in the mixing appears as the temperature increases. This trend agrees with what was observed in the majority of the systems investigated up till now (see Section 2.4.1)).

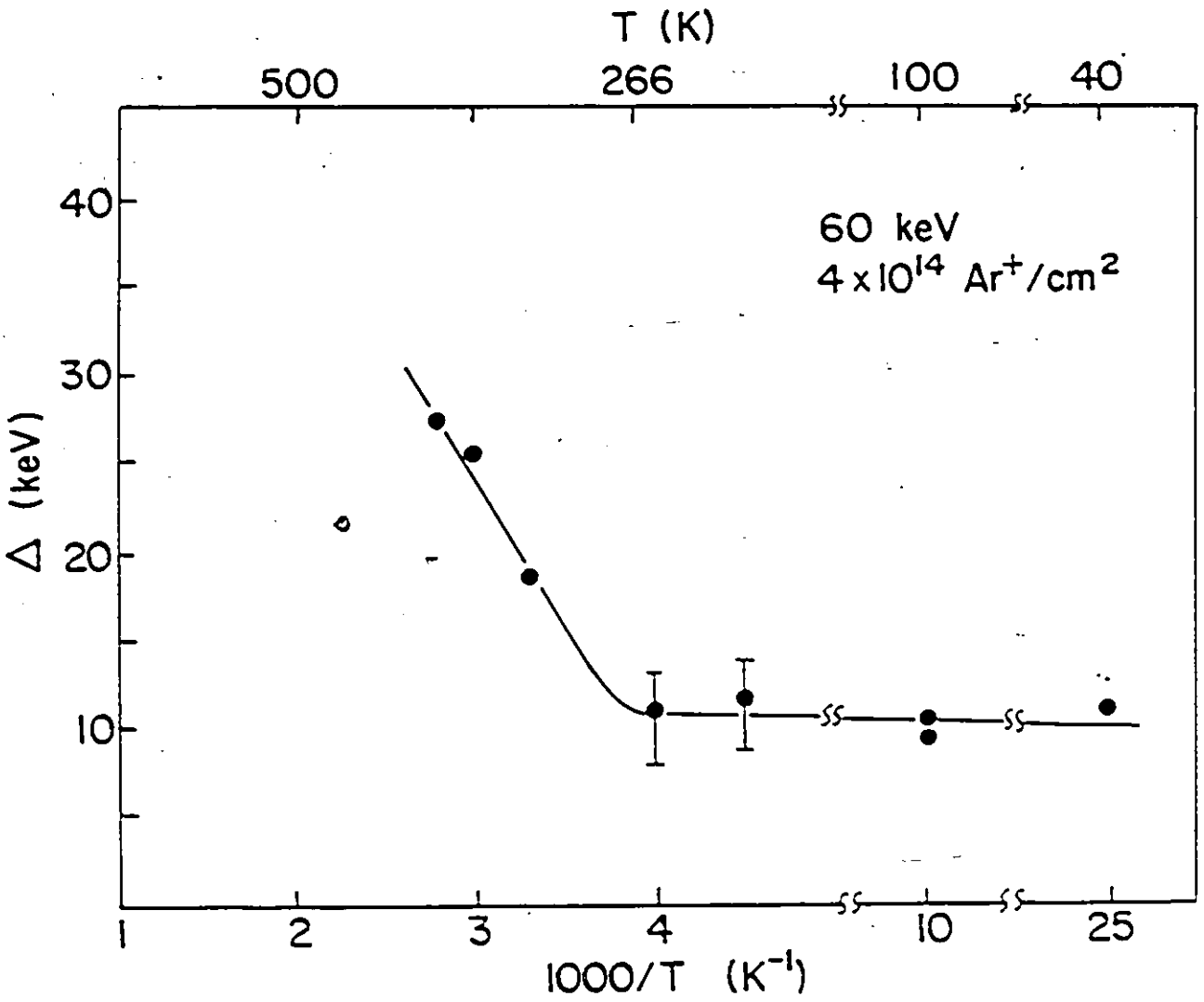

Fig. (5.11) Variation of the amount of mixing vs. temperature for 4×10^{14} cm^{-2} of 60 Kev Ar^{+}.

The implications of these findings are that the cascade mixing dominates at temperatures below about 266 K, while radiation enhanced diffusion dominates at higher temperatures. The identification of the mixing mechanism as cascade is based on the observation that the mixing is independent of temperature below 266 K and down to 40 K within the experimental uncertainties.

Diffusion Coefficients

i) $\underline{T > T_c}$

Eq. (5.8) was used to calculate the effective diffusion coefficient. The information needed for the calculations are listed in Table (5.2). The results of the calculations are given in Table (5.3). In these calculations ϕ' was taken to be 1.66×10^{12} cm^{-2} sec.$^{-1}$.

To obtain the activation energy, E_A, ln(D) was plotted vs. 1000/T as shown in Fig. (5.12), assuming the validity of the relation:

$$D = D_o \exp\left(-\frac{E_A}{K_B T}\right) \qquad (5.11)$$

This leads to: slope $= E_A/K_B T$, hence $E_A \simeq 0.15 \pm 0.02$ eV.

For thermal annealing (without irradiation) the activation energy is 0.66 eV [136]. The reported values of D_o range from 10^{-9} cm^2/sec [137] to 3×10^{-14} cm^2/sec [138]. Thus, the thermal diffusion coefficient is much lower than the effective diffusion coefficient under irradiation.

The value of vacancy migration energy in Bi was evaluated [137] to be 0.3 eV, i.e., E_A is about half the vacancy migration energy. This may suggest that vacancy annihilation occurs principally by direct recombination (see Eq. (2.3)).

Table (5.2) Measured values of the increased Sb width for $4\times10^{14}\,cm^{-2}$ of 60 KeV Ar^+ at various temperatures.

Temperature (K)	300	333	353
$\sigma^2-\sigma^2_o(KeV)^2$	63.9	122.2	142.2

Table (5.3) Calculated values of diffusion coefficient and the corresponding temperatures.

Temperature (K)	300	333	353
D ($10^{-15}\,cm^2/sec$)	2.80	5.37	6.25

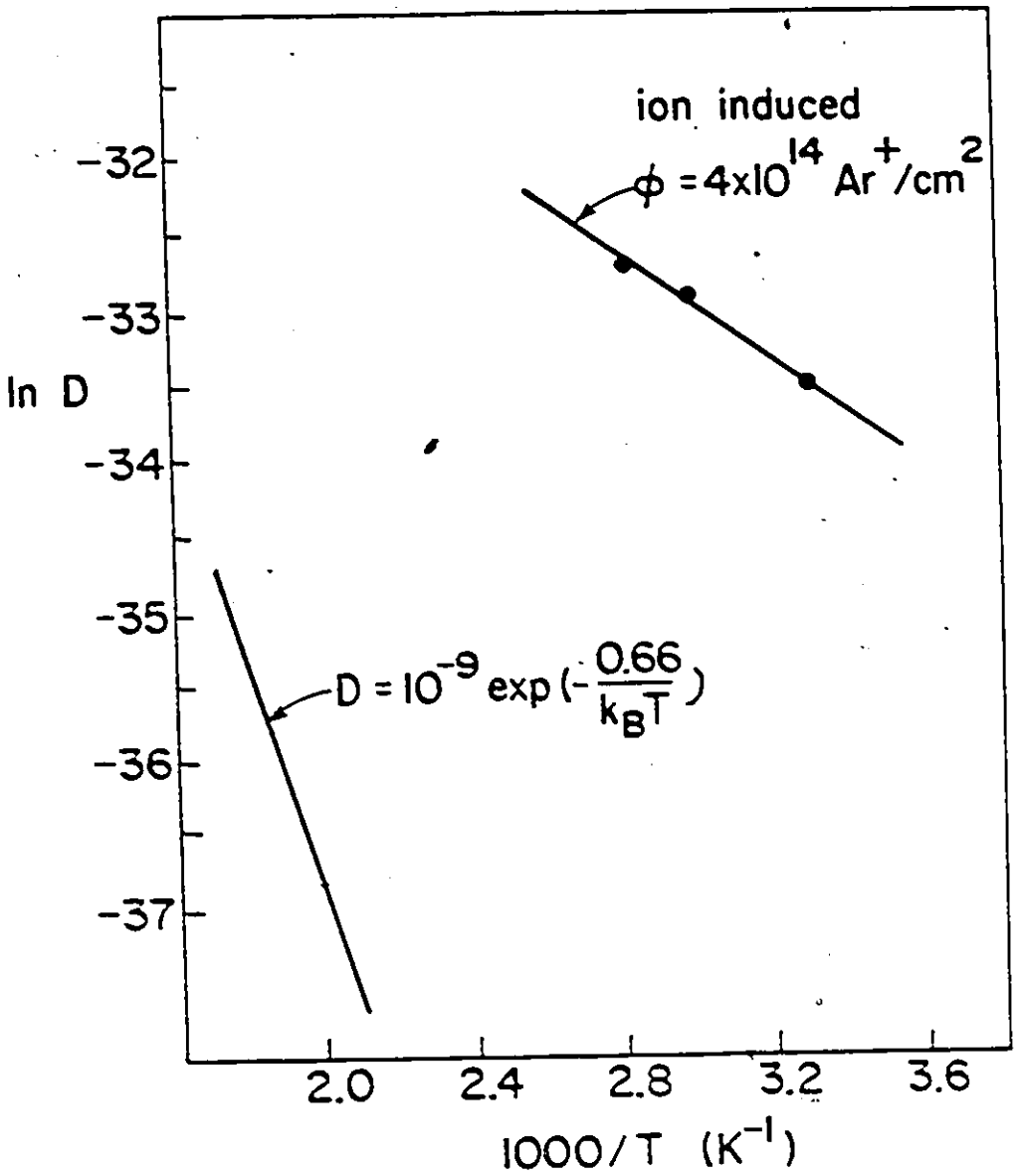

Fig. (5.12) Temperature dependence of diffusion coefficients.

ii) $T < T_c$

At temperatures lower than ~266 K, $(\sigma^2 - \sigma_0^2)$ is constant and is ~18.8 $(KeV)^2$. This leads to a value of the effective diffusion coefficient of about 8.3×10^{-16} cm^2/sec. This value is much lower than that calculated for the cases where $T > T_c$ given in Table (5.3).

5.4 The thermoelectric characteristics

5.4.1 The thermoelectric voltage vs. temperature

The thermoelectric voltage (Seebeck voltage), V_s, was measured as a function of temperature, T, for $Bi_{1-x}Sb_x$ (where x varies from 0 to ~0.45) prepared by ion beam-mixing. The results for three alloys with x = 0.13, 0.23 and 0.48 are shown in Fig. (5.13). In the temperature range 300-500 K, V_s varies linearly with T. Thus, in this range, the thermoelectric power (Seebeck coefficient), S, can be obtained from dV_s/dT (see Eq. (3.1)).

5.4.2 The thermoelectric power vs. alloy composition

The measured variation of the thermoelectric power, S, with the antimony concentration in the mixed alloys is shown in Fig. (5.14) along with values reported for Bi-Sb alloys prepared for other techniques [135]. The reults reported by Favannec et al. [140] for the dependence of S on the thickness of Bi films, shown in Fig. (5.15), were used to correct for the difference in the thickness between samples used in this work (~ 50 nm) and the samples used in the previous study (~ 1 μm) i.e. the results of Ref. [135] were multiplied by 0.9.

Fig. (5.14) shows that the trend of the variation of S with the antimony concentration is similar for ion beam-mixed alloys and those reported in Ref. [135] but with better reproductibility. The maximum, in both cases, occurs around a concentration of 12-13% Sb. This behaviour can be explained, with reference to Fig. (5.16), as follows. Pure Bi is a semimetal that has three conduction band minima located at L-points of the Brillouin zone.

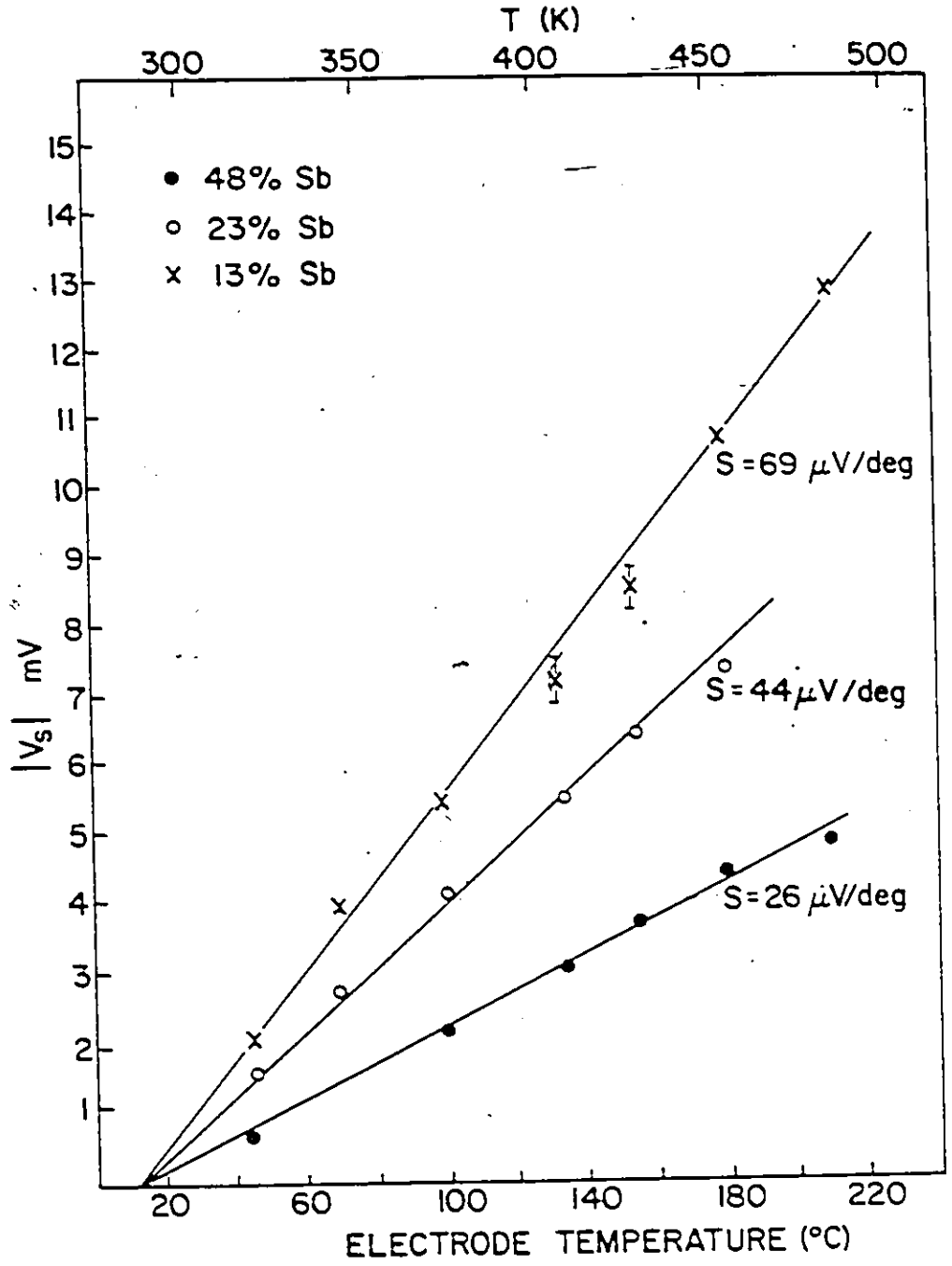

Fig. (5.13) Seebeck voltage versus temperature for three alloys with different Sb concentrations.

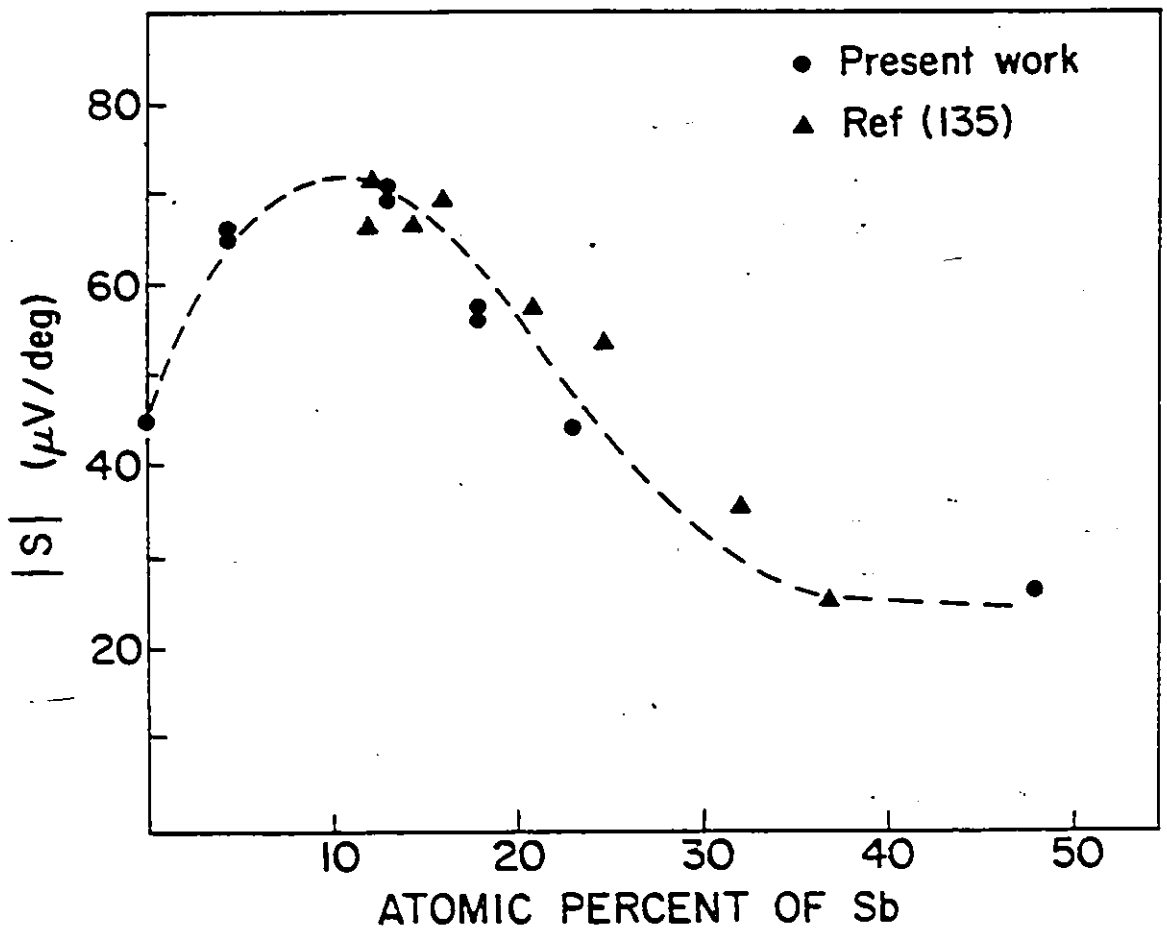

Fig. (5.14) Variation of the corrected thermoelectric power with Sb concentration in Bi-Sb thin film alloys at room temperature.

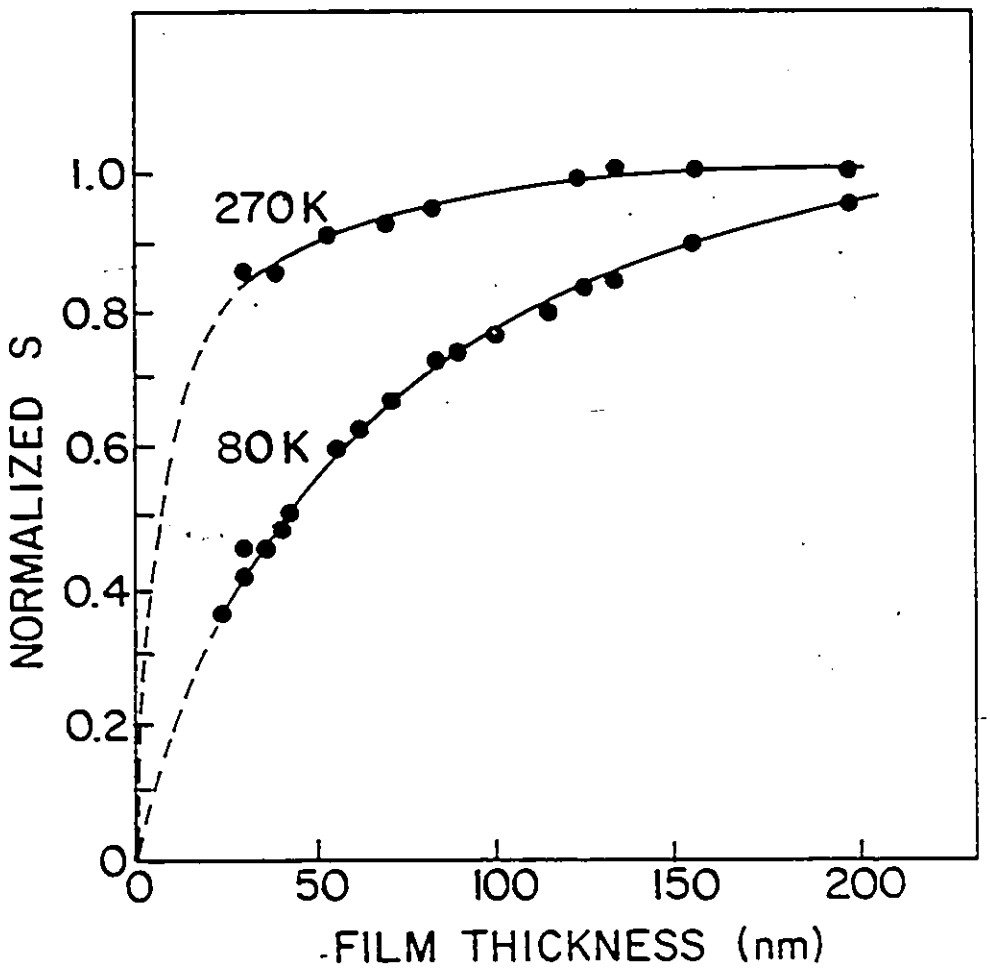

Fig. (5.15) Dependence of the thermoelectric power on the thickness of a Bi film (Adapted from Ref. [140]).

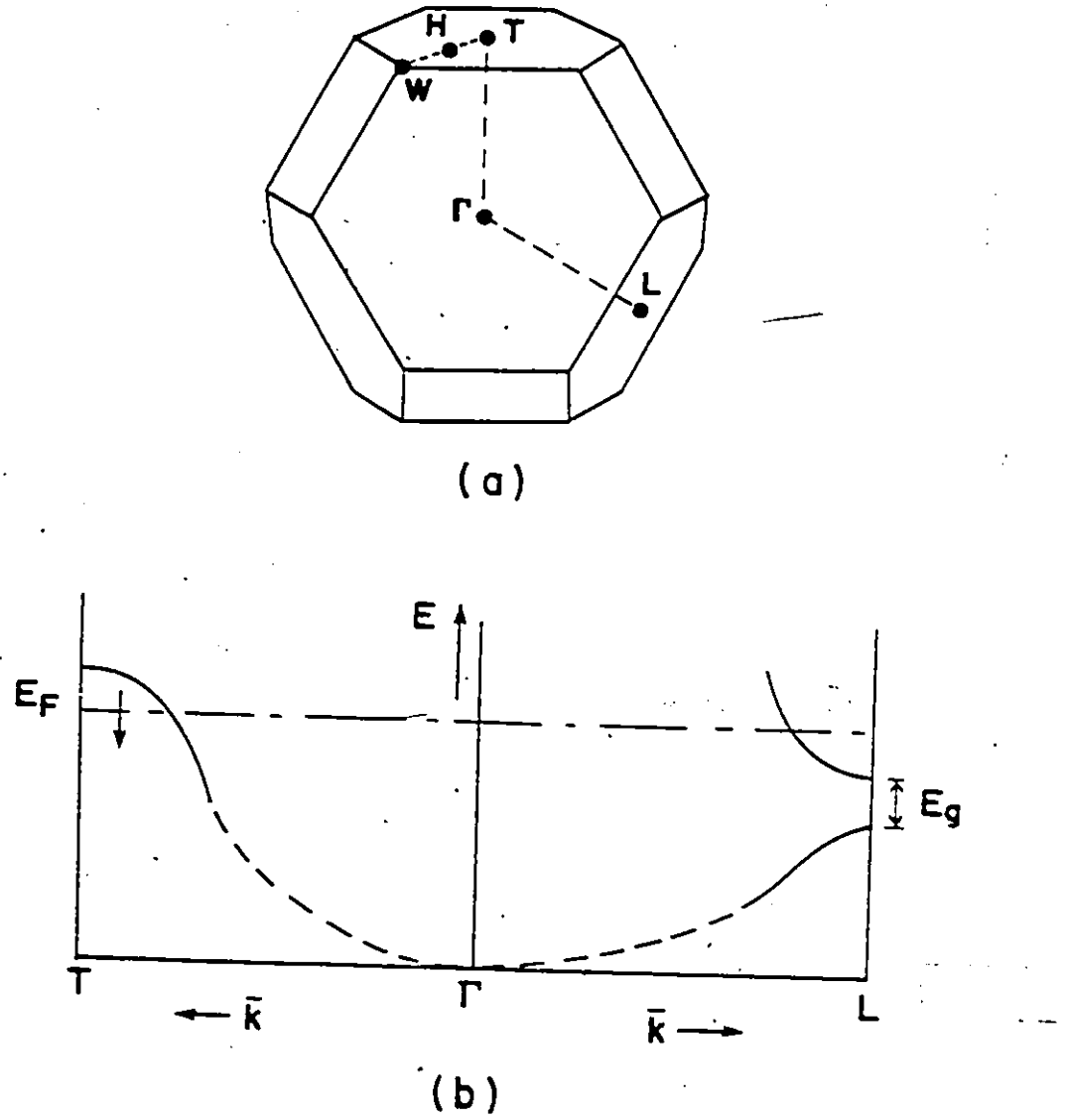

Fig. (5.16) a) Brillouin zone for Bi
b) Schematic of the dispersion relation for Bi near Fermi-energy (from Ref. [141]).

Table (5.4) Dependence of the characteristics of bulk $Bi_{1-x}Sb_x$ on the antimony concentration, x.

x	Phase	Reference
$0 \leq x \leq 0.04$	Semimetal	[142]
$x \simeq 0.04$	Gapless	[143]
$0.07 \leq x \leq 0.22$	Semiconductor	[142, 144]
$0.23 \leq x \leq 0.56$	Semimetal	[145]
$0.75 \leq x \leq 1$	Semimetal	[146]

Table (5.5) Reported values of the maximum energy gap, $E_{g_{max}}$, occurring in Bi-Sb alloys.

$E_{g_{max}}$(meV)	Alloy type	Reference
14.0	Bulk	[147]
24.0	Bulk	[142]
30.0	Bulk	[145]
50.3	Thin Film	[148]

They substantially overlap a single valence band maximum located at T-points. There are also three valence band minima at L-points with a direct energy gap between these bands. As antimony is added to bismuth, the direct gap remains approximately constant; however, the T-point valence band intially moves downwards leading to a gapless phase followed by transition to a semiconductor phase. Further increase in the antimony concentration results in a transition back to the semimetallic phase. Table (5.4) shows the dependence of the phase of the $Bi_{1-x}Sb_x$ alloy on the value of x.

Although there is a general agreement in the literature on the $Bi_{1-x}Sb_x$ model as presented here, nevertheless, there is a disagreement on the magnitude of the energy gaps produced by Sb addition to Bi (and hence on E_F). The values reported by different workers are given in Table (5.5). The values reported of Eg in Ref. [147] and Ref. [148] were evaluated from resistivity vs. temperature measurements, a technique which may not be accurately applied for measuring a narrow energy gap. The values reported in Ref. [142] and Ref. [145] were evaluated from de Haass van Alphen effect measurements, a technique which can be used only for single crystals.

Based on the model discussed above, Eq. (3.35) was used to estimate the variation in the thermoelectric power, S, as a function of the reduced Fermi energy, η, in the range from -2 to $+2$, using the tabulated values of the Fermi integral, $F_r(\eta)$ [92]. The results are shown in Fig. (5.17). They indicate that: as the overlap decreases, the thermoelectric power, S, increases. The measured and calculated values of S are of the same order of magnitude. This represents a good agreement between the theory and the experiment considering the simplicity of Eq. (3.35).

Table (5.6) Comparison of ZT for pure Bi and $Bi_{.87}$ $Sb_{.13}$ thin films.

Thin film	Current (A) (DC or RMS)	ZT
Bi	9.6×10^{-7}	0.068
$Bi_{.87}Sb_{.13}$	6.4×10^{-7}	0.10

Table (5.7) The output power and the Seebeck Voltage for a $Bi_{.87}$ $Sb_{.13}$ alloy.

Temperature Difference	Seebeck Voltage (mV)	Output Power (10^{-9}W)
15	2.1	1.3
50	4.0	4.6
80	5.5	8.3
115	7.3	19.2
135	8.5	21
160	10.5	32
190	13.0	52

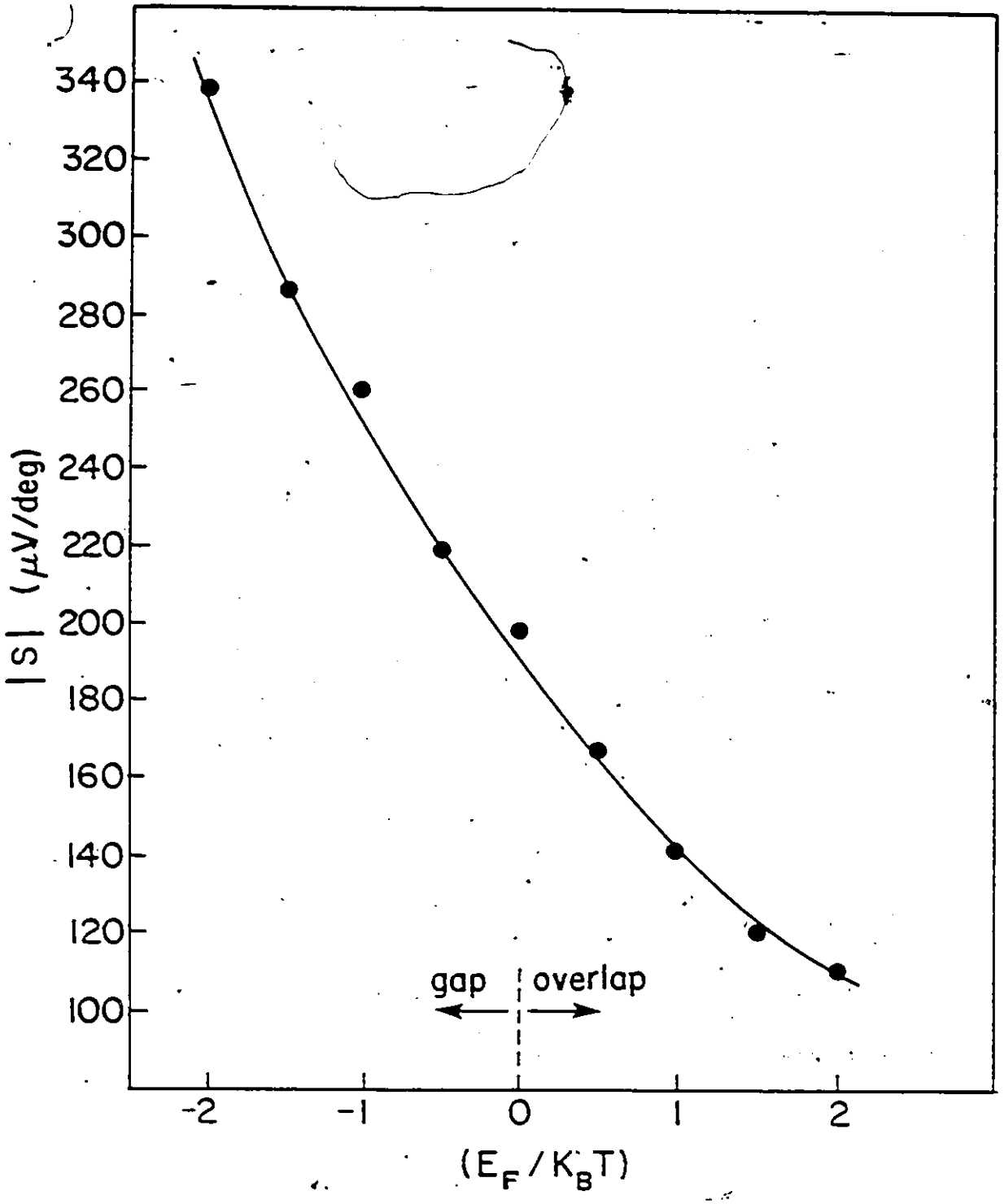

Fig. (5.17) The calculated dependence of the thermoelectric power on the reduced Fermi energy.

5.4.3 Annealing

The possibility of variation of the thermoelectric power due to annealing by repeated heat cycles was investigated by performing repeated measurement cycles. A measurement cycle means raising the temperature, in steps, of one electrode up to about 200°C, then cooling it down to room temperature. The results are shown in Fig (5.18). No appreciable variation in the thermoelectric power was observed for up to 10 measurement cycles.

5.4.4 Type of conductivity

Hall effect measurement, along with the negative polarity of V_s, indicated that $Bi_{1-x}Sb_x$ $(0 \leq x \leq .45)$ have n-type conductivity.

5.4.5 The figure of merit

Harman technique (see Section (4.3.2)) was used to compare the values of ZT for a pure Bi and $Bi_{.87}Sb_{.13}$ alloy deposited on glass substrate; both having thickness of ~55 nm. The results are given in Table (5.6). The alloy showed an enhancement of about 32% in ZT.

5.4.6 The output power

The output power from a $Bi_{.87}Sb_{.13}$ alloy, that has an area of about 1 cm^2 and thickness of about 55 nm, delivered to a matching resistive load (0.86 KΩ) was calculated. The results are given in Table (5.7) along with the corresponding Seebeck voltage and the temperature difference across the sample. From the data of Table (5.7), one can conclude that a unit composed of 10 modules each consisting of 10 segments (giving a total weight of ~50μg, substrate not included) can deliver about 5.2 μW to a resistive load for a temperature difference of 190°. This is a low power, but still useful as explained in Section (3.4).

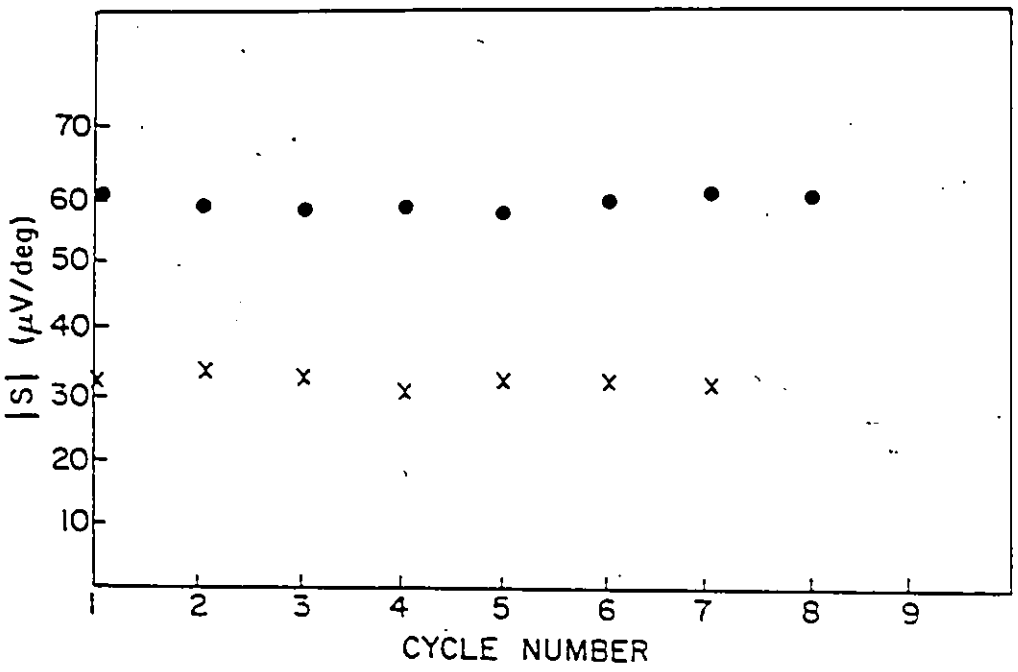

Fig. (5.18) Repeated measurements of the thermoelectric power for the two Bi-Sb alloys with different Sb concentrations.

5.4.7 Dependence of the thermoelectric power on the mixing dose

The thermoelectric power, S, was measured as a function of the dose of bombardment ions, ϕ. The samples were composed of a Bi film with a thin layer of Sb buried in the middle. The results of bombardment with 60 KeV Ar^+ are shown in Fig. (5.19). The results indicate that S increases with ion dose rapidly at low doses, then it approaches saturation at high doses. It can also be seen that for doses higher than a threshold, ϕ_{th}, of $\sim 1.0 \times 10^{14}$ Ar^+/cm^2, S is proportional to $\sqrt{\phi}$. In other words, for $\phi > \phi_{th}$, the thermoelectric power and the alloy thickness have the same functional dependence on ϕ.

The results shown in Fig. (5.19) can be explained qualitatively as follows: in region I, the thickness of the alloy region in the sample is small and the Sb concentration is high so that S is not dominated by the contribution from the alloy region. In region II, the contribution from the alloy dominates. In region III, the thickness of the alloy approaches the total film thickness and hence S approaches saturation.

In order to relate the above picture to the thermoelectric theory, consider the diagram shown in Fig. (5.20). It shows schematically the effect of bombardment with an ion dose, ϕ, for $\phi < \phi_{max}$, where ϕ_{max} is the dose that results in a uniform alloy.

A mixed layer is formed starting from the initial Bi/Sb interface. The measured thermoelectric power, S, is the resultant of contributions from the thermoelectric powers of antimony, S_{Sb}, bismuth, S_{Bi} and the alloy, S_{Al}. Here we have the case of the single conductor that has independent groups of charge carriers such that each group acting alone can contribute a thermoelectric power S_{Sb}, S_{Al}, and S_{Bi}. According to Eq. (3.32), one can then represent the partially mixed alloy by the circuit shown in Fig. (5.21). As the mixing-ion dose increases, the following effects that may influence S will occur:

i) The thickness of the mixed Bi-Sb layer increases.

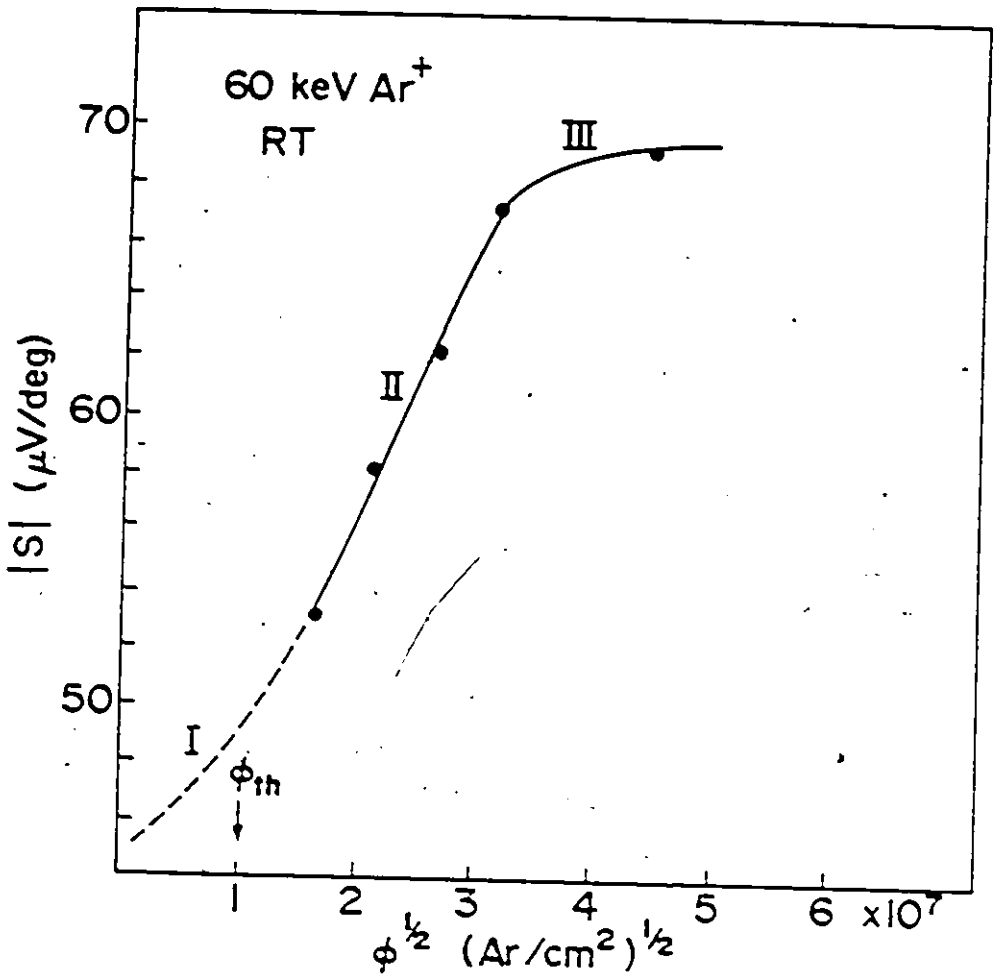

Fig. (5.19) The thermoelectric power versus the square root of the ion dose for 60 KeV Ar^+ bombardment at room temperature.

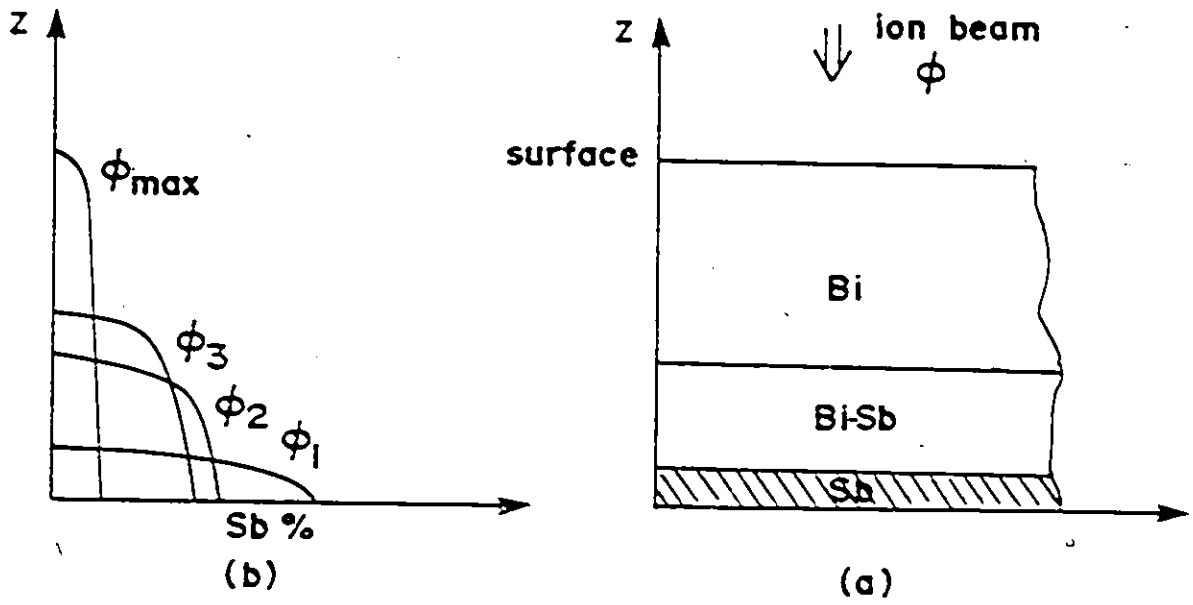

Fig. (5.20) The evolution of a Bi-Sb alloy due to ion bombardment.

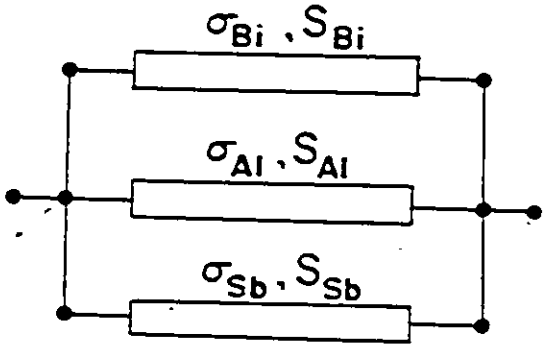

Fig. (5.21) The equivalent circuit of a partially mixed Bi/Sb system.

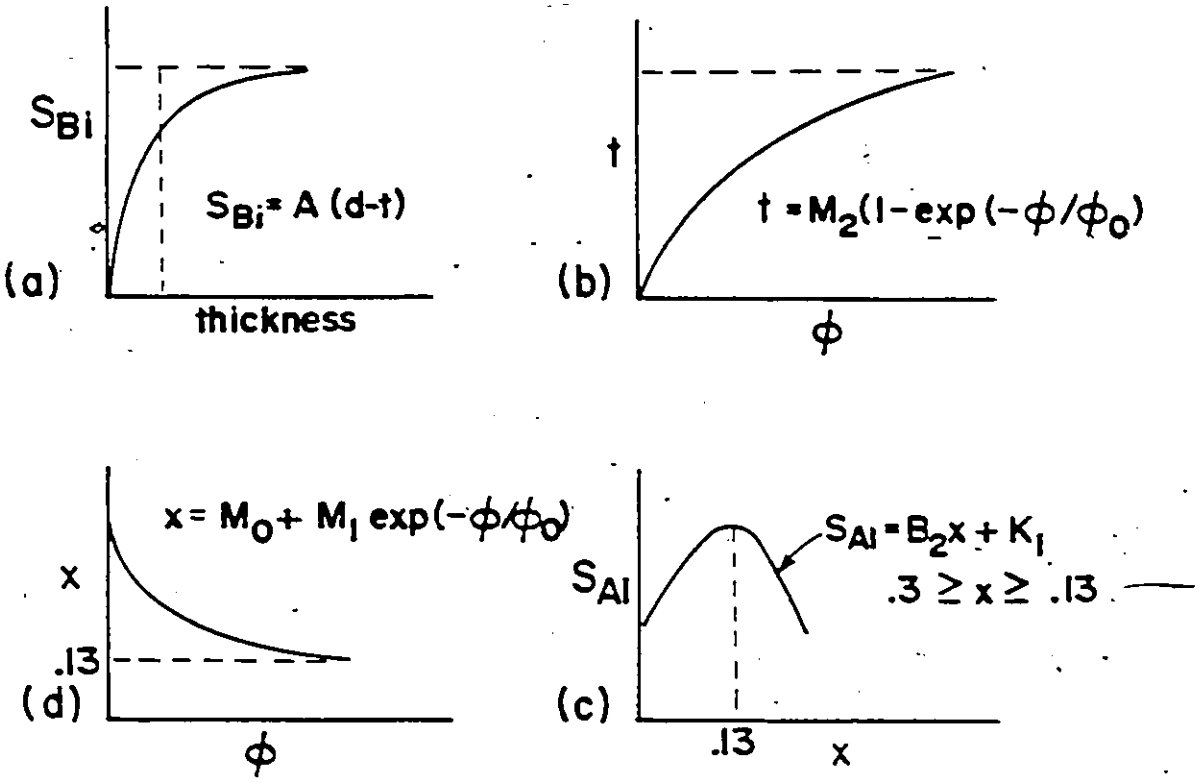

Fig. (5.22) Schematic of some relations used in the analysis of S dependence on ϕ.
a) Dependence of S_{Bi} on thickness, approximated from Ref. [140].
b) Dependence of alloy thickness on the ion dose.
c) Thermoelectric power of the alloy vs. composition.
d) Composition vs. ion dose.

ii) The average concentration of Sb in the alloy decreases.

iii) The thickness of Bi and Sb layers decrease.

iv) The concentration of the bombarding ions that become implanted in the sample increases.

Sputtering is a fifth factor that can influence the overall thermoelectric power by decreasing the total film thickness. For the present purpose, the effect of sputtering will not be considered.

The consequences of the previous effects are:

i) An increase in S_{Al} because of the increase in the effective alloy thickness and because of the decrease of the Sb concentration in the alloy.

ii) A decrease in S_{Bi} and S_{Sb} due to the decrease in the thickness of pure Bi and Sb layers as shown in Fig. (5.15).

iii) Since the mixing ions are Ar^+ and Kr^+, they are expected to have no effect on the value of S. This was confirmed by measuring S as a function of dose for a pure Bi film bombarded with Ar ions. Also, V_s and S for $Bi_{.87}$ $Sb_{.13}$ prepared by Ar^+ and Kr^+ bombardment were measured. No dependence on the mixing ion was observed.

To obtain an analytical expression for the dependence of S on ϕ, based on the above physical description, we start with Eq. (3.32), then we employ approximate analytical relations between the ion dose, composition and thickness and between the composition, thickness and thermoelectric power. These relations are sketched in Fig. (5.22).

The objective of the analysis is to show that indeed the above picture can lead to the findings shown in Fig. (5.19). In the analysis the alloy thickness is assumed to have an exponential dependence on ϕ, to encompass the low and high dose regions in one simple function. This assumpton is made to simplify the mathematics and is valid as a first order

approximation. A complicated function, f(ϕ), could have been used, but since the purpose is to show that the analysis leads to the conclusion that if the alloy thickness dependence on ϕ is represented by f(ϕ) then S should be proportional to f(ϕ), a simple function is more adequate.

From Eq. (3.32), the overall thermoelectric power, S, can be expressed as:

$$S = \frac{\sigma_{Bi}}{\sigma_{Bi}+\sigma_{Al}+\sigma_{Sb}} \cdot S_{Bi} + \frac{\sigma_{Al}}{\sigma_{Bi}+\sigma_{Al}+\sigma_{Sb}} \cdot S_{Al} + \frac{\sigma_{Sb}}{\sigma_{Bi}+\sigma_{Al}+\sigma_{Sb}} \cdot S_{Sb} \qquad (5.12)$$

where, σ_{Bi}, σ_{Al}, and σ_{Sb} are the electrical conductivities of the Bi, alloy and Sb layers, respectively. These conductivities are thickness dependent when the thickness is comparable to the mean free path, mfp, of the charge carriers. The mfp is ~ 60nm for Bi and does not change appreciably for the alloy. Since the overall thickness of the film in the present study is ~ 55nm, σ_{Bi}, σ_{Al}, and σ_{Al}, are always thickness dependent. We can further assume that the thickness dependence of σ_{Bi}, and σ_{Al} is the same because the mfp does not change significantly. The contribution from the antimony layer can be neglected because the layer is initially very thin and because $|S_{Sb}| < |S_{Bi}|$ for similar film thicknesses. This was verified experimentally by comparing the values of S for a pure Bi film and an unbombarded Bi-Sb sample. The two values were almost identical.

Equation (5.12) can be simplified further by considering:

$$\frac{\sigma_{Bi}}{\sigma_{Bi}+\sigma_{Al}} = \frac{A(d-t)}{A(d-t)+At} = \left(1-\frac{t}{d}\right) \qquad (5.13)$$

and

$$\frac{\sigma_{Al}}{\sigma_{Bi}+\sigma_{Al}} = \frac{At}{A(d-t)+At} = A_1 t \qquad (5.14)$$

where, A and $A_1 = 1/d$ are constants, d is the overall thickness of the film and t is the thickness of the alloy. Here we assumed the thickness dependence of σ_{Bi} and σ_{Al} to be the same.

Accordingly, Eq. (5.12) reduces to the approximate equation given by:

$$S = \left(1 - \frac{t}{d}\right) \cdot S_{Bi}(t) + A_1 t \cdot S_{Al}(t, x) \tag{5.15}$$

where, x is the average composition (Sb%).

Eq. (5.15) can be expressed as:

$$S = \left(1 - \frac{t}{d}\right) \cdot S_{Bi}(t) + A_1 t \cdot S_{Al}(t) S_{Al}(x) \tag{5.16}$$

From the approximate relations of Fig. (5.22), we have:

$$S_{Bi}(t) = S_1\left(1 - \exp.\left(-\frac{d-t}{d_o}\right)\right) \tag{5.17}$$

where S_1 and d_o are constants.

Hence, the first term in Eq. (5.16) can be expressed as:

$$\begin{aligned}\left(1 - \frac{t}{d}\right) \cdot S_{Bi}(t) &= \left(1 - \frac{t}{d}\right)\left\{S_1 - S_2\left[1 + \left(\frac{t}{d_o}\right) + \frac{1}{2}\left(\frac{t}{d_o}\right)^2 + \ldots\right]\right\} \\ &= S_2 - S_1\left(\frac{1}{d_o} + \frac{1}{d}\right) \cdot t - \frac{1}{2} S_1\left(\frac{1}{d_o^2 - \frac{1}{d\, d_o}}\right) t^2 - \ldots \\ &= S_3 - S_4 t - S_5 t^2 - \ldots\end{aligned} \tag{5.18}$$

where S_1, S_2, S_3, and S_4 are constants. Also, the thickness of the Bi layer, $d - t$, decreases with ion dose, ϕ, as the alloy region grows due to ion bombardment. The increase in the alloy thickness, t, with ϕ can be expressed as (see Fig. 5.22):

$$t = M_2(1 - \exp.(-\phi/\phi_o)) \tag{5.19}$$

where M_2 is a constant. ($M_2 \simeq d$)

Hence, Eq. (5.18) becomes:

$$\begin{aligned}\left(1 - \frac{t}{d}\right) \cdot S_{Bi}(t) &= S_2 - S_3 M_2(1 - \exp.(-\phi/\phi_o)) \\ &\quad - S_4(1 - \exp.(-\phi/\phi_o))^2 - \ldots \\ &= S_5 + S_6 \exp.(-\phi/\phi_o) + \ldots\end{aligned} \tag{5.20}$$

where S_3, S_4, S_5, and S_6 are constants.

Similarly, we can write:

$$S_{Al}(t) = S_5' - S_6' \exp.(-\phi/\phi_o) + \ldots \tag{5.21}$$

where S_5' and S_6' are constants.

For the condition that $x > 0.13$, we can approximate the compositional dependence of S_{Al} (see Fig. (5.22) as:

$$S_{Al}(x) = B_2 x + K_1 \tag{5.22}$$

where B_2 and K_1 are constants.

Using the compositional dependence on dose, given in Fig. (5.22), Eq. (5.22) becomes:

$$S_{Al}(x) = B_2 M_1 \exp.(-\phi/\phi_o) + K_1 + B_2 M_o \tag{5.23}$$

Using equations (5.20), (5.21), and (5.23), Eq. (5.16) becomes:

$$\begin{aligned} S &= \left(1 - \frac{t}{d}\right) \cdot S_{Bi}(t) + A_1 t \cdot S_{Al}(t, \bar{x}) \\ &= S_5 + S_6 \exp.(-\phi/\phi_o) + A_1 M_2 (1 - \exp.(-\phi/\phi_o)) \times \\ &\quad (S_5' + S_6' \exp.(-\phi/\phi_o)) \cdot (B_2 M_1 \exp.(-\phi/\phi_o) + K_1 + B_2 M_o) \\ &= S_m - K_o \exp.(-\phi/\phi_o) + \ldots \end{aligned} \tag{5.24}$$

Where, S_m, K_o and ϕ_o are constants. S_m is the maximum attainable thermoelectric power for a given sample geometry, K_o and ϕ_o are the parameters used to approximate the segmented function to a simple exponential. The consant ϕ_o depends mainly on the nuclear deposited energy while K_o is an agglomeration of various effects.

5.4.8 Discussion of the analysis of the dependence of S on ϕ

The analysis presented in the previous section is useful in explaining the experimental results of Fig. (5.19). It answers the question: why the thermoelectric power and the alloy thickness have a similar dependence on ion dose.

The analysis, as explained, is not meant to be used as an exact analytical relation predicting the value of the thermoelectric powers, for a given dose, ϕ; it is meant to give an insight into the physical processes leading to the dependence of S on ϕ. Nevertheless, the analysis leads to the prediction that the slope in region II (Fig. 5.19a), ϕ_{th} and ϕ_{max} should scale with the nuclear deposited energy of the bombardment ions for a given sample geometry. Although the analysis was concerned with Bi-Sb alloys, similar reasoning could be applied to similar systems, e.g., Sb-As alloys.

In the analysis, we considered bombardment with inert ions only, e.g. Ar^+ rather than Te^+. The analysis does not apply if the mixing ions lead to the formation of a ternary alloy. The role of quantum size effect was not considered. Thus, the analysis does not apply at low temperature where the quantum size effect is most pronounced.

CHAPTER VI

SUMMARY AND CONCLUSIONS

This chapter summarizes the conclusions of this work. These conclusions represent an achievement of the objectives of the work as stated in the introduction. In other words, they provide answers to the questions about the ability to form $Bi_{1-x}Sb_x$ alloy by ion beam mixing, the possible mixing mechanisms, and the thermoelectric characteristics of these alloys. Additional conclusions have also been reached; they will be summarized here as well.

6.1 Ion beam mixing

i) Uniform $Bi_{1-x}Sb_x (0 \leq x \leq .45)$ can be obtained by ion beam mixing.

ii) Ion bombardment of Bi/Sb system leads to grain growth. The grain size increases from ~100 nm to ~ 140 nm and ~150 nm after doses of $\sim 1 \times 10^{15}$ cm^{-2} and $\sim 3 \times 10^{15}$ cm^{-2} respectively of 80 KeV Ar^+.

6.2 Mixing mechanisms

i) Mixing has a square root dependence on the dose of the bombardment ions (Ar, Kr, and Ne), both at high (~350 K) and low (~40 K) temperatures. This reveals a similarity of the mixing processes with thermal diffusion.

ii) At temperatures lower than ~266 K, cascade mixing dominates; the mixing is independent of temperature. The effective diffusion coefficient, D^*, is 4.9×10^{-28} cm^4/ion.

iii) At temperatures higher than 266 K, radiation enhanced diffusion dominates; the rate of mixing increases with temperature in the range where the temperature alone (without irradiation) causes very little

diffusion. The effective diffusion coefficient, D*, at 300 K is 1.7×10^{-27} cm^4/ion.

iv) In the radiation-enhanced-diffusion regime, the activation energy is about 0.15 eV.

v) The rate of mixing is observed to increase with the elastic energy density deposited in the interface region.

6.3 The thermoelectric characteristics

i) The thermal voltage, V_s, of the $Bi_{1-x}Sb_x$ ($0\leq x\leq 0.45$) has a linear dependence on the temperature in the range 300 to 500 K.

ii) The absolute thermoelectric power of $Bi_{1-x}Sb_x$, $|S|$, increases as x increases up to $x=0.13$, then it decreases (S is negative).

iii) Implanted Kr and Ar do not contribute to the thermoelectric power of Bi or $Bi_{1-x}Sb_x$.

iv) A Bi/Sb system bombarded with inert ions can be modelled, for thermoelectric characterization, by three resistors connected in parallel with the thermal voltages (or the thermoelectric powers) appearing across the corresponding elements.

v) A $Bi_{.87}Sb_{.13}$ segment (5.0×10^{-7} gm) delivers 5.2×10^{-8} W to a matching load for an applied temperature difference of 190°.

6.4 General

i) Thin film thermoelectrics have unique applications, such as in cardiac pacemakers. However, they cannot compete with thin film solar cells as energy converters for general purposes.

ii) Thermoelectric measurements can be used, in some cases, as an analytical tool to give information about the uniformity of an alloy.

iii) The findings of this work may lead to the revival of the interest in alloys that have received less attention in the past because of the difficulty of preparation. These alloys may have a potential for efficient thermoelectric energy conversion, e.g. Sb-As alloys [149].

REFERENCES

[1] K.L. Chopra, and I. Kaur, Thin Film Device Applications, Plenum Press, New York (1983).

[2] D.M. Rowe, Proc. IEE, 125, 1113 (1978).

[3] R.D. Cocfield, R.F. Hartman, and C.E. Kelly, in Proc. of 15th Intersociety Energy Conversion Engineering Conference, Seattle, Washington (1980), p.1043.

[4] R.E. Benenson, V.K. Tikku, D. Kollwe, and H.-S. Jin, Nucl. Instr. and Meth. **209/210**, 185 (1983).

[5] A.M. Ibrahim, and D.A. Thompson, Mat. Chemistry and Phys., 12, 29 (1985).

[6] E.M. Kunoff, B.S. Elmna, and M.S. Dresselhaus, Mat. Res. Soc. Symp., 27, 553 (1984).

[7] Z.L. Liau, and J.W. Mayer, J. Vac. Sci. Technol., 15, 1629 (1978).

[8] H.H. Andersen, and H.L. Bay in Sputtering by Particle Bombardment, ed., R. Behrisch, Springer-Verlag, Berlin (1981), p. 189.

[9] H.J. Goldsmid, Phys. Stat. Sol. (a), 1, 7 (1970).

[10] S. Matteson, and M-A. Nicolet, Ann. Rev. Mat. Sci., 33, 339 (1983).

[11] A.J. Barcz, and M-A. Nicolet, Appl. Phys. A, 33, 167 (1984).

[12] A.J. Barcz, and B.M. Paine, and M.-A. Nicolet, Appl. Phys. Lett., 44, 45 (1984).

[13] Wang Ke-Ming, C. Burman, W.A. Lanford, and R. Groleau, Rad. Eff. Lett., 85, 177 (1985).

[14] A.M. Ibrahim, and D.A. Thompson, Nucl. Instr. and Meth., B7/8, 566 (1985).

[15] J. Lindhard, and M. Scharff, Phys. Rev., 124, 128 (1961).

[16] H. Goldstein, Classical Mechanics, Addison-Wesley, Cambridge, Mass. (1958).

[17] N. Bohr, Mat. Fys. Medd. Dan. Vid. Selesk., 18, No. 8 (1948).

[18] E. Rutherford, Phil. Mag., 21, 669 (1911).

[19] J. Lindhard, M. Scharff, and H.E. Schiøt, Mat. Fys. Medd. Dan. Vid. Selesk., **33**, No. 14 (1962).

[20] A.A. Abrahamson, Phys. Rev., **133A**, 990 (1964).

[21] J. Lindhard, Mat. Fys. Medd. Dan. Vid. Selesk., **34**, No. 14 (1965).

[22] O.B. Firsov, Sov. Phys. JEPT, **6** (33), 534 (1958).

[23] P. Gombas, Handbuch der Physik, Ed. XXXVI (1956).

[24] J. Lindhard, V. Nielsen, and M. Scharff, Mat. Fys. Medd. Dan. Vid. Selesk., **36**, No. 10 (1968).

[25] M. Born, and J.E. Mayer, Z. Physik, **75** (1), 96 (1932).

[26] J. Lindhdard, V. Nielsen, N. Scharff, and P.V. Thomson, Mat. Fys. Medd. Dan. Vid. Selesk., **33** No. 10 (1963).

[27] H.A. Bethe, Ann. Phys., **5**, 325 (1930).

[28] J. Lindhard, and A. Winther, Mat. Fys. Medd. Dan. Vid. Selesk., **34**, 4 (1964).

[29] F.H. Eisen, Can. J. Phys., **46**, 561 (1968).

[30] P. Hvelplund, and B. Fastrup, Phys. Rev., **165**, 408 (1968).

[31] I.M. Cheshire, G. Dearnaley, and J.M. Poate, Phys. Lett., **27A**, 304 (1968).

[32] J.S. Briggs, and A.P. Pathak, J. Phys. C., Solid State Physics, **6**, L153 (1973).

[33] H.W. Bragg, and R. Kleeman, Phil. Mag., **10**, 5318 (1905).

[34] G.H. Kinchin, and R.S. Pease, Rep. Prog. Phys., **18** (1), 143 (1955).

[35] M.T. Robinson, Phil. Mag., 17, 639 (1968).

[36] P. Sigmund, Appl. Phys. Lett., 14 No. 3, 114 (1969).

[37] K.B. Winterbon, P. Sigmund, and J.B. Sanders, Mat. Fys. Medd. Kgl. Dan. Vid. Selesk., **37** No. 14 (1970).

[38] H. Cramer, Mathematical Methods of Statistics, Princeton University Press, Princeton, N.J. (1964).

[39] E.M. Baroody, J. Appl. Phys., **36**, 3562 (1965).

[40] J.A. Brinkman, J. Appl. Phys., **25**, 961 (1954).

[41] J.A. Brinkman, Am. J. Phys., **24** 246 (1956).

[42] D.A. Thompson, Rad. Effects, 56, 105 (1981).

[43] F. Seitz, and J.S. Koehler, Progress in Solid State Physics, 2, 305 (1956).

[44] M.W. Thompson, and R.S. Nelson, Phil. Mag., 7, 205 (1962).

[45] R. Kelly, Surf. Science, 90, 280 (1979).

[46] R. Collins, Rad. Effects, to be published.

[47] H.H. Andersen, Appl. Phys., 18, 131 (1979).

[48] P.K. Haff, and Z.E. Switkowski, J. Appl. Phys., 48, 3383 (1977).

[49] S.M. Myers, Nucl. Instr. and Meth., 168, 265 (1980).

[50] G.J. Dienes, and A.C. Damask, J. Appl. Phys., 29, 1713 (1958).

[51] S.M. Myers, D.E. Amos, and D.K. Brice, J. Appl. Phys., 47, 1812 (1976).

[52] D. Gupta, D.R. Campbell, and P.S. Ho in Thin Films-Interdiffusion and Reactions, J.M. Poate, K.N. Tu and J.M. Mayer, eds., John Wiley, New York (1978).

[53] L.G. Harrison, Trans. Faraday Soc., 44, 4455 (1973).

[54] D. Peak, and R.S. Averback, Nucl. Instr. and Meth., B7/8, 561 (1985).

[55] U. Shreter, F.C.T. So, B.M. Paine, and M.-A. Nicolet, Mat. Res. Soc. Symp. Proc., 27, 31 (1984).

[56] T. Banwell, B.X. Liu, I. Golecki and M.-A. Nicolet., Nucl. Instr. and Meth., 209/210, 125 (1983).

[57] W.L. Johnson, Y.T. Cheng, M. van Rossum, and M.-A. Nicolet, Nucl. Instr. and Meth., B7/8, 657 (1985).

[58] S. Matteson, J. Roth, and M.-A. Nicolet, Rad. Effects, 42, 217 (1979).

[59] B.M. Paine, and R.S. Averback, Nucl. Instr. and Meth., B7/8, 666 (1985).

[60] J. Bøttiger, S.K. Nielsen, H.J. Whitlow, and P. Wriedt, Nucl. Instr. and Meth., 218, 684 (1983).

[61] G.J. Clark, A.D. Marwick, and D.B. Poker, Nucl. Instr. and Meth., 209/210, 107 (1985).

[62] B.M. Pain, M.-A. Nicolet, R.G. Newcombe, and D.A. Thompson, Nucl. Instr. and Meth., 182/183, 115 (1981).

[63] S.J. Kim, M.-A. Nicolet, R.S. Averback, and P. Baldo, Appl. Phys. Lett., to be published.

[64] L.S. Wielunski, B.M. Paine, B.X. Liu, C.-D. Lien, and M.-A. Nicolet, Phys. Stat. Sol. (a), 72, 399 (1982).

[65] C.T. Chang, S.V. Campisano, S. Cannavpo, and E. Rimini, J. Appl. Phys., 55, 3322 (1984).

[66] R.S. Averback, L.J. Thompson, and L.E. Rehn, Mat. Res. Symp. Proc., 27, 25 (1984).

[67] M.-A. Nicolet, T.C. Banwell, and B.M. Paine, Mat. Res. Symp. Proc., 27 3 (1984).

[68] P. Sigmund, Appl. Phys., A30, 1 (1983).

[69] J. Bøttiger, S.K. Nielsen, and P.T. Thorsen, Nucl. Instr. and Meth., B7/8, 707 (1985).

[70] M.G. Scott and R.A. Collins, and G. Dearnaley, Rad. Effects, 81, 211 (1984).

[71] B.M. Paine, and R.S. Averback, Nucl. Instr. and Meth., B7/8, 666 (1985).

[72] D.B. Poker, O.W. Holland, and B.R. Appleton, Mat. Res. Soc. Symp. Proc., 27, 73 (1984).

[73] B.Y. Tsaur, and J.W. Mayer, Phil. Mag., A43, 345 (1981).

[74] K.L. Wang, F. Bacon, and R.F. Reihl, J. Vac. Sci. Technol., 16, 130 (1979).

[75] K. Saito, and M. Iwaki, Nucl. Instr. and Meth., B7/8, 626 (1985).

[76] R.S. Averback, L.G. Thompson, Jr., J. Moyle, and M. Schalit, J. Appl. Phys., 53, 1342 (1982).

[77] J. Bøttiger, S.K. Nielsen, H.J. Whitlow, and P. Wriedt, Nucl. Instr. and Meth., 218, 684 (1983).

[78] J. Bøttiger, S.K. Nielsen, and P.T. Thorsen, J. de Phys., to be published.

[79] S. Matteson, G. Mezey, and M.-A. Nicolet, in Proc. Symp. on Thin Film Interfaces and Interactions, eds., J.E.E. Baglin and J.M. Paate, Los Angeles (1979), p. 242.

[80] S. Matteson, B.M. Paine, M.G. Grimaldi, G. Mezey, and M.-A. Nicolet, Nucl. Instr. and Meth., 182/183, 43 (1981).

[81] B.Y. Tsaur, S.S. Lau, and J.W. Mayer, Appl. Phys. Lett., 36, 823 (1980).

[82] B.X. Liu, W.L. Johnson, and M.-A. Nicolet, Appl. Phys. Lett., 42, 45 (1983).

[83] B.Y. Tsaur, and J.W. Mayer, Appl. Phys. Lett., 37, 389 (1980).

[84] J.L. Brimhall, H.E. Kissinger, and L.A. Charlot in Metastable Materials Formation by Ion Implantation, eds., S.T. Picraux and W. Choke, Vol. 7, North Holland, New York (1982).

[85] C. Jaouen, J.P. Riviére, A. Bellara, and J. Delafond, Nucl. Instr. and Meths., B7/8, 97 (1985).

[86] B.Y. Tsaur, and M. Mäenpää, J. Appl. Phys., 52, 728 (1981).

[87] P. Wang, D.A. Thompson, and W.W. Smeltzer, Nucl. Instr. and Meth., B7/8, 97 (1985).

[88] S.W. Angrist, Direct Energy Conversion, Allyn and Bacon, Boston (1971).

[89] R.D. Barnard, Thermoelectricity in Metals and Alloys, Taylor and Francis Ltd., London (1972).

[90] A.V. Gold, D.K. MacDonald, W.B. Pearson, and I.M. Templeton, Phil. Mag., 5, 781 (1960).

[91] G.C. Jain, and W.B. Berry, Transport Properties of Solids and Solid State Energy Conversion, Tata McGraw-Hill, Bombay (1972).

[92] J.S. Blackemore, Semiconductor Statistics, Pergman Press, Oxford (1962).

[93] K.L. Chopra, Thin Film Phenomena, McGraw-Hill, New York (1969).

[94] E.H. Sondheimer, Advan. Phys., 1, 1 (1962).

[95] C.R. Telllier, and A.J. Tosser, Size Effects in Thin Films, Elsevier, New York (1982).

[96] K.L. Chopra, R. Suri, and A.P. Thakoor, J. Appl. Phys., 48, 538 (1977).

[97] K.L. Chopra, and A.P. Thakoor, J. Appl. Phys., 49, 2855 (1978).

[98] K.L. Chopra, R. Suri and A.P. Thakoor, Phys. Rev. B, 15, 4682 (1977).

[99] K.L. Chopra, A.P. Thakoor, S.K. Barthwal, and P. Nath, Phys. Stat. Sol. (a), 40, 247 (1977).

[100] Ho-Yuan Yu, and W.F. Leonard, J. Appl. Phys., 44, 5324 (1973).

[101] M.A. Angadi, and L.A. Udachan, J. Phys. D. Appl. Phys., 14, L03 (1981).

[102] D. De, S. Chaudhuri, and A.K. Pal, Thin Solid Films, 99, 371 (1983).

[103] M.A. Angadi, and L.A. Udachan, J. Mat. Sci. Lett., 1, 539 (1982).

[104] R.V. Wilhelm, Jr., and J.P. Roland, J. Appl. Phys., 48, 2086 (1976).

[105] G. Wedler, and R. Chander, Thin Solid Films, 65, 53 (1980).

[106] M.J. Burns, and P.M. Chaikin, Phys. Rev. B, 27, 5924 (1983).

[107] M.A. Angadi, and P.V. Ashrit, J. Phys. D. Appl. Phys., 14, L125 (1981).

[108] A. Perianti, and G.F. Paicentini, J. Vac. Sci. Technol., 14, 169 (1977).

[109] K.L. Chopra, and S.K. Bahl, Thin Solid Films, 12, 211 (1972).

[110] K.L. Chopra, and P. Nath, Phys. Stat. Sol. (a), 33, 333 (1976).

[111] S. Hishida, M. Konagai, and K. Takahashi, Thin Solid Films, 112, 7 (1984).

[112] S. Chaudhuri, B. Chakrabarti, and A.K. Pal, Thin Solid Films, 82, 217 (1981).

[113] L.I. Bytenskii, T.S. Gudbin, E.K. Iordanishvili, and S.A. Kaz'min, V.I. Kaidanov, Sov. Phys. Semicond., 11, 849 (1977).

[114] J.U. Trefny, and T.S. Jayadev, Proc. of the 15th Intersociety Energy Conv. Conf., Seattle, Washington (1980), p. 1610.

[115] A. Arrial, J.C. Bernede, and A. Conan, Thin Solid Films, 69, 23 (1980).

[116] S. Yugo, and T. Kimura, Phys. Stat. Sol. (a), 59, 263 (1980).

[117] S. Yugo, T. Sato, and T. Kimura, Appl. Phys. Lett., 46, 842 (1985).

[118] V.G. Sidrov, L.S. Sveshkova, M.D. Shagalov, and Yu K. Shalabutov, Sov. Phys. Semicond., 10, 1309 (1977).

[119] C. Weclwicz, L. Zdanawicz, and J. Jurusik, Proc. 1st Int. Symp. on Phys. and Chemistry of II-V Compounds, Poland (1980), p. 125.

[120] G.E. Smith, and R. Wolfe, J. Appl. Phys., 33, 841 (1962).

[121] F.D. Rosi, E.F. Hockings, and N.E. Lindenablad, RCA Rev., 22, 82 (1961).

[122] D.A. Wright, Metal. Rev., 15, 147 (1970).

[123] J.M. Doyle, Thin-Film and Semiconductor Integrated Circuitry, McGraw-Hill, New York (1966).

[124] R.K. Collier, and C.E. Bakus, Proc. of the 7th Intersociety Energy Conversion Engineering Conf., San Diego, California (1972), p. 216.

[125] D.M. Rowe, and C.M. Bhandari, Modern Thermoelectrics, Holt, Rinehart and Winston Ltd., London (1983).

[126] T.L. Chu, S.S. Chu, C.L. Lin, and R.M. Davis, Abstracts of the Fourth Annual Photovoltaic Advanced Research and Development Conference, Solar Energy Research Institute, Colorado (1980), p. 173.

[127] F. Schmid, C.P. Khattak, and M. Basaran, Abstracts of the Fourth Annual Photovoltaic Advanced Research and Development Conference, Solar Energy Research Institute, Colorado (1980), p. 166.

[128] R.D. Dupuis, P.D. Dapkus, R.D. Yingling, and L.A. Mondy, Appl. Phys. Lett., 31, 201 (1977).

[129] J.A. Borders, and S.T. Picraux, Proc. IEEE, 62, 1224 (1974).

[130] Wei-Kan Chu, J.W. Mayer, and M.-A. Nicolet, Backscattering Spectrometry, Academic Press, New York (1978).

[131] L.C. Feldman, and J.M. Poate, Ann. Rev. Matr. Sci., 12, 149 (1982).

[132] F.J. Blatt, P.A. Schroeder, C.L. Foiles, and D. Greig, Thermoelectric Power of Metals, Plenum Press, New York (1976).

[133] F.E. Jaumot in Direct Conversion of Heat into Electricity, eds., J. Kaye and J.A. Welsh, John Wiley, New York (1960).

[134] T.C. Harman, J.H. Cahn, and M.J. Logan, J. Appl. Phys., 30, 1351 (1959).

[135] J.U. Trefny, Proc. 4th Intern. Conf. on Thermoelectric Energy Conversion (sponsored by IEEE), Arlington, Texas (1982), p. 79.

[136] R.M. Tahboub, M. El Gindy, and H.D. Merchent, Oxidations of Metals, 13, 454 (1979).

[137] S. Otabe, Y. Ishii, and N. Matsuno, Jpn. J. Appl. Phys., 20, 1037 (1981).

[138] W. Seith, Z. Electrochem., 39, 538 (1933).

[139] W.P. Ellis, and N.H. Nachtrieb, J. Appl. Phys., 40, 472 (1969).

[140] M. Favennec, M. LeContellec, and J. LeTraon, Thin Solid Films, 13, 73 (1972).

[141] R.B. Horst, and L.R. Williams, Proc. of the 3rd International Conf. on Thermoelectric Energy Conversion, Arlington, Texas (1980), p. 139.

[142] G.A. Mironova, M. Sudakova, and Y.G. Ponomorev, Sov. Phys. JEPT, 51, 918 (1980).

[143] S. Golin, Phys. Rev., 176, 830 (1968).

[144] W.F. Ehret, and M.B. Abramson, J. Am. Chem. Soc., 56, 385 (1934).

[145] N.B. Brandt, R. Hermann, G.I. Golysheva, L.I. Devyatkova, D. Kurski, W Kraak, and Y.G. Ponomarev, Sov. Phys. JEPT, **56**, 1247 (1982).

[146] E.G. Brown, and M.W. Jones, Phil. Mag., **7**, 1029 (1932).

[147] A.L. Jain, Phys. Rev., **6**, 1518 (1959).

[148] V. Damodara Das, and M.S. Jagadesh, Mat. Res. Bull., **16**, 1547 (1981).

[149] A.M. Ibrahim, The Second McMaster University Symposium on Nuclear Science and Engineering, McMaster University, Hamilton, Ontario (1985).